



**CONSTITUTIVE MODELING
FOR ISOTROPIC MATERIALS (HOST)
(FINAL REPORT)**

By
K. S. Chan
U. S. Lindholm
S. R. Bodner

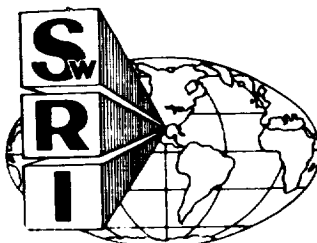
**SOUTHWEST RESEARCH INSTITUTE
P. O. Drawer 28510
San Antonio, TX 78284**

Prepared For
**NATIONAL AERONAUTICS AND SPACE ADMINISTRATION
NASA-Lewis Research Center
Contract NAS3-23925**

(NASA-CR-182132) CONSTITUTIVE MODELING FOR
ISOTROPIC MATERIALS Final Report (Southwest
Research Inst.) 155 p CSCL 21E

N88-29811

Unclas
G3/07 0167345



**SOUTHWEST RESEARCH INSTITUTE
SAN ANTONIO
HOUSTON**

1. Report No. NASA CR 182132		2. Government Accession No.		3. Recipient's Catalog No.	
4. Title and Subtitle Constitutive Modeling for Isotropic Materials				5. Report Date June 1988	
				6. Performing Organization Code	
7. Author(s) K. S. Chan, U. S. Lindholm, and S. R. Bodner				8. Performing Organization Report No. SwRI Project No. 06-7576	
				10. Work Unit No.	
9. Performing Organization Name and Address Southwest Research Institute Department of Materials Sciences P. O. Drawer 28510 San Antonio, TX 78284				11. Contract or Grant No. NAS3-23925	
12. Sponsoring Agency Name and Address National Aeronautics & Space Administration Washington, DC 20546				13. Type of Report and Period Covered Final Report	
				14. Sponsoring Agency Code RTOP 533-04-1A	
15. Supplementary Notes Project Manager, R. L. Thompson NASA Lewis Research Center (MS 49-7) 21000 Brookpark Road Cleveland, OH 44135					
16. Abstract <p>This report presents the results of the third and fourth year of work on a four-year research program which is part of the NASA HOST Program. The program goals were (1) to develop and validate unified constitutive models for isotropic materials, and (2) to demonstrate their usefulness for structural analyses of hot section components of gas turbine engines. The unified models selected for development and evaluation were those of Bodner-Partom and of Walker.</p> <p>The unified approach for elastic-viscoplastic constitutive equations has been shown to be a viable method for representing and predicting material response characteristics in the range where strain rate and temperature dependent inelastic deformations are experienced. This conclusion has been reached by extensive comparison of model calculations against the experimental results of a sophisticated test program on two high temperature Ni-base alloys, B1900+Hf and Mar-M247, over a wide temperature range for a variety of deformation and thermal histories including uniaxial, multiaxial, and thermomechanical loading paths. Particular material effects which have been examined in this program include strain-rate and temperature dependence of inelastic flow, isotropic and directional hardening, static thermal recovery, multiaxial cyclic hardening, thermal history effects, strain aging effects, and the effects of thin coatings and grain size on mechanical response. Procedures for evaluating the material constants have also been developed and verified.</p> <p>The applicability of the Bodner-Partom and the Walker models for structural applications has been demonstrated by implementing these models into the MARC finite element code and by performing a number of analyses including thermomechanical histories on components of the hot section of gas turbine engines and benchmark notch tensile specimens.</p> <p>The results of this four-year program have been documented in four annual reports. The results of the base program are summarized in this report. The tasks covered in this report include: (1) development of material test procedures, (2) thermal history effects, and (3) verification of the constitutive model for an alternate material.</p>					
17. Key Words (Suggested by Author(s)) Hot Section Technology, Nonlinear Structural Analysis, Unified Constitutive Model			18. Distribution Statement Unclassified Unlimited		
19. Security Classif. (of this report) Unclassified		20. Security Classif. (of this page) Unclassified		21. No. of pages 141	
				22. Price*	

PREFACE

This final report covers the effort of the optional program on the NASA HOST Program entitled "Constitutive Modeling for Isotropic Materials" conducted under Contract NAS3-23925. The effort of the base program is documented in the Second Annual Status Report. The NASA program manager for this project was Mr. Albert Kaufman who retired during the latter phase of this program. Dr. Robert Thompson has been the NASA Program Manager since Mr. Kaufman's retirement. The program manager at Southwest Research Institute is Dr. Ulric S. Lindholm. Contributors to this report are Drs. Kwai S. Chan, Richard A. Page and Mr. Andrew Nagy of SwRI, and Professor Sol R. Bodner of Technion, Israel, a consultant to this project.

ACKNOWLEDGEMENTS

We are thankful to Drs. G. R. Halford and V. Moreno for the use of the TEM results of the isothermally deformed B1900+Hf specimens that were generated in the Fatigue Life Prediction Contract (NAS3-23288). The technical assistance by Mr. F. Campbell and H. Saldana of SwRI in conducting the experiments is also acknowledged. Special thanks also go to Ms. Myrtle Brown and Linda Tufino for preparing this report.

TABLE OF CONTENTS

	<u>Page</u>
LIST OF FIGURES	vi
LIST OF TABLES	xiii
1.0 INTRODUCTION	1
2.0 DEVELOPMENT OF MATERIAL TEST PROCEDURES (TASK J)	4
2.1 Determination of Material Constants	4
2.2 Strain-Aging Effects	13
2.3 Nonproportional Hardening	20
2.4 Update on Finite-Element Analysis of the Benchmark Notch Specimen	23
3.0 THERMAL HISTORY EFFECTS (TASK K)	28
3.1 Thermal History Effects - Literature Study	28
3.2 Thermal History Effects - Numerical Integration	30
3.3 Thermomechanical Constitutive Testing	35
3.3.1 Experimental Set-up	35
3.3.2 Nonisothermal Loading Paths	45
3.4 Results: Experiment and Model	52
3.4.1 Nonisothermal Tensile Tests	52
3.4.2 Nonisothermal Creep Tests	61
3.4.3 Nonisothermal Cyclic Tests	63
3.4.4 Thermomechanical Fatigue Tests	78
3.5 Microstructure, Deformation Modes and Dislocation Structure	90
3.5.1 Microstructure	92
3.5.2 Dislocation Structures	93
3.5.2.1 Isothermal Specimens	93
3.5.2.2 Nonisothermal Specimens	96
3.5.3 Relation of Microstructural Examinations and Unified Constitutive Theories	112
3.6 Discussion of Thermal History Effects	115

TABLE OF CONTENTS (CONTINUED)

	<u>Page</u>
4.0 APPLICATION OF CONSTITUTIVE MODEL TO AN ALTERNATIVE MATERIAL (TASK L)	118
4.1 Experiments	118
4.1.1 Isothermal Tensile, Creep, and Cyclic Testing	118
4.1.2 Nonisothermal Tensile and TMF Testing	120
4.2 Correlation of Model and Experiment	121
4.3 Discussion	133
5.0 SUMMARY	138
6.0 REFERENCES	140

LIST OF FIGURES

<u>Figure</u>	<u>Page</u>
2.1 A Flow Chart Showing a Systematic Procedure for Evaluating the Material Constants in the Bodner-Partom Theory	7
2.2 The Isotropic and Directional Hardening Components of B1900+Hf in a γ - σ Plot	8
2.3 Determination of the Value of n Based on Several Strain Rates	9
2.4 Comparison of Monotonic Tensile and Jump Test Results of B1900+Hf	11
2.5 Determination of the Value of γ Based on the Slopes of the q vs $\sigma_c - \sigma_0$ Curves for B1900+Hf	12
2.6 Comparison of Jump Test Results for B1900+Hf Specimens at 648°C and With Two Different Grain Sizes	14
2.7 Comparison of Jump Test Results for B1900+Hf Specimens at 982°C and With Two Different Grain Sizes	14
2.8 Comparison of Cyclic Behavior of B1900+Hf Specimens With Two Different Grain Sizes	15
2.9 Model Representations of B1900+Hf at 649°C Using a Strain Aging Term: (a) Effects of a_0 in the Strain Aging Term on the Stress-Strain Curve, and (b) Strain Aging Effect Simulated With the Bodner-Partom Model Using $a_0 = .5$, $a_1 = .1$, and $\dot{\epsilon}_0 = 1 \times 10^{-4} \text{ sec}^{-1}$	17
2.10 Stress-Strain Curve Calculated with the Bodner-Partom Model with a Strain Aging Term	19
2.11 Bodner-Partom Model Calculation for Mar-M247 Under (1) Uniaxial Cycling for 5 Cycles, Followed by (2) 90° Out-of-Phase Cycling for 2-1/2 Cycles, and (3) Uniaxial Cycling for 5 Cycles: (a) $\sigma - \sqrt{3}\tau$ Plot, and (b) Time History of Z^D	21
2.12 Bodner-Partom Model Calculation For Mar-M247 Under the Same Loading Histories as in Figure 2.11: (a) $\sigma - \sqrt{3}\tau$ Plot, and (b) Time History of Z^D During Cycling	24
2.13 Finite-Element Mesh of the Benchmark Notch-Round Specimens	25

LIST OF FIGURES (CONTINUED)

<u>Figure</u>		<u>Page</u>
2.14	Comparison of Model Predictions with Experimental Results of the Benchmark Notched Specimen Under Monotonic Loading	27
3.1	A Schematic of the Thermomechanical Testing System	39
3.2	Specimen Designs Utilized in Various Constitutive Tests	40
3.3	Comparison of Prescribed Temperature with Specimen (Measured) Temperature	41
3.4	Thermal Strain of B1900+Hf Specimen Heated from 38°C to 538°C and Then Cycled at Zero Load from 538°C to 982°C for Ten Cycles	43
3.5	A Close-up View of a Thermomechanical Cyclic Specimen Under Cycling from 538°C to 982°C	44
3.6	Strain-Time and Temperature-Time Histories for Step Temperature Tensile Tests	48
3.7	Stress-Time and Temperature-Time Histories for Step Temperature Creep Tests	49
3.8	Strain-Time Histories for Step Temperature Cyclic Tests	50
3.9	TMF Loading Histories of Triangular Waveform: a) In-Phase Loading, (b) Out-of-Phase Loading	51
3.10	Nonisothermal Tensile Results Compared with Isothermal Tensile Data at 760°C	54
3.11	Comparison of Nonisothermal Tensile Results with Isothermal Tensile Data Obtained Based on Round-Bar Specimens from Both the Base and Optional Programs	55
3.12	Bodner-Partom Model Predictions of Nonisothermal Tensile Curves Compared to Isothermal Tensile Curves	56
3.13	Comparison of Predicted and Experimental Nonisothermal Tensile Curves for Straining at $\dot{\epsilon} = 1 \times 10^{-4} \text{ sec}^{-1}$ with Temperature Change from 760°C to 982°C with Isothermal Data	58

LIST OF FIGURES (CONTINUED)

<u>Figure</u>	<u>Page</u>
3.14 Comparison of Predicted and Experimental Nonisothermal Tensile Curves for Straining at $\dot{\epsilon} = 1 \times 10^{-4} \text{ sec}^{-1}$ with Temperature Change from 982°C to 760°C with Isothermal Data	59
3.15 Comparison of Nonisothermal Tensile Results with Model Predictions for Specimens Tested in the 538-760°C Temperature Range	60
3.16 Nonisothermal Constant Load Creep Data of B1900+Hf for Test Conditions of $\sigma = 215 \text{ MPa}$ and $T = 982^\circ\text{C}$ with Subsequent Stress and Temperature Changes to $\sigma = 690 \text{ MPa}$ and $T = 760^\circ\text{C}$ and Finally to $\sigma = 215 \text{ MPa}$ and $T = 982^\circ\text{C}$	62
3.17 Nonisothermal Constant Load Creep Data of B1900+Hf for Test Conditions of $\sigma = 690 \text{ MPa}$ and $T = 760^\circ\text{C}$ with Subsequent Stress and Temperature Changes to $\sigma = 215 \text{ MPa}$ and $T = 982^\circ\text{C}$	64
3.18 Nonisothermal Constant Load Creep Data of B1900+Hf for Test Conditions of $\sigma = 690 \text{ MPa}$ and $T = 649^\circ\text{C}$ with Subsequent Stress and Temperature Changes to $\sigma = 427 \text{ MPa}$ and $T = 871^\circ\text{C}$ and Finally to $\sigma = 690 \text{ MPa}$ and $T = 649^\circ\text{C}$	65
3.19 Comparison of Nonisothermal Creep Data with Isothermal Creep Data and Model Predictions	66
3.20 Stress-Strain Response of B1900+Hf Subjected to Strain Cycling at 538°C Until Cyclic Saturation, Strain Hold at 760°C for Two Hours, and Then Strain Cycling at 538°C	67
3.21 Stress-Time Response of B1900+Hf Subjected to Strain Cycling at 538°C Until Cyclic Saturation, Strain Hold at 760°C for Two Hours, and Then Strain Cycling at 538°C	68
3.22 Stress-Strain Response of B1900+Hf Subjected to Strain Cycling at 538°C Until Cyclic Saturation, Strain Hold at 982°C for Two Hours, and Then Strain Cycling at 538°C	71
3.23 Stress-Time Response of B1900+Hf Subjected to Strain Cycling at 538°C Until Cyclic Saturation, Strain Hold at 982°C for Two Hours, and Then Strain Cycling at 538°C	72

LIST OF FIGURES (CONTINUED)

<u>Figure</u>	<u>Page</u>
3.24 Stress-Strain Response of B1900+Hf Subjected to Strain Cycling (1) at 538°C Until Cyclic Saturation, (2) at 982°C Until Cyclic Saturation, and (3) at 538°C Until Cyclic Saturation	74
3.25 Stress-Strain Response of B1900+Hf Subjected to Strain Cycling (1) at 982°C Until Cyclic Saturation, (2) at 538°C Until Cyclic Saturation, and (3) at 982°C Until Cyclic Saturation	75
3.26 Hysteresis Loops of B1900+Hf Subjected to Strain Cycling at 760°C with Subsequent Temperature Changes to 538°C and 760°C: (a) $\Delta\epsilon = \pm 0.4\%$ and (b) $\Delta\epsilon = \pm 0.6\%$	76
3.27 Comparison of Isothermal and Nonisothermal Cyclic Data of B1900+Hf at 538°C	79
3.28 Comparison of Isothermal and Nonisothermal Cyclic Data of B1900+Hf at 760°C	80
3.29 Comparison of Isothermal and Nonisothermal Cyclic Data of B1900+Hf at 982°C	81
3.30 Hysteresis Loops of B1900+Hf Subjected to In-Phase TMF Loading Under a Mechanical Strain Range of $\pm 0.4\%$: (a) Experiment, and (b) Bodner-Partom Model Calculations	82
3.31 Hysteresis Loops of B1900+Hf Subjected to In-Phase TMF Loading Under a Mechanical Strain Range of $\pm 0.6\%$: (a) Experiment, and (b) Bodner-Partom Model Calculations	83
3.32 Hysteresis Loops of B1900+Hf Subjected to Out-of-Phase TMF Loading Under a Mechanical Strain Range of $\approx \pm 0.37\%$ in the 538-760°C Range: (a) Experiment, and (b) Bodner-Partom Model Calculation	84
3.33 Hysteresis Loops of B1900+Hf Subjected to Out-of-Phase TMF Loading Under a Mechanical Strain Range of $\approx \pm 0.55\%$ in the 538 to 760°C Range: (a) Experiment, and (b) Bodner-Partom Model Calculation	85
3.34 Hysteresis Loops of B1900+Hf Subjected to Out-of-Phase TMF Loading in the 538 to 982°C Range and a Mechanical Strain Range of $\pm 0.37\%$: (a) Experiment, and (b) Bodner-Partom Model Calculation	87

LIST OF FIGURES (CONTINUED)

<u>Figure</u>	<u>Page</u>
3.35 Hysteresis Loops of B1900+Hf Subjected to Out-of-Phase TMF Loading in the 538 to 982°C Range and a Mechanical Strain Range of $\pm 0.58\%$: (a) Experiment, and (b) Bodner-Partom Model Calculation	88
3.36 Experimental Hysteresis Loops of B1900+Hf with Yttrium-Stabilized Zirconia Coating Subjected to Out-of-Phase TMF Loading in the 538 to 982°C Range: (a) $\Delta\epsilon = \pm 0.4\%$, and (b) $\Delta\epsilon = \pm 0.6\%$	89
3.37 Microcracks Observed in the Coated B1900+Hf Specimen Subjected to an Out-of-Phase TMF Loading	91
3.38 Gamma Prime (γ') Shows Increase with Heat Treatment	94
3.39 The Morphologies of γ' Observed in Deformed B1900+Hf: (a) cuboidal γ' , (b) spaghetti γ' , (c) spheroidal γ'	
3.40 Composite TEM Photos of Tensile Tested B1900+Hf Specimens at Various Temperatures, from Moren et al [23]	97
3.41 Dislocation Networks Observed in Isothermal Creep Specimens of B1900+Hf: (a) creep tested at 982°C/283 MPa for 4.1 hours; (b) creep tested at 871°C/427 MPa for 20.6 hours; and (c) creep tested at 760°C/600 MPa for 134.8 hours	98
3.42 Dislocation Structures After Being LCF Tested at 538°C (1000°F), 10 cpm, $\Delta\epsilon = \pm 0.25\%$ for 12,500 Cycles, from Moreno et al [23]	100
3.43 Dislocation Structure After Being LCF Tested at 871°C (1600°F), 10 cpm, $\Delta\epsilon = \pm 0.25\%$ for 2,965 Cycles, from Moreno et al [23]	101
3.44 TEM Micrograph of Specimen J3-1 Showing Combination of Straight and Wavy Dislocation in γ' and Extremely High Dislocation Density in γ and at γ/γ' Interface	104
3.45 TEM Micrograph of Specimen K2 Showing Low Dislocation Density in γ , High Dislocation Density at γ/γ' Interface and Curved (Wavy) Dislocations in γ'	104
3.46 TEM Micrograph of Specimen K3 Showing Extremely High Dislocation Density in γ and at γ/γ' Interface, and Relatively Low Density of Straight and Wavy Dislocations in γ'	105

LIST OF FIGURES (CONTINUED)

<u>Figure</u>		<u>Page</u>
3.47	TEM Micrograph of Specimen K9 Showing Similar Dislocation Structures as in Specimen K3	105
3.48	TEM Micrograph of Specimen 1D Showing Extremely High Dislocation Density in γ and at γ/γ' Interface, and High Density of Straight Dislocations in γ'	106
3.49	TEM Micrograph of Specimen 1E Showing High Dislocation at γ/γ' Interface, Low Dislocation Density in Some γ , and Relatively Low Density of Curved Dislocations in γ'	106
3.50	Dislocations in the γ' of TMF Specimen Tested at: (a) 538-760°C (Specimen 1D), and (b) 538-982°C (Specimen 1E)	109
3.51	Intense Shear Bands Observed in Specimen 1E are Comprised Primarily of Edge Dislocations (a and b), and a Shear Band in Specimen 1D, Which is Comprised of Mixed Dislocations (c)	111
4.1	Correlation of the Bodner-Partom Model with Experimental Tensile Curves at Six Temperatures: (a) Experiment, and (b) Model Calculations	124
4.2	Comparisons of Model Calculation and Experiment for Tensile Test with Strain Rate Changes: (a) 23°C, (b) 648°C, and (c) 760°C	126
4.3	Creep Curve on Mar-M247 at 871°C Under an Applied Stress of 600 MPa	128
4.4	Comparison of Model Calculation and Experimental Cyclic Data at 648°C	129
4.5	Comparison of Model Calculation and Experiment for Mar-M247 Under 90° Out-of-Phase Strain Cycling at 648°C	130
4.6	Comparison of Model Calculation and Experiment for Mar-M247 Under 90° Out-of-Phase Strain Cycling at 982°C with Strain Hold at Each of the Strain Peaks	131
4.7	Comparison of the Bodner-Partom Model Calculated Curve with the Experimental Results of a Nonisothermal Tensile Test for Mar-M247 with Temperature Changes from 760°C to 649°C and Then Reverting to 760°C	132

LIST OF FIGURES (CONTINUED)

<u>Figure</u>		<u>Page</u>
4.8	Comparison of the Bodner-Partom Model Prediction with the Experimental Results of a Nonisothermal Tensile Test for Mar-M247 with Temperature Change from 649°C to 760°C	134
4.9	Comparison of Experimental Result with Bodner-Partom Model Calculation for Mar-M247 Subjected to an Out-of-Phase TMF Cycle of $\Delta\epsilon = \pm 0.4\%$: (a) Experiment, and (b) Bodner-Partom Model Calculation	135
4.10	Comparison of Experimental Result with Bodner-Partom Model Calculation for Mar-M247 Subjected to an Out-of-Phase TMF Cycle $\Delta\epsilon = \pm 0.6\%$: (a) Experiment, and (b) Bodner-Partom Model Calculation	136

LIST OF TABLES

<u>Table</u>		<u>Page</u>
2.1	A Summary of Bodner-Partom Model	5
2.2	Material Constants in Bodner-Partom Constitutive Model	6
3.1	Bodner-Partom Model Constants for B1900+Hf	36
3.2	Temperature Dependence of the Bodner-Partom Model Constants for B1900+Hf	37
3.3	Test Matrix for Thermomechanical Constitutive Testing of B1900+Hf	46
3.4	B1900+Hf Specimens Selected for Microstructural Characterization Using Transmission Electron Microscopy	103
3.5	A Summary of Dislocation Structures in B1900+Hf Specimens Under Nonisothermal or TMF Conditions	107
4.1	Isothermal Tensile, Cyclic and Creep Test Matrices for Mar-M247	119
4.2	Bodner-Partom Model Constants for Mar-M247	122
4.3	Temperature Dependence of the Bodner-Partom Model Constants for Mar-M247	123

1.0 INTRODUCTION

The objective of the present program is to evaluate and further develop existing unified constitutive models for use in finite-element structural analysis of turbine engine hot section components. This effort leads to a different approach for nonlinear finite-element computer codes which have heretofore been based on classical inelastic methods. The unified constitutive theory does not require many of the simplifying assumptions of classical elastic-plastic theory and is characterized by the use of kinetic equations and internal variables with appropriate evolution equations for treating all aspects of inelastic deformation including plasticity, creep, and stress relaxation. Specific model development has been directed toward isotropic, cast nickel-base alloys used for air-cooled turbine blades and vanes. The results of the present program have shown that this approach is particularly suited for determining the cyclic behavior of superalloy type blade and vane materials under cyclic loading conditions and high temperature environments, and is entirely compatible with three dimensional inelastic finite-element formulations. More efficient and accurate inelastic analysis of hot section components--turbine blades, turbine vanes, combustor liners and seals--fabricated from "age-hardenable" isotropic superalloy materials has been realized as the result of these developments.

The program was conducted in two phases: a basic program (Tasks A through I) and an optional follow-on program (Tasks J through M). In the basic program which was completed in 1985 [1,2], two unified constitutive models, i.e., those of Bodner-Partom [3,4] and Walker [5], underwent further development for the prediction of the structural response of isotropic

materials for temperatures and strain ranges characteristic of cooled turbine vanes in advanced gas turbine engines (Task A). A data base of uniaxial and multiaxial material response characteristics required for the constitutive model development and evaluation was obtained for the base material, B1900+Hf (Tasks C and E). The constitutive models were then incorporated into the MARC finite-element computer code (Task D). The capability of the analytical method to predict the structural response was evaluated for multiaxial stress states (Task E) and nonisothermal conditions by conducting thermomechanical loading and benchmark notch verification experiments and analysis (Task F). As a final evaluation of the analytical model, a structural analysis was performed for a hot section component fabricated from the base material for simulated engine operating conditions (Task G).

In the optional program, material property test procedures were developed further to obtain the material model constants from a minimum number of conventional tests (Task J). Further evaluation of the model was undertaken to consider thermal history effects (Task K). Finally, the developed constitutive model was applied and evaluated for an alternate material, Mar-M247 (Task L).

The work under this program has been conducted as a joint effort between Pratt & Whitney Aircraft (PWA) and Southwest Research Institute (SwRI) with technical assistance from Prof. Sol R. Bodner and Dr. Kevin Walker in the area of constitutive model development. The work and data base generated has been coordinated closely with another NASA funded HOST program at PWA (NAS3-23288) to develop advanced life prediction techniques for isotropic superalloy vane and blade materials.

The results of the present program have been reported annually in a series of NASA reports [1,2,6]. Results of the base program are summarized in the Second Annual Report, while this report documents those of the optional program. Some of the work in the optional program has been reported earlier in the Third Annual Report; part of these will be repeated in this report for the sake of clarity and completeness. While the base program demonstrated that both the Bodner-Partom and the Walker constitutive models were able to describe the extensive material data base with acceptable accuracy and were demonstrated to be efficiently utilized in the MARC finite element structural analysis code, the effort in the optional program has dominantly focused on the Bodner-Partom model for further study. This is not based on the advocacy of one model over the other but on the limitations of time and resources. Both models have certain advantages as well as limitations. Both will find further applications.

2.0 DEVELOPMENT OF MATERIAL TEST PROCEDURES (TASK J)

2.1 Determination of Material Constants

The procedure initiated in the base program for determining the Bodner-Partom model constants was developed further in Task J of the optional program. As a consequence of these efforts, the amount of required testing has been minimized. With the present methods, it is possible to determine the material constants of the Bodner-Partom model from conventional tensile data with supplemental creep data if slow strain-rate tensile data is not available. Since a detailed presentation of the method for constants evaluation has been presented in the third annual report [6], only a brief outline is presented here. Procedures for determining the material constants in the Walker model were established in the base program. Summaries of the Walker model, the procedures for determining model constants, and material constants for the B1900+Hf alloy were presented in [2].

A summary of the Bodner-Partom model is given in Table 2.1, while the material constants in the model are listed in Table 2.2. As illustrated in Figure 2.1, the proposed method relies on the use of work hardening data in the form of a γ versus σ plot to obtain the hardening constants, where γ is the derivative of the stress with respect to plastic work ($\gamma = d\sigma/dW_p$). An example of a γ - σ plot for B1900+Hf is shown in Figure 2.2. The γ - σ plot provides values for m_1 and m_2 (assumed to be constants), and also the value of the saturation stress, σ_s , at the test strain rate. The dependence of σ_s on strain rate is used for determining the value of n , Figure 2.3. It should be noted that the required σ_s data can be generated by either performing tensile tests on multiple specimens at various strain rates or on a single specimen

TABLE 2.1
A SUMMARY OF BODNER-PARTOM MODEL

1. Flow Law:

$$\begin{aligned}\dot{\epsilon}_{ij} &= \dot{\epsilon}_{ij}^e + \dot{\epsilon}_{ij}^p \\ \dot{\epsilon}_{ij}^p &= \lambda S_{ij} ; \dot{\epsilon}_{kk}^p = 0 \\ \text{with } S_{ij} &= \sigma_{ij} - \frac{1}{3} \delta_{ij} \sigma_{kk}\end{aligned}$$

2. Kinetic Equation:

$$\begin{aligned}D_2^p &= D_0^2 \exp \left\{ - \left[\frac{Z^2}{3J_2} \right]^n \right\} \\ \text{with } Z &= Z^I + Z^D \\ D_2^p &= \frac{1}{2} \dot{\epsilon}_{ij}^p \dot{\epsilon}_{ij}^p \\ J_2 &= \frac{1}{2} S_{ij} S_{ij} \\ \lambda^2 &= D_2^p / J_2\end{aligned}$$

3. Evolution Equations of Internal Variables:

a. Isotropic Hardening

$$\begin{aligned}\dot{Z}^I &= m_1 \left[Z_1 + \alpha Z_3 - Z^I \right] \dot{W}_p - A_1 Z_1 \left[\frac{Z^I - Z_2}{Z_1} \right]^{r_1} \\ \text{where } \dot{\alpha} &= m_2 (\alpha_1 \sin \theta - \alpha) \dot{W}_p \\ \theta &= \cos^{-1} (V_{ij} \bar{V}_{ij}) \text{ or } \theta = \cos^{-1} (u_{ij} \bar{u}_{ij}) \\ V_{ij} &= \beta_{ij} / (\beta_{kl} \beta_{kl})^{1/2}, \bar{V}_{ij} = \dot{\beta}_{ij} / (\dot{\beta}_{kl} \dot{\beta}_{kl})^{1/2} \\ u_{ij} &= \sigma_{ij} / (\sigma_{kl} \sigma_{kl})^{1/2}, \bar{u}_{ij} = \dot{\sigma}_{ij} / (\dot{\sigma}_{kl} \dot{\sigma}_{kl})^{1/2} \\ \text{with } Z^I(0) &= Z_0 ; \dot{W}_p = \sigma_{ij} \dot{\epsilon}_{ij}^p ; W_p(0) = 0 ; \alpha(0) = 0\end{aligned}$$

b. Directional Hardening

$$\begin{aligned}\dot{\beta}_{ij} &= m_2 (Z_3 u_{ij} - \beta_{ij}) \dot{W}_p - A_2 Z_1 \left[\frac{(\beta_{kl} \beta_{kl})^{1/2}}{Z_1} \right]^{r_2} v_{ij} \\ \text{with } Z^D &= \beta_{ij} u_{ij} ; Z^D(0) = 0, \beta_{ij}(0) = 0\end{aligned}$$

Material Constants: $D_0, Z_0, Z_1, Z_2, Z_3, m_1, m_2, \alpha_1$
 A_1, A_2, r_1, r_2, n , and elastic constants

In most cases can set: $r_1 = r_2, A_1 = A_2, Z_0 = Z_2$

TABLE 2.2

MATERIAL CONSTANTS IN BODNER-PARTOM CONSTITUTIVE MODEL

Constants	Descriptions
D_0	Limiting shear strain rate, sec^{-1} (assumed value)
Z_0	Initial value of the isotropic hardening variable, MPa, (T)
Z_1	Limiting (maximum) value of Z^I , MPa
Z_2	Fully recovered (minimum) value of Z^I , MPa, (T)
Z_3	Limiting (maximum) value of Z^D , MPa
m_1	Hardening rate coefficient of Z^I , MPa^{-1}
m_2	Hardening rate coefficient of Z^D , MPa^{-1}
n	Kinetic parameter, (T)
A_1	Recovery coefficient for Z^I , sec^{-1} , (T)
A_2	Recovery coefficient for Z^D , sec^{-1} , (T)
r_1	Recovery exponent for Z^I , (T)
r_2	Recovery exponent for Z^D , (T)
α_1	Limiting coefficient for non-proportional hardening effect

Note: Symbol (T) indicates general temperature dependence

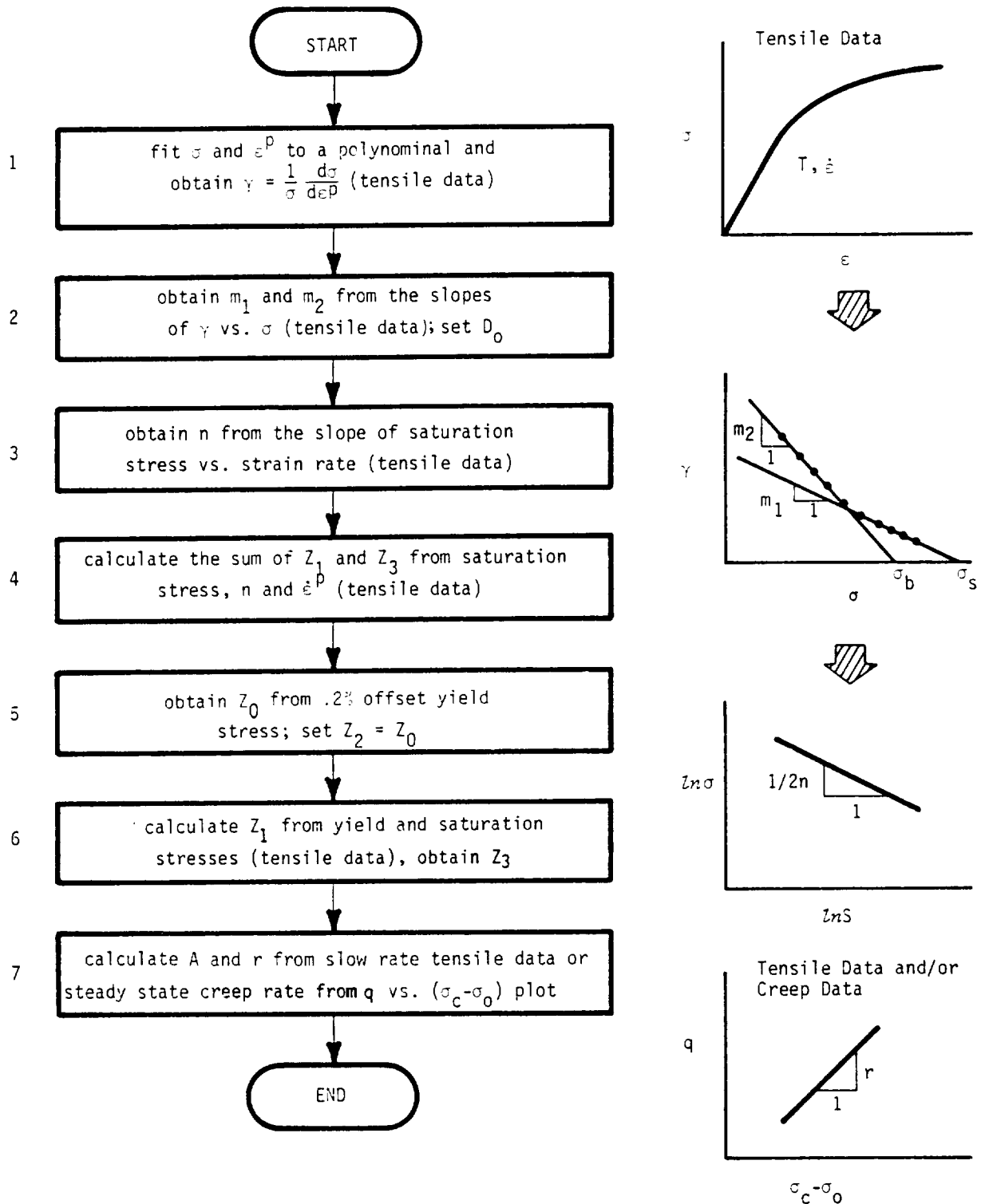


FIGURE 2.1 A FLOW CHART SHOWING A SYSTEMATIC PROCEDURE FOR EVALUATING THE MATERIAL CONSTANTS IN THE BODNER-PARTOM THEORY

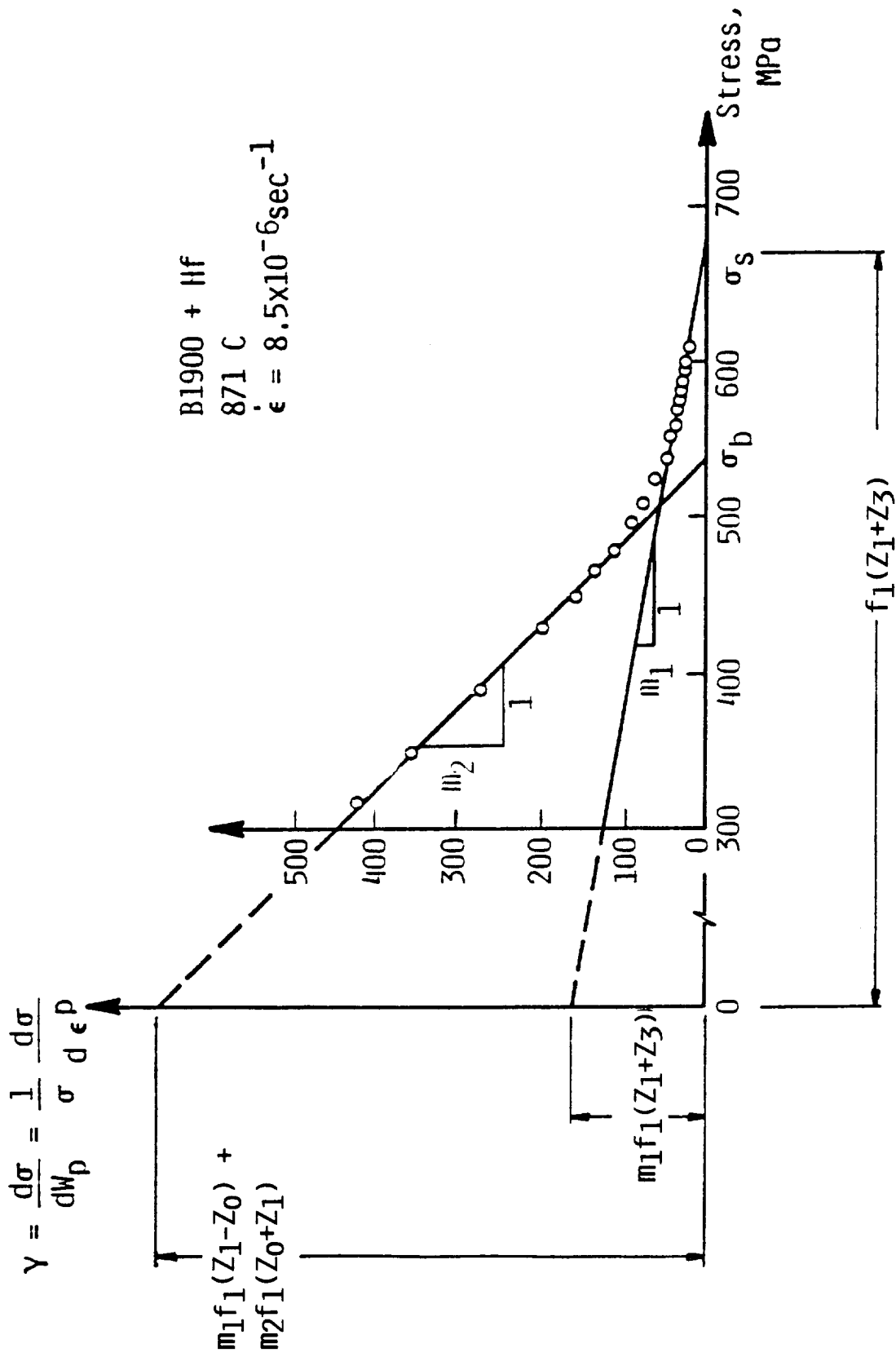


FIGURE 2.2 THE ISOTROPIC AND DIRECTIONAL HARDENING COMPONENTS OF B1900+Hf IN A γ - σ PLOT

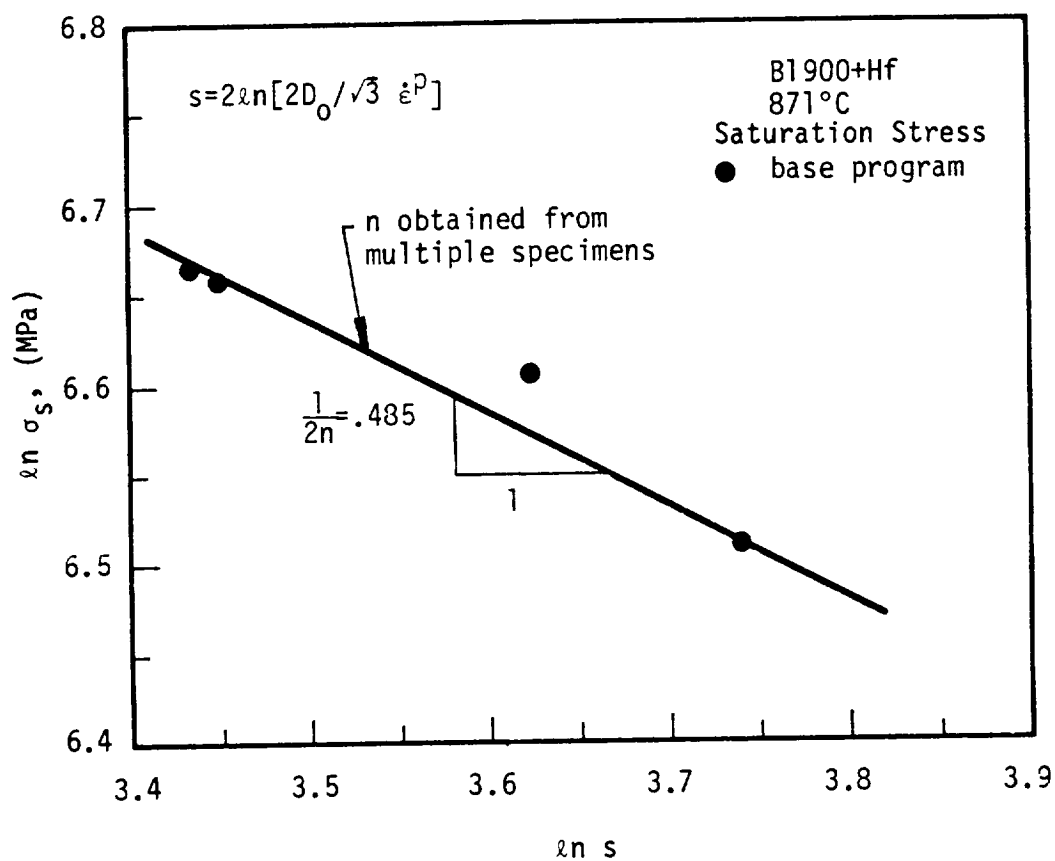


FIGURE 2.3 DETERMINATION OF THE VALUE OF n BASED ON SEVERAL STRAIN RATES

involving strain rate jumps. In the latter case, the strain-rate jump should be made after saturation has occurred. Figure 2.4 indicates that the saturation stresses at $\dot{\epsilon} = 1 \times 10^{-3} \text{ sec}^{-1}$ obtained based on these two approaches show little difference. Once n is obtained, the values for Z_0 , Z_1 , and Z_3 can be computed from the intercepts in Figure 2.2 using the 0.2% offset yield stress (or the proportional limit), the saturation stress, and an assumed value of D_0 . The procedures outlined so far are applicable for temperatures at which static thermal recovery is unimportant. For elevated temperatures at which static thermal recovery is important, the thermal recovery constants need to be evaluated. This is accomplished through the use of a plot of q vs. $\sigma_C - \sigma_0$, where

$$q = \{L_1[m_1(Z_1 - Z_0) + m_2(Z_0 + Z_3)] - m_2\sigma_C\}\sigma_C\dot{\epsilon}_C^p \quad (2.1)$$

$$\sigma_0 = [2\ln(2D_0/\sqrt{3}\dot{\epsilon}^p)]^{-1/n} Z_0$$

and σ_C and $\dot{\epsilon}_C$ are the stress and plastic strain rate under steady-state conditions. A plot of q vs $\sigma_C - \sigma_0$ for B1900+Hf is shown in Figure 2.5. As discussed in [6,7], the slope of such a plot is the thermal recovery exponent r , and the values of q and $\sigma_C - \sigma_0$ can be used to compute the thermal recovery coefficient A . This procedure is based upon assuming that $A_1 = A_2$ and $r_1 = r_2 = r$.

The proposed procedures have been applied to the B1900+Hf and Mar-M247 materials in this program with good results. They have also been applied to HY-80, A533B steels, and Astroloy 700 in other programs at SwRI. In all cases, very satisfactory results are obtained.

A limited amount of effort has been devoted to examining the possible effects of grain size and surface coating on the model constants through

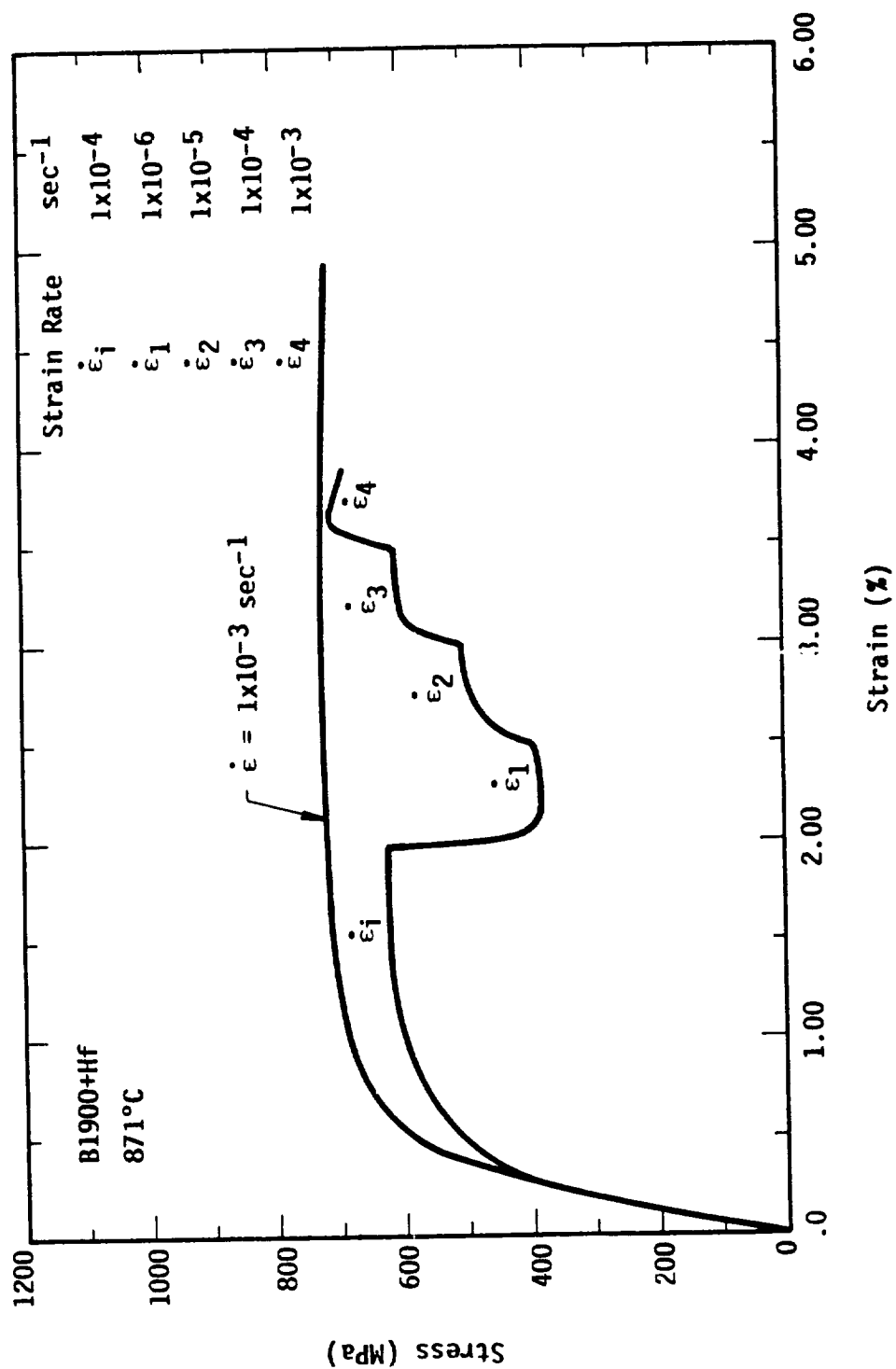


FIGURE 2.4 COMPARISON OF MONOTONIC TENSILE AND JUMP TEST RESULTS OF B1900+Hf

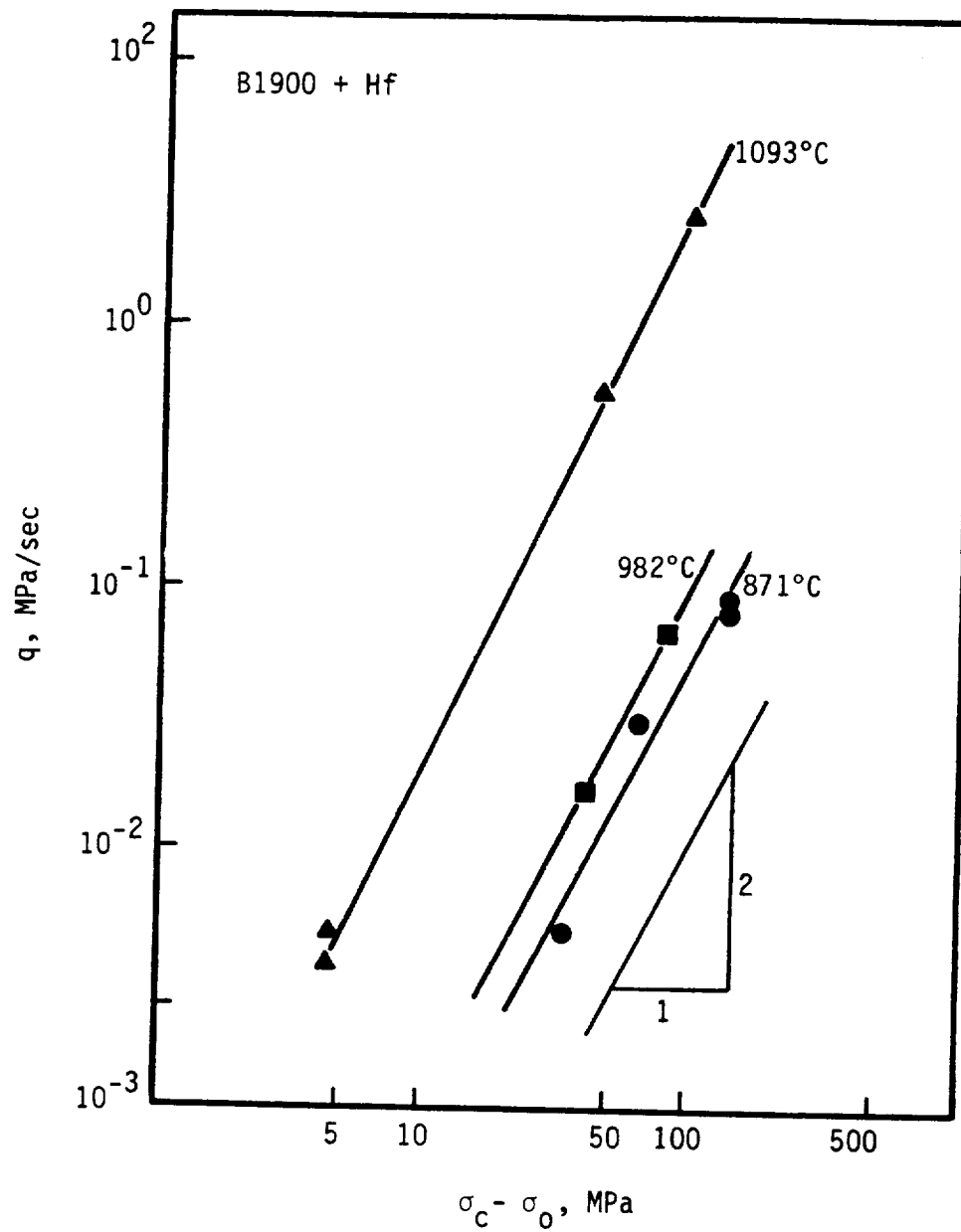


FIGURE 2.5 DETERMINATION OF THE VALUE OF r BASED ON THE SLOPES OF THE q VS $\sigma_c - \sigma_o$ CURVES FOR B1900+Hf

their influence on the constitutive behavior of the alloys. Figures 2.6-2.8 show that for the B1900+Hf material investigated, grain size has only a small effect on the stress-strain behavior under either tensile or cyclic loading. The effect of a thermal barrier surface coating on the deformation behavior of B1900+Hf was investigated by performing a TMF test and those results will be presented in the next section. It was also found that this coating also had a negligible effect on the model constants.

2.2 Strain-Aging Effects

Step strain-rate tensile tests in the optional program indicated that negative strain rate sensitivity, which is a consequence of strain aging effects, is present in B1900+Hf at a temperature range bounded above by about 760°C, and also exists in Mar-M247 in the temperature range of 23-648°C. Under this circumstance, certain predictions of the Bodner-Partom model do not correlate well with the experimental data because strain aging effects are not included in the model. In addition, it has been suggested that strain aging can lead to thermal-history effects which can potentially invalidate isothermally based constitutive models subjected to nonisothermal loading histories [8,10]. As a result, a small effort has been attempted to incorporate the strain aging effect into the Bodner-Partom model in order to improve the accuracy of the model in the regime of influence. A strain aging term is present in the Walker model [2]; thus, modification of this model is unnecessary.

Strain aging effects are primarily due to the interaction of dislocations and solute atoms with moving dislocations [11-13]. Common observations associated with strain aging are: (1) serrated flow, (2) negative strain rate sensitivity, and (3) a plateau in the temperature dependence of

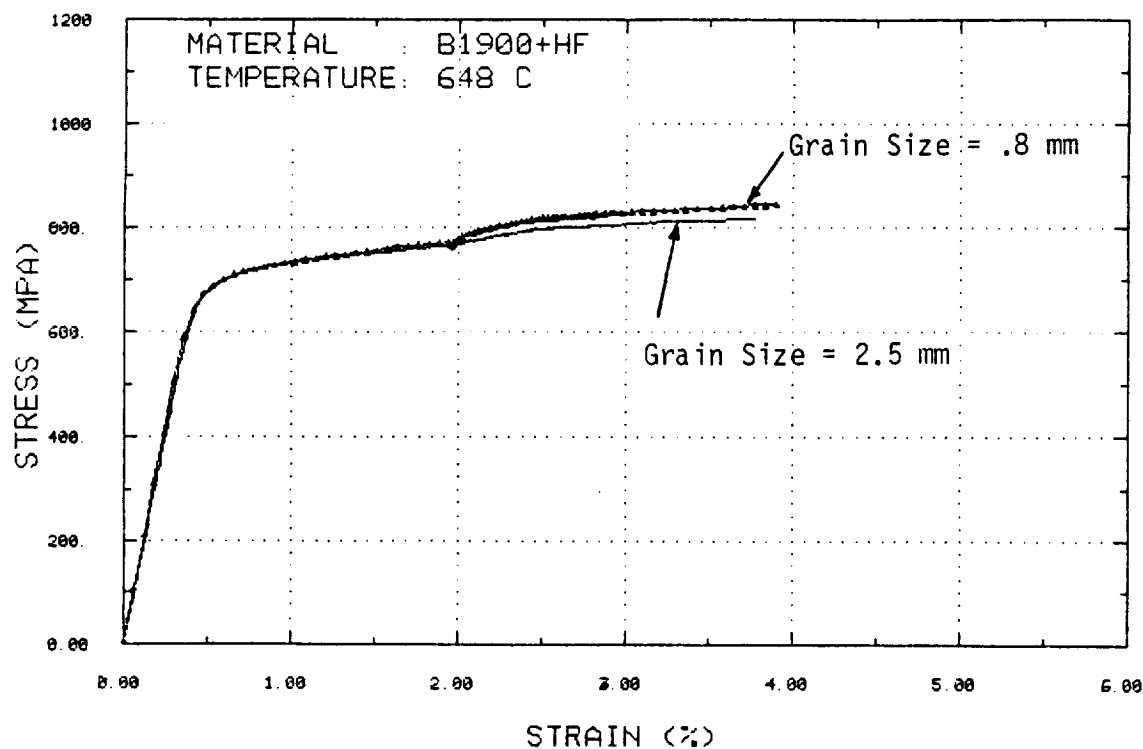


FIGURE 2.6 COMPARISON OF JUMP TEST RESULTS FOR B1900+HF SPECIMENS AT 648°C AND WITH TWO DIFFERENT GRAIN SIZES.

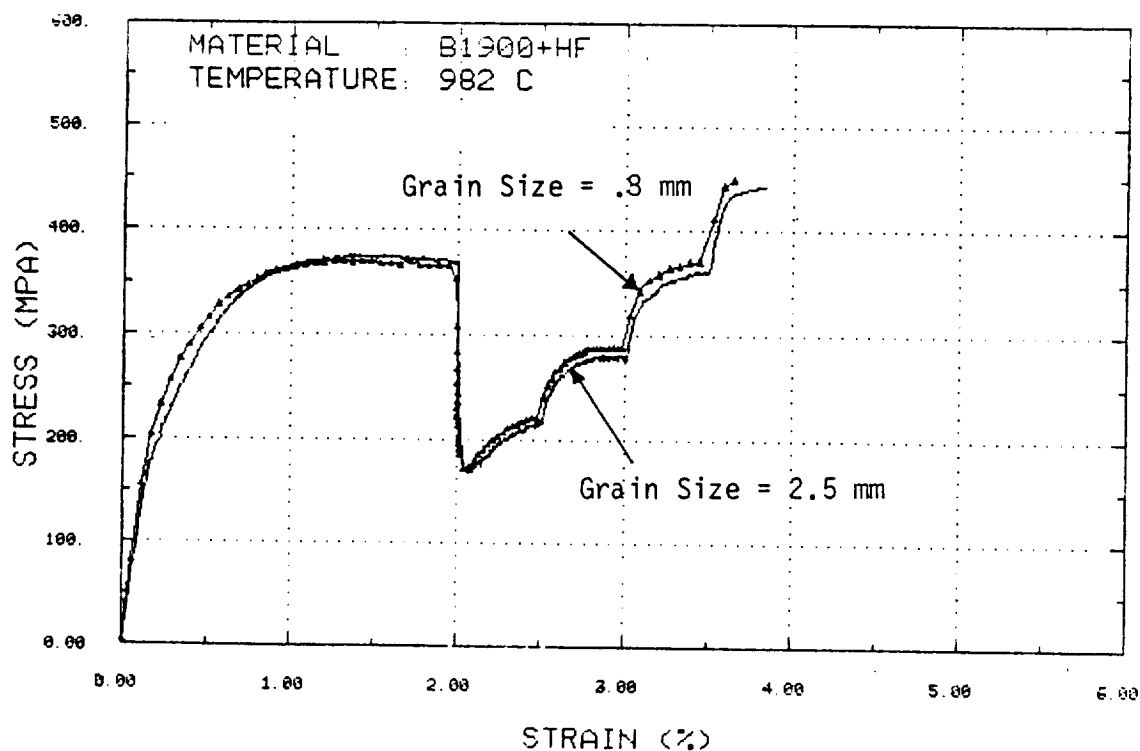
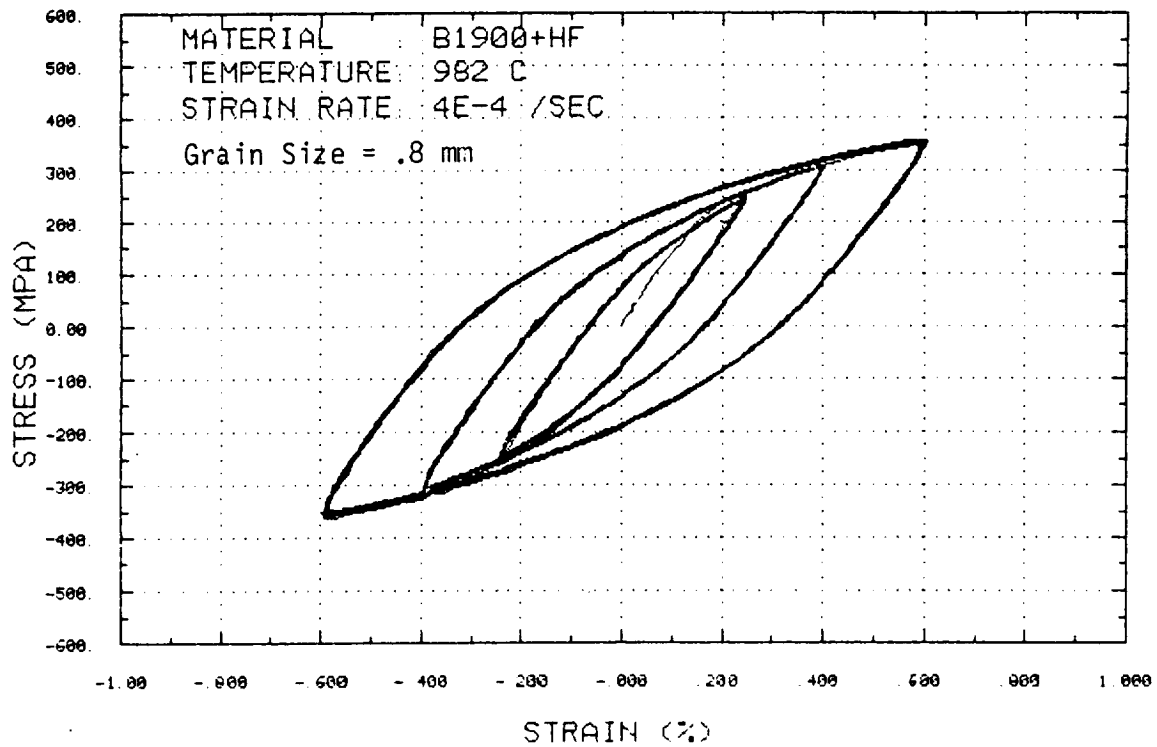
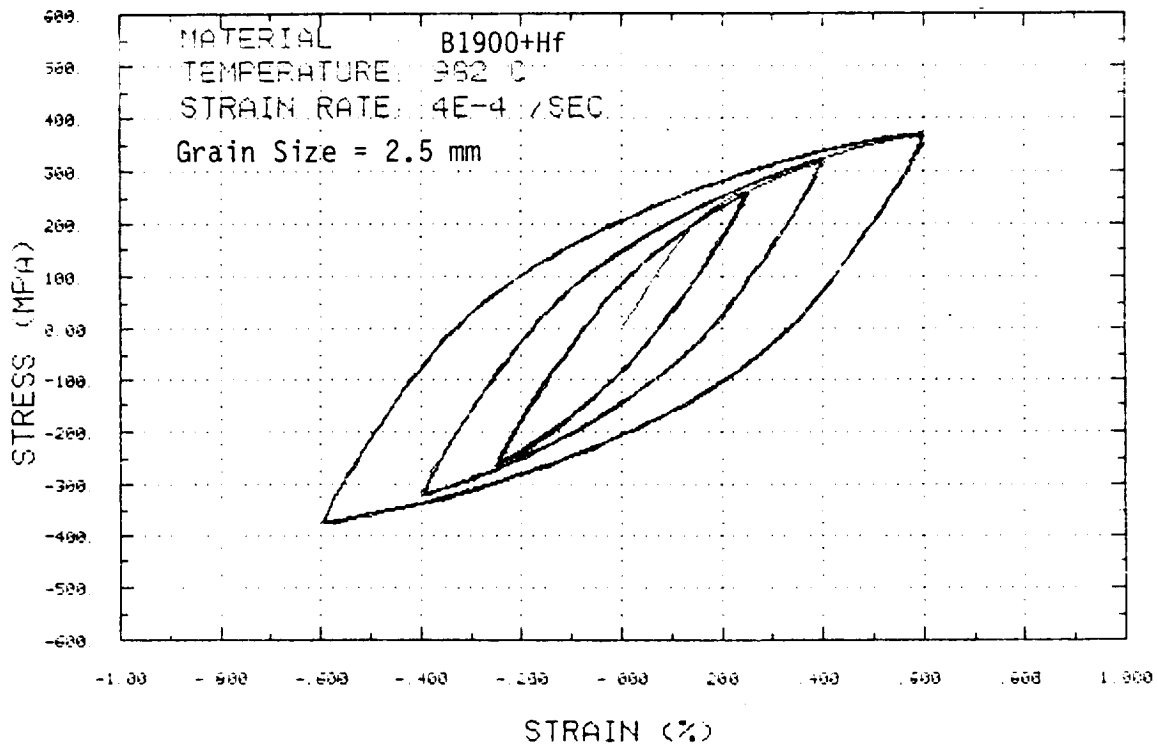


FIGURE 2.7 COMPARISON OF JUMP TEST RESULTS FOR B1900+HF SPECIMENS AT 982°C AND WITH TWO DIFFERENT GRAIN SIZES.



(a)



(b)

FIGURE 2.8 COMPARISON OF CYCLIC BEHAVIOR OF B1900+Hf SPECIMENS WITH TWO DIFFERENT GRAIN SIZES: (a) .8 mm, AND (b) 2.5 mm.

the yield stress. In a review paper, Schmidt and Miller [12] indicated that solute enhanced strain hardening can be due to a number of processes which include precipitation and the solute affecting the rate of dislocation multiplication, annihilation, or the recovery of dislocation structures. As indicated earlier, strain aging and precipitation have also been linked to thermal history effects [8-10].

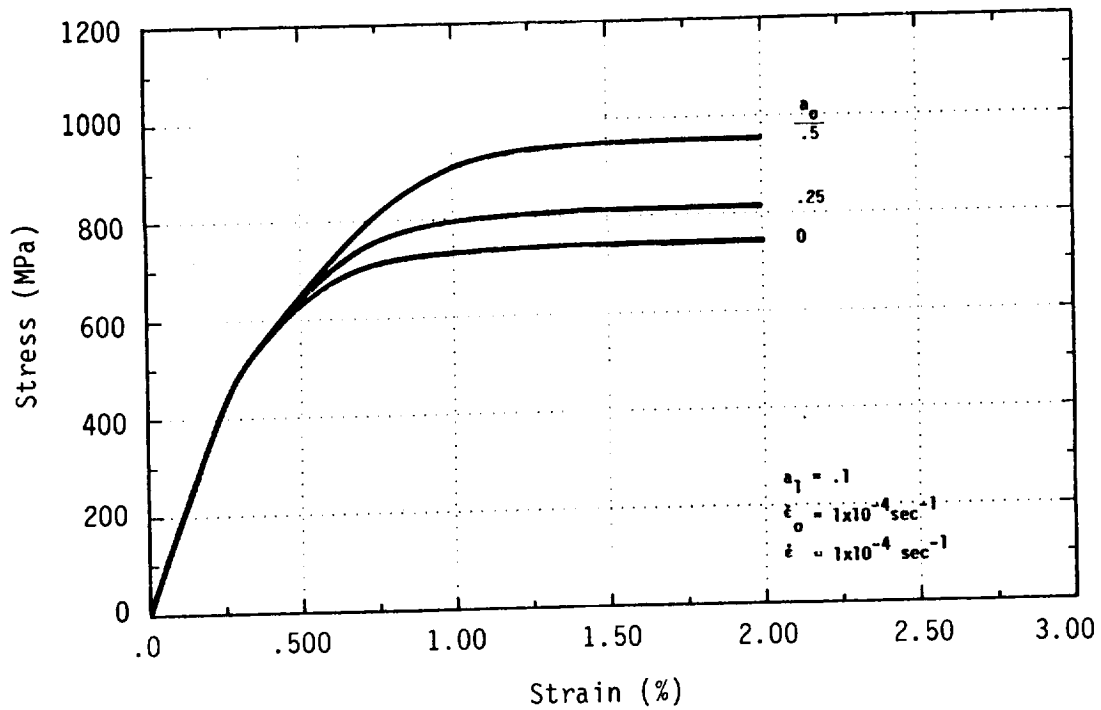
Schmidt and Miller [14] have incorporated a strain aging term into the unified constitutive equations of Miller [15] by introducing a function which is added to the isotropic hardening variables. The functional form proposed by Schmidt and Miller to represent solute strengthening is:

$$F(\text{solute hardening}) = a_0 \exp [-a_1 \log(\dot{\epsilon}/\dot{\epsilon}_0)^2] \quad (2.2)$$

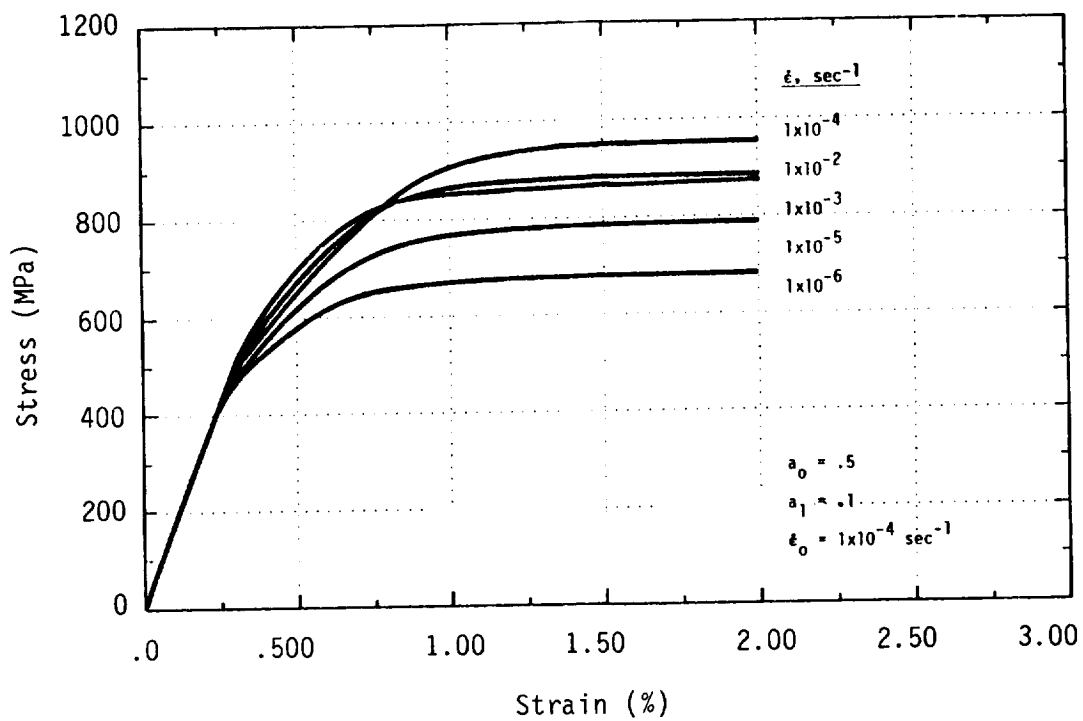
where a_0 , and a_1 are constants and $\dot{\epsilon}$ and $\dot{\epsilon}_0$ are the applied and reference effective strain rates. It is noted that this procedure is an empirical method for representing the effect of strain aging and does not correspond directly with physical processes. This functional relationship was adopted in the Walker model for incorporating strain aging effects [2]. Walker, however, considered solute hardening to be directional in character and the strain aging effects were incorporated in the evolution equation for the equilibrium stress [2]. A possible method for modifying the Bodner-Partom model to include strain aging effects would be to adopt Equation (2.2) into the evolution equation for the directional hardening variable, β_{ij} , so that

$$\dot{\beta}_{ij} = m_2 [Z_3 U_{ij} - \beta_{ij} (1-a)] \dot{W}_p - (\text{thermal recovery term}) \quad (2.3)$$

where a represents the strain aging term given by Equation (2.2). The constants a_0 , a_1 , and $\dot{\epsilon}_0$ must be evaluated from tensile data in the strain aging regime. Figures 2.9(a) and (b) show the stress-strain results by



(a)



(b)

FIGURE 2.9 MODEL REPRESENTATIONS OF B1900+Hf AT 649°C USING A STRAIN AGING TERM: (a) EFFECTS OF a_0 IN THE STRAIN AGING TERM ON THE STRESS-STRAIN CURVE, AND (b) STRAIN AGING EFFECT SIMULATED WITH THE BODNER-PARTOM MODEL USING $a_0 = .5$, $a_1 = .1$, and $\dot{\epsilon}_0 = 1 \times 10^{-4} \text{ sec}^{-1}$

systematically varying the parameters a_0 , a_1 , $\dot{\epsilon}_0$, and strain rate using the material constants for B1900+Hf at 649°C. The results indicate that a strength peak can be produced at a strain rate of $\dot{\epsilon} = \dot{\epsilon}_0$ so that the flow stress decreases when the strain rate is either increased or decreased, which simulates one of the characteristics of the strain aging effect. The magnitude of the flow stress enhancement depends on the value of the material constants a_0 . Calculations of tensile curves with several strain rate changes, however, indicate that Equation (2.3) would not produce a strain-rate independent inelastic flow behavior. Although a negative strain-rate dependence is obtained, transient overshoots in stress, not observed in B1900+Hf, are often accompanied with the strain rate changes, Figure 2.10.

Another characteristic of the strain aging phenomenon is the increase in strength with increasing temperature, resulting in a plateau or strength peak in the temperature dependence of yield strength. Such a strength peak exists at $\approx 648-760^\circ\text{C}$ in B1900+Hf and Mar-M247. However, the strength peak in this intermediate temperature range is generally attributed to the deformation characteristics of the γ' phase and is not due to strain aging [16]. It should be noted that a strength peak is also observed in single crystal and polycrystalline Ni_3Al (γ') at the intermediate temperature range. The mechanisms of the strength peak in γ' appears to be dislocation interactions resulting from cross-slip from (111) planes to (010) planes [16]. The latter type of dislocations are sessile and they tend to interact with subsequent dislocation movements on the (111) planes. The consequences are anomalous temperature-strength behavior, asymmetric flow, and unusual hardening behavior. Since B1900+Hf and Mar-M247 contain approximately 60% ($\pm 5\%$) volume fraction of γ' , it is possible that the observed temperature-strength behavior and thermal-history effects in Ni-alloys are caused by Ni_3Al

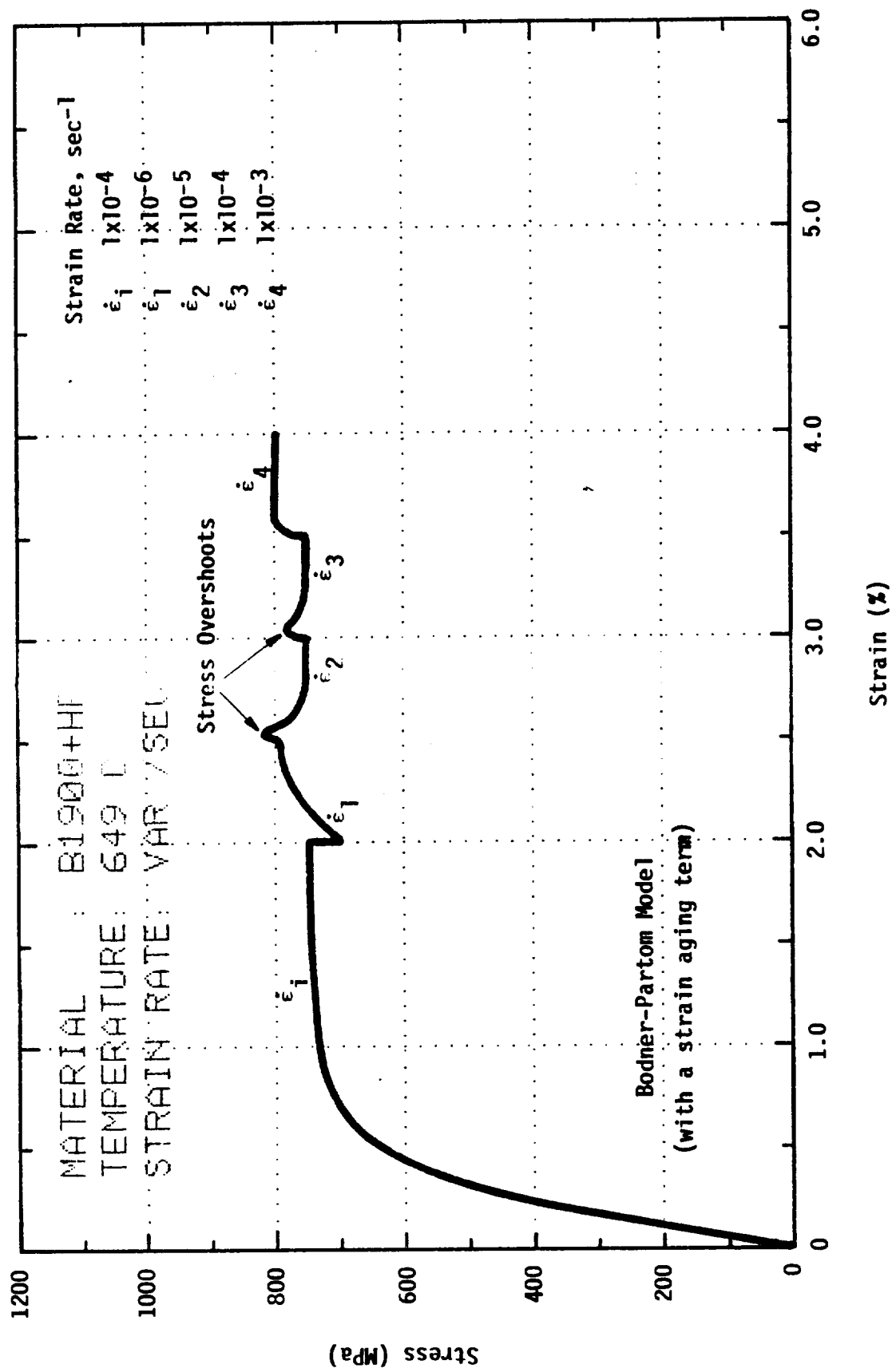


FIGURE 2.10 STRESS-STRAIN CURVE CALCULATED WITH THE BODNER-PARTOM MODEL WITH A STRAIN AGING TERM

rather than strain aging. Because of the uncertainties of the underlying mechanisms, further attempts to include strain aging effects in the Bodner-Partom model were discontinued.

Unusual cyclic hardening effects, to be presented in the next section, were observed in TMF cycling of B1900+Hf in the temperature range of 538-760°C; transmission electron microscopy revealed that the anomalous hardening behavior originated from dislocation interactions in the γ' phase.

2.3 Nonproportional Hardening

As discussed in [6], the Bodner-Partom model somewhat overpredicts the stress response of Mar-M247 subjected to 90° out-of-phase tension-torsion strain cycling. Similar results were also observed in the calculations for B1900+Hf [2]. In order to examine this effect, exercises were performed using the Bodner-Partom model and the constants for Mar-M247 at 982°C. The loading sequence was: (1) uniaxial strain cycling under an axial strain range of $\pm 4\%$ for 5 cycles, (2) 90° out-of-phase tension-torsion for two and one-half cycles at an effective strain range of $\pm 4\%$, and (3) return to axial loading as described in Step (1). The calculated σ vs. $\sqrt{3}\tau$ responses associated this sequence is shown in Figure 2.11(a). It is noted that cyclic saturation is almost attained after uniaxial cycling for 5 cycles. Additional cyclic hardening, however, is observed when the 90° out-of-phase cycle is applied. This nonproportional hardening saturated rapidly, and the σ - $\sqrt{3}\tau$ locus becomes stable in the second cycle. Detailed examination of the internal variables indicated that the calculated nonproportional hardening effect is the consequence of an increase of the directional hardening variable, Z^D , when the loading condition is changed from uniaxial to out-of-phase loading. This

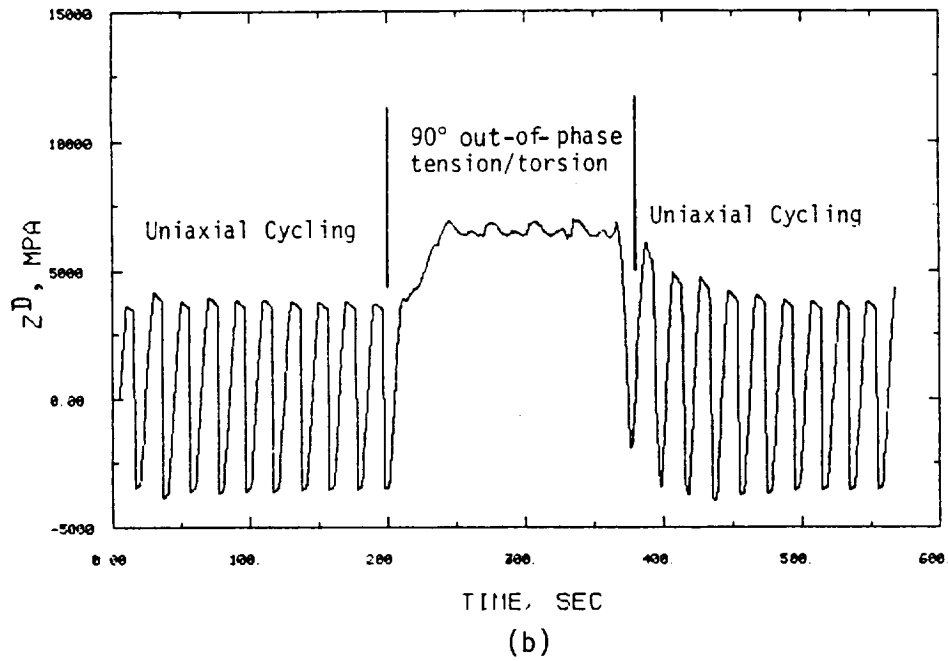
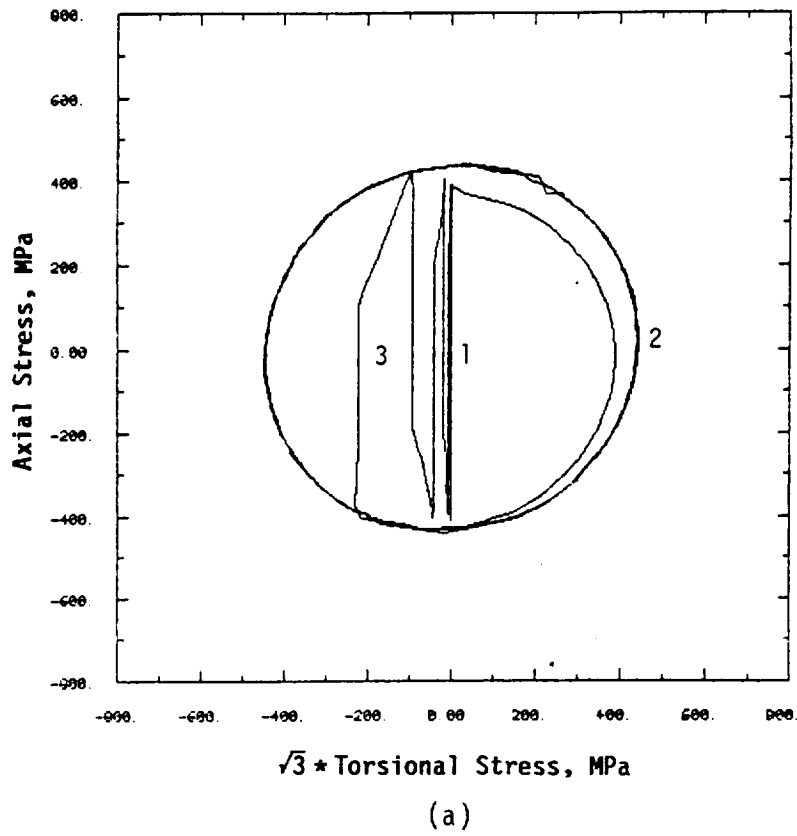


FIGURE 2.11 BODNER-PARTOM MODEL CALCULATION FOR MAR-M247 UNDER
 (1) UNIAXIAL CYCLING FOR 5 CYCLES, FOLLOWED BY
 (2) 90° OUT-OF-PHASE CYCLING FOR 2-1/2 CYCLES, AND
 (3) UNIAXIAL CYCLING FOR 5 CYCLES: (a) σ - $\sqrt{3}\tau$ PLOT,
 AND (b) TIME HISTORY OF Z^D

nonproportional hardening effect is transient and diminishes as the loading condition is returned to uniaxial loading. The corresponding history for the directional hardening variable, Z^D , is shown in Figure 2.11(b).

A possible explanation for this transient nonproportional hardening is that the conditions for cyclic saturation under uniaxial loading and non-proportional, multiaxial loading are different. For the latter case, it appears that

$$Z^D = \beta_{ij} u_{ij} = \text{constant} \quad (2.4)$$

during cyclic saturation under a 90° out-of-phase strain cycle. As a result,

$$\dot{Z}^D = \beta_{ij} \dot{u}_{ij} + \dot{\beta}_{ij} u_{ij} = 0 \quad (2.5)$$

$$\dot{Z}^I = 0 \quad (2.6)$$

would be the conditions for cyclic saturation under nonproportional loading. On the other hand, the condition for cyclic saturation under uniaxial straining is $\dot{Z}^I = 0$, but Z^D varies continually with cycling and its amplitude depends on the cycle strain range.

This type of nonproportional hardening effect appears to be present in B1900+Hf and Mar-M247. The effect, however, is quite small and becomes saturated within one cycle. The overprediction of the axial stress by the Bodner-Partom model for 90° out-of-phase loading appears to be primarily due to overestimation of this transient, nonproportional hardening effect. Further examinations of the calculated results and Equation (2.5) revealed that the discrepancies can be completely eliminated by an adjustment of the thermal recovery constant A_2 in the expression for $\dot{\beta}_{ij}$, as illustrated in

Figure 2.12. Since the magnitude of directional hardening B_{ij} is essentially constant under 90° out-of-phase loading, it would be sensitive to the thermal recovery constant at elevated temperature. It may therefore not be proper to set $A_1=A_2$ when dealing with multiaxial nonproportional loading at elevated temperature.

2.4 Update on Finite-Element Analysis of the Benchmark Notch Specimen

Finite element analyses of the benchmark notch-round specimens were performed in the base program using the MARC Code [17] and the Walker constitutive model. The Bodner-Partom model was not used in these numerical applications. In the last two years, there has been an effort at SwRI to develop an in-house elastic-viscoplastic finite-element code which is suitable for high strain rate ($> 10^4 \text{ sec}^{-1}$) structural applications. This finite-element code, which has been completed during the last year, uses the Bodner-Partom model with isotropic hardening. Because of the availability of this new finite-element code, an analysis of the benchmark notch-round specimen subjected to a monotonic load was performed. The analysis was intended as a check of the finite-element code and was carried out in another SwRI project at no cost to NASA. Since the results are of interest to this program, the benchmark notch calculations are reported here also.

Figure 2.13 shows the finite-element mesh used in the benchmark notch calculations. It consists of 283 axis-symmetric elements with 1832 active degrees of freedom. Since the benchmark notch test was conducted under displacement control, the load-line displacements were prescribed on the boundary elements. The finite-element calculations were performed on a VAX/780 computer, and the CPU time was approximately one and one-half hours.

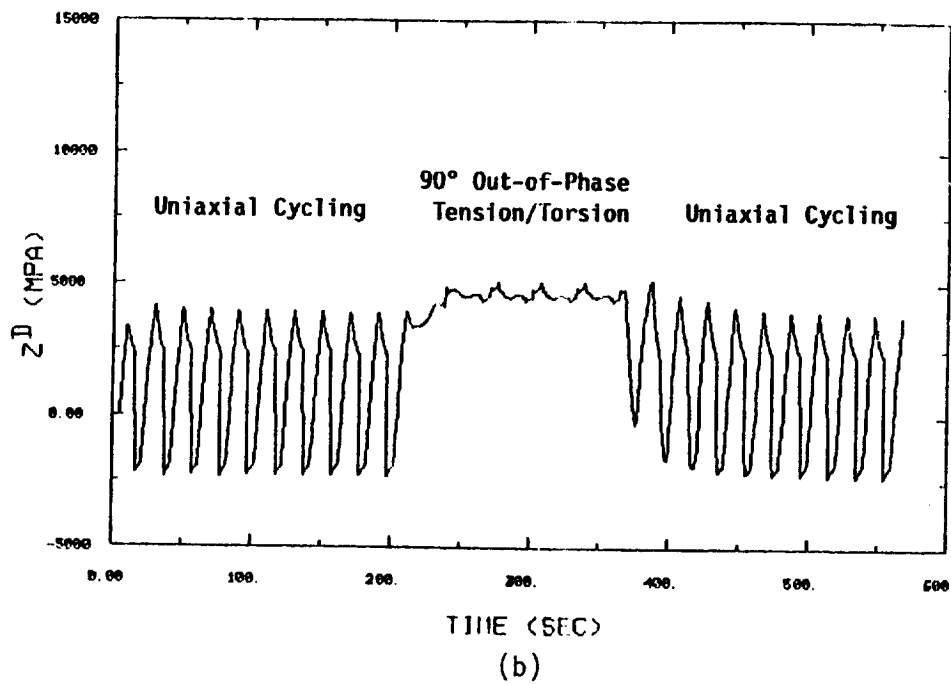
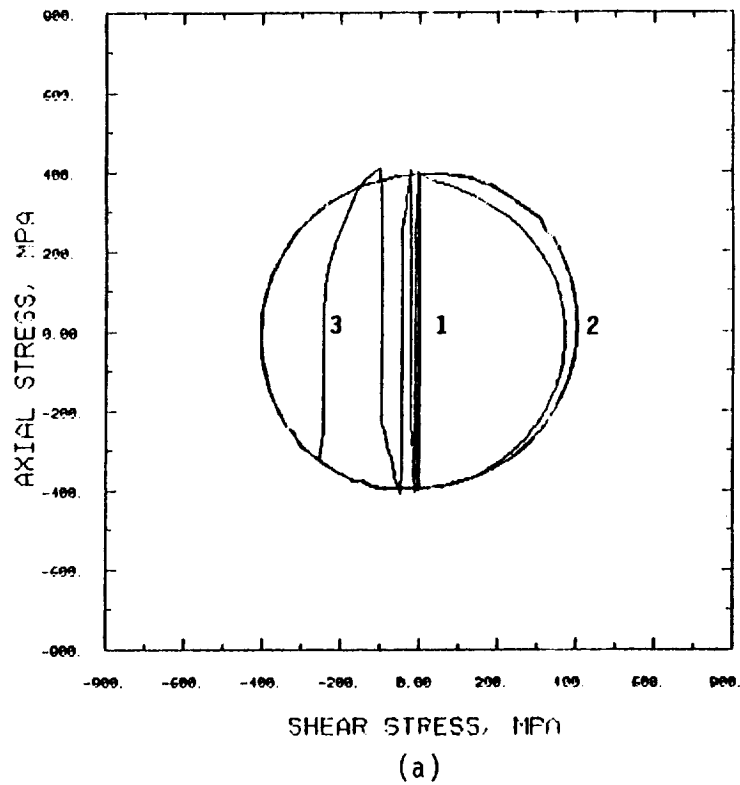


FIGURE 2.12 BODNER-PARTOM MODEL CALCULATION FORMAR-M247 UNDER THE SAME LOADING HISTORIES AS IN FIGURE 2.11; (a) $\sigma-\sqrt{3}\tau$ PLOT, AND (b) TIME HISTORY OF Z^D DURING CYCLING. Results are obtained by increasing the value of A_2 by a factor of 10.

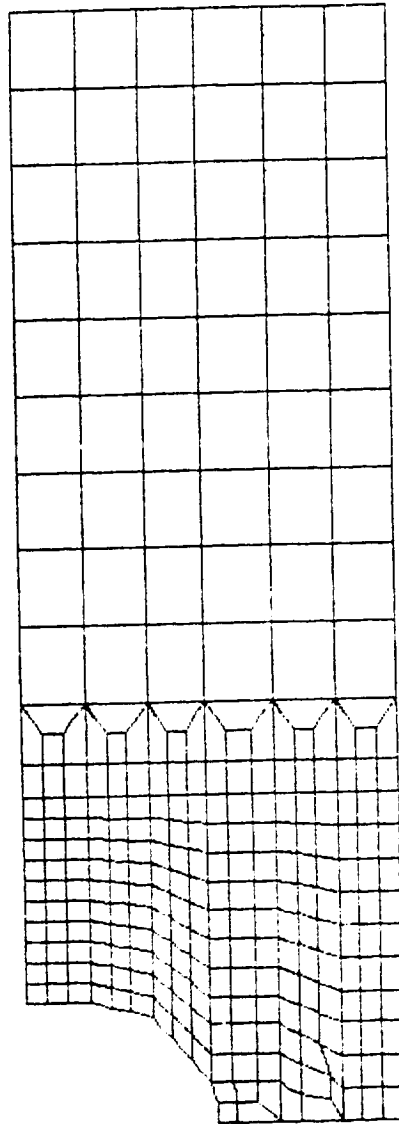


FIGURE 2.13 FINITE-ELEMENT MESH OF THE BENCHMARK NOTCH-ROUND SPECIMEN

Figure 2.14 shows the excellent agreement between experiment and finite-element calculation based on the Bodner-Partom model. Previously reported, the finite-element calculations based on the Walker model and MARC code overpredicted the applied load at a given diametrical displacement. These finite-element results, together with previous results on the turbine blade analysis, indicate that the unified constitutive models are viable for structural applications based on the finite-element method.

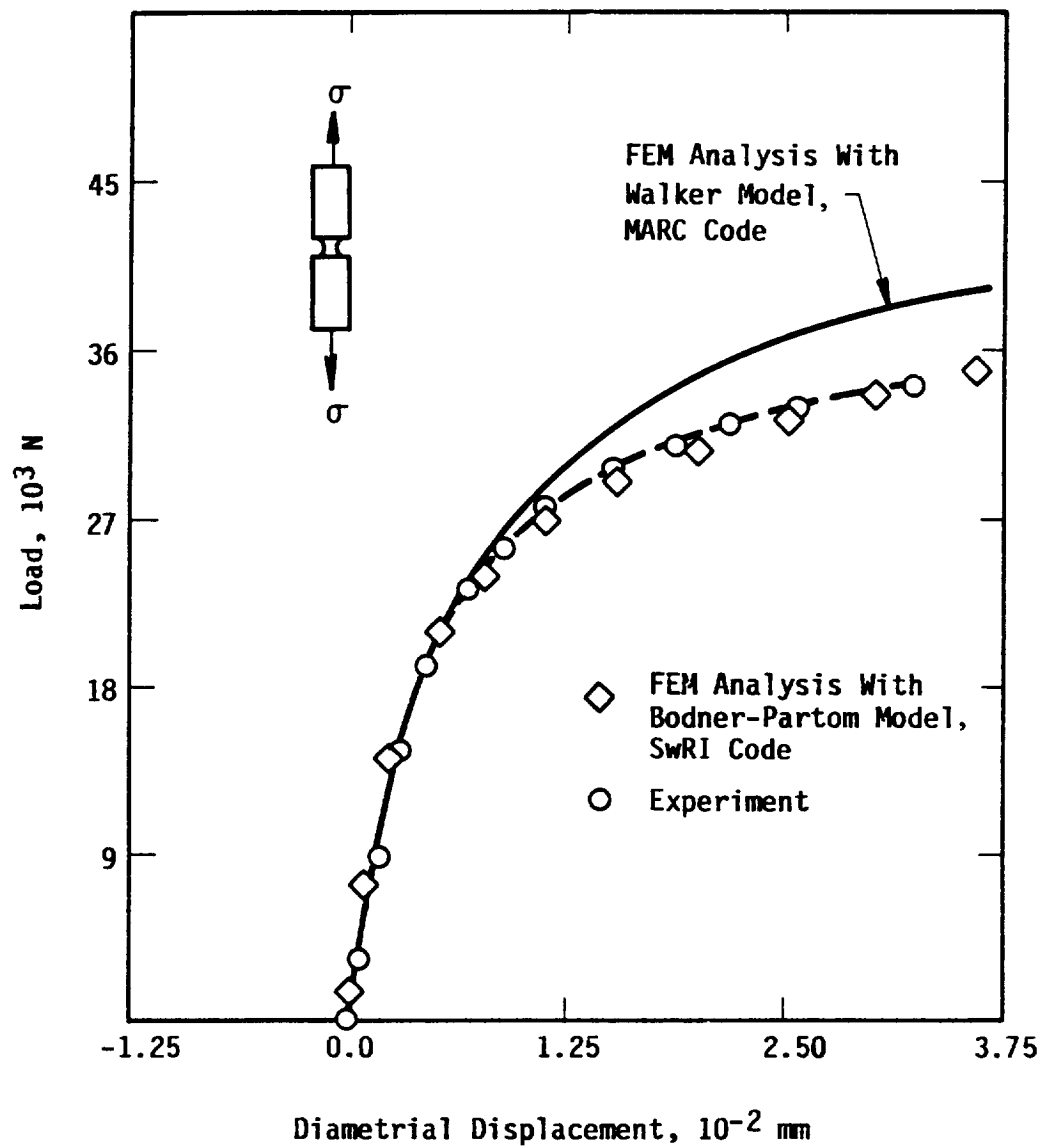


FIGURE 2.14 COMPARISON OF MODEL PREDICTIONS WITH EXPERIMENTAL RESULTS OF THE BENCHMARK NOTCHED SPECIMEN UNDER MONOTONIC LOADING

3.0 THERMAL HISTORY EFFECTS (TASK K)

3.1 Thermal History Effects--Literature Survey

A literature survey was conducted as part of Task K1 to assess the effects of thermal history on constitutive behavior and their implications with regard to constitutive modeling based on the unified approach. The literature survey indicated that the inelastic response of metals [8,9,18] including yield surface determinations [19], depends, in general, not only on the current temperature but also on the thermal history. This is analogous to the fact that inelastic deformation depends on the deformation history as well as on the current stress. In some instances, the hardening response of materials is observed to differ under isothermal and nonisothermal conditions which has generally been attributed to either strain aging [8,9] or other microstructural effects [18].

Thermal history effects are usually modeled in the unified constitutive approach by including thermal terms in the evolution equations for the isotropic and directional hardening variables [10,20]. The general forms of the evolution equations for the isotropic hardening variables, K , and the directional hardening variable, Ω_{ij} , are as follows [20]:

$$\dot{K} = F(J_2, K, T) = h_1(K, T)\dot{M}_1 - r_1(T, K) \quad (3.1)$$

$$\dot{\Omega}_{ij} = G(\sigma_{ij}, \Omega_{ij}, T) = h_2(\Omega_{ij}, T)\dot{M}_{ij} - d(\Omega_{ij}, T)\dot{N}_{ij} - r_2(\Omega_{ij}, T)V_{ij} \quad (3.2)$$

for isothermal loading, and

$$\dot{K} = h_1(K, T)\dot{M}_1 - r_1(T, K) + \theta_1(K, T)T \quad (3.3)$$

$$\begin{aligned} \dot{\Omega}_{ij} = & h_2(\Omega_{ij}, T)\dot{M}_{ij} - d(\Omega_{ij}, T)\dot{N}_{ij} - r_2(\Omega_{ij}, T)V_{ij} \\ & + \theta_2(\Omega_{ij}, T)T W_{ij} \end{aligned} \quad (3.4)$$

where h_1 , r_1 , and θ_1 represent, respectively, the hardening, static thermal recovery, and thermal history functions for K; h_2 , d , r_2 , and θ_2 represent the hardening, dynamic recovery, static thermal recovery, and thermal history functions for α_{ij} , respectively; \dot{M}_{ij} and \dot{N}_{ij} are the hardening measure; V_{ij} and W_{ij} are directional indices. Specific forms of \dot{M}_{ij} , \dot{N}_{ij} , V_{ij} , and W_{ij} are given in [20].

The appropriate forms of θ_1 and θ_2 are not well established at this time. A general approach for modeling thermal history effects is to express θ_1 and θ_2 as functions of the internal variable and temperature [10,20]. New internal variables may also be introduced [18]. In a particular approach [2,5,21], θ_1 and θ_2 are taken as functions represented by the temperature derivatives of the evolution equations for isothermal conditions [2,5,21].

$$\theta_1(T) = F(J_2, K, T),_T \quad (3.5)$$

$$\theta_2(T) = G(\alpha_{ij}, T, \sigma_{ij}),_T \quad (3.6)$$

which generally contain terms involving the temperature derivative of material constants. Temperature-dependent material constants in the kinetic equation are treated in a similar manner. Comparisons of thermomechanical constitutive data of B1900+Hf and calculations using the Bodner-Partom and Walker models at SwRI and PW&A indicated that this approach led to reasonably good agreement between theory and experiment [2] suggesting that thermal history effects associated with TMF cycling can be predicted based on isothermal data alone. No additional temperature rate (T) terms other than those represented by Eqs. (3.5) and (3.6) were needed. Whether or not this conclusion is valid for other materials or thermal paths remains an open question.

Recent thermomechanical studies [8,9] report response characteristics under nonisothermal conditions which are substantially different from those manifested under isothermal circumstances. While these studies clearly demonstrate the presence of strain aging and thermal history effects on the behavior of certain structural alloys, the results do not contradict the possibility of predicting thermal history effects by an appropriate constitutive model which uses material constants based on isothermal data. A systematic evaluation of model prediction against experimental results obtained under a variety of thermomechanical paths is required to resolve this issue.

Based on the results of this literature survey, SwRI recommended that efforts in Task K2 be directed to examining thermal history effects in B1900+Hf by thermomechanical cycling: (1) at a temperature range where strain aging effect is prominent, (2) at a temperature range where microstructure changes such as precipitation or resolution of precipitates could occur, (3) at various heating rates, (4) using different thermal paths, and (5) with elastic as well as inelastic paths. The experimental efforts have been coupled with parallel analytical efforts to determine whether or not thermal history effects can be predicted using the Bodner-Partom model in conjunction with material constants obtained solely from isothermal data.

3.2 Thermal History Effects: Numerical Integration

The various unified constitutive models proposed in the literature contain material constants of which some are temperature dependent. These temperature-dependent constants can include the initial and, in certain models, the limiting values of the hardening variables, and also terms in the kinetic equation. Using these constitutive models for thermomechanical

loading requires a judicious means of tracing and updating the current values of the hardening variables and the other materials constants during temperature changes. A theoretical framework for this purpose is presented in this section. The results of this investigation also indicate the general forms of evolution equations for the hardening variables when temperature rate terms are included.

At a temperature T and a temperature rate \dot{T} ($\dot{T} = dT/dt$), all of the unified constitutive models can be represented in the following form:

$$\dot{\underline{\varepsilon}}^P = \underline{f}(\underline{\sigma}, \underline{x}, T) \quad (3.7)$$

$$\dot{\underline{x}} = \underline{g}(\underline{\sigma}, \underline{x}, T) \quad (3.8)$$

$$\dot{\underline{\sigma}} = \underline{D}(\dot{\underline{\varepsilon}} - \dot{\underline{\varepsilon}}^P) + \theta(\alpha, \underline{D}) \dot{T} \quad (3.9)$$

$$\begin{aligned} \text{with} \quad \theta(\alpha, \underline{D}) = & \left[\underline{\varepsilon} - \underline{\varepsilon}^P - \alpha(T - T_0) \right] \frac{\partial \underline{D}}{\partial T} \\ & - \underline{D} \left[(T - T_0) \frac{\partial \alpha}{\partial T} + \alpha \right] \end{aligned} \quad (3.10)$$

where $\underline{\varepsilon}$, $\underline{\varepsilon}^P$, $\underline{\sigma}$, and \underline{x} are the total strain, inelastic (plastic) strain, stress, and hardening variable vectors, respectively; \underline{D} is the stiffness matrix and α is the coefficient of thermal expansion. The dot above the variables denotes the derivative of the variable with time. It should be noted that Equation (3.10) is obtained by differentiating Hooke's law with respect to time for thermomechanical loading conditions by including effects of temperature change on the elastic moduli and coefficient of thermal expansion.

Using Tanaka's approach [22], an implicit time operator is used for integrating the rate equations in the unified models. The incremental stress vector $\Delta \underline{\sigma}$, strain vector $\Delta \underline{\epsilon}$, nonelastic strain vector $\Delta \underline{\epsilon}^p$, and structural variable vector $\Delta \underline{x}$, occurring in the time interval $\Delta t = b_t - a_t$ can be defined as

$$\Delta \underline{\sigma} = \Delta t \{ (1-\eta) \underline{\dot{\sigma}}_a + \eta \underline{\dot{\sigma}}_b \} , \quad (3.11)$$

$$\Delta \underline{\epsilon} = \Delta t \{ (1-\eta) \underline{\dot{\epsilon}}_a + \eta \underline{\dot{\epsilon}}_b \} , \quad (3.12)$$

$$\Delta \underline{\epsilon}^p = \Delta t \{ (1-\eta) \underline{\dot{\epsilon}}_a^p + \eta \underline{\dot{\epsilon}}_b^p \} , \quad (3.13)$$

$$\Delta \underline{x} = \Delta t \{ (1-\eta) \underline{\dot{x}}_a + \eta \underline{\dot{x}}_b \} , \quad (3.14)$$

in which $b(\)$ and $a(\)$ represent the values of the parameters () at $t = b$ and $t = a$, respectively. The implicit time operator, η , has values ranging from 0 to unity, i.e.,

$$0 \leq \eta \leq 1 \quad (3.15)$$

It should be noted that the numerical scheme reduces to Euler's explicit method when $\eta = 0$, and to Euler's implicit method when $\eta = 1$.

The values of $\underline{\dot{\epsilon}}^p$ and $\underline{\dot{x}}$, at time $t = b$ can be approximated by their previous values and their gradients at $t = a$ through Taylor's expansion:

$$\underline{\dot{\epsilon}}_b^p = \underline{\dot{\epsilon}}_a^p + \underline{\dot{\epsilon}}_{a,\sigma}^p \Delta \underline{\sigma} + \underline{\dot{\epsilon}}_{a,x}^p \Delta \underline{x} + \underline{\dot{\epsilon}}_{a,T}^p \Delta T \quad (3.16)$$

$$\underline{\dot{x}}_b = \underline{\dot{x}}_a + \underline{\dot{x}}_{a,\epsilon} \Delta \underline{\epsilon} + \underline{\dot{x}}_{a,x} \Delta \underline{x} + \underline{\dot{x}}_{a,T} \Delta T \quad (3.17)$$

Substituting Equations (3.7-3.10) and Equations (3.16-3.17) into Equation (3.11-3.14) and after rearranging terms leads to

$$\begin{bmatrix} \tilde{M} \end{bmatrix} \begin{bmatrix} \Delta\sigma \\ \Delta\epsilon^p \\ \Delta\chi \\ \Delta\epsilon \end{bmatrix} = \begin{bmatrix} \Delta V \\ \tilde{} \end{bmatrix} + \begin{bmatrix} \Delta V' \\ \tilde{} \end{bmatrix} \quad (3.18)$$

or

$$\begin{bmatrix} \Delta\sigma \\ \Delta\epsilon^p \\ \Delta\chi \\ \Delta\epsilon \end{bmatrix} = \begin{bmatrix} \tilde{M} \end{bmatrix}^{-1} \begin{bmatrix} \Delta V \\ \tilde{} \end{bmatrix} + \begin{bmatrix} \tilde{M} \end{bmatrix}^{-1} \begin{bmatrix} \Delta V' \\ \tilde{} \end{bmatrix} \quad (3.19)$$

isothermal terms nonisothermal terms

where

$$\tilde{M} = \begin{bmatrix} -\eta\Delta t \, a_{f,\tilde{g}} & \tilde{I} & -\eta\Delta t \, a_{f,\tilde{x}} & \tilde{0} \\ \tilde{0} & -a_{g,\tilde{\epsilon}^p} & \tilde{I} - \eta\Delta t \, a_{g,\tilde{x}} & \tilde{0} \\ \tilde{I} & \tilde{0} & \tilde{0} & -\tilde{0} \end{bmatrix} \quad (3.20)$$

$$\Delta V = \begin{bmatrix} \Delta t \{ a_{f,\tilde{}} - \eta (a_{\tilde{\epsilon}^p} - a_{f,\tilde{}}) \} \\ \Delta t \{ (a_{\tilde{x}} - a_{g,\tilde{\epsilon}^p} a_{\tilde{\epsilon}^p}) - \eta (a_{\tilde{x}} - a_{g,\tilde{}}) \} \\ \tilde{0} \end{bmatrix} \quad (3.21)$$

and

$$\Delta \underline{V} = \begin{bmatrix} \eta \Delta t \underline{a}_{f,T} \dot{T} \\ \eta \Delta t \underline{a}_{g,T} \dot{T} \\ \underline{\theta}(\alpha, D) \dot{T} \end{bmatrix} \quad (3.22)$$

It is important to note that Equations (3.19) are divided into isothermal and nonisothermal terms. The nonisothermal terms include the thermal load terms and the terms representing the temperature derivatives of the kinetic equation (\underline{f}) and the evolution equations of the hardening variable (\underline{g}). The temperature dependence of the material constants enters directly in the expression for $\underline{a}_{f,T}$ and $\underline{a}_{g,T}$. The approach outlined above was applied to the Bodner-Partom model and used in all the numerical calculations shown in this program.

For the Bodner-Partom model,

$$\underline{f} = \lambda S_{ij} \quad (3.23)$$

$$\underline{g}^I = \dot{Z}^I \quad (3.24)$$

$$\underline{g}^D = \dot{\beta}_{ij} \quad (3.25)$$

whose temperature derivative are as follow:

$$\underline{f}_{,T} = -\frac{1}{2} \left(\frac{Z^2}{3J_2} \right)^n \ln \left(\frac{Z^2}{3J_2} \right) \dot{\epsilon}_{ij}^p \left(\frac{dn}{dT} \right) \quad (3.26)$$

$$\begin{aligned}
g_{,T}^I &= 2m_1 \sqrt{D_2 J_2} \left(\frac{dZ_2}{dT} \right) - A_1 Z_1 \left[\frac{Z - Z_2}{Z_1} \right]^{r_1} \cdot \\
&\quad \left[\frac{1}{A_1} \frac{dA_1}{dT} + \ln \left[\frac{Z - Z_2}{Z_1} \right] \left(\frac{dr_1}{dT} \right) \right] \quad (3.27) \\
g_{,T}^D &= 2m_2 \sqrt{D_2 J_2} u_{ij} \left(\frac{dZ_3}{dT} \right) - A_2 Z_1 \left[\frac{\sqrt{\beta_{kl} \beta_{kl}}}{Z_1} \right]^{r_2} \frac{\beta_{ij}}{\sqrt{\beta_{kl} \beta_{kl}}} \cdot \\
&\quad \left\{ \frac{1}{A_2} \left(\frac{dA_2}{dT} \right) + \ln \left[\frac{\sqrt{\beta_{kl} \beta_{kl}}}{Z_1} \right] \left(\frac{dr_2}{dT} \right) \right\} \quad (3.28)
\end{aligned}$$

It is noted that this model contains relatively few temperature-dependent material constants (compared to other models) which simplifies the numerical work. From Equations (3.26-3.28) it is clear that the temperature derivatives of the material constants are needed in the nonisothermal load terms in Equations (3.19). The appropriate temperature derivatives of the Bodner-Partom model constants for B1900+Hf are obtained by fitting the temperature-dependent material constants, shown in Table 3.1, to appropriate functions and then taking derivatives of those functions with respect to temperature. Summaries of the expressions representing the temperature dependence of the model constants for B1900+Hf are given in Table 3.2.

3.3. Thermomechanical Constitutive Testing

3.3.1 Experimental Set-up

Thermomechanical response tests were conducted on an MTS hydraulic testing machine equipped with an inducting heating unit, a dynamic temperature

TABLE 3.1

BODNER-PARTOM MODEL CONSTANTS FOR B1900+HF

o Temperature-Independent Constants

$m_1 = .270 \text{ MPa}^{-1}$
 $m_2 = 1.52 \text{ MPa}^{-1}$
 $\alpha_1 = 0.0$
 $Z_1 = 3000 \text{ MPa}$
 $Z_3 = 1150 \text{ MPa}$
 $r_1 = r_2 = 2$
 $D_o = 1 \times 10^4 \text{ sec}^{-1}$

o Temperature-Dependent Constants

Constants	Temperature, °C		
	$T \leq 760^\circ\text{C}$	871°C	982°C
n	1.055	1.03	.850
$Z_o \text{ (MPa)}$	2700	2400	1900
$A_1 = A_2 \text{ (sec}^{-1}\text{)}$	0	.0055	.02
$Z_2 (=Z_o) \text{ (MPa)}$	2700	2400	1900
			1200

o Elastic Moduli for B1900+HF

$E = 1.987 \times 10^5 + 16.78 T - .1034 T^2 + 1.143 \times 10^{-5} T^3 \text{ MPa with } T \text{ in } ^\circ\text{C}.$

$G = 8.650 \times 10^4 - 17.58 T + 2.321 \times 10^{-2} T^2 - 3.464 \times 10^{-5} T^3 \text{ MPa with } T \text{ in } ^\circ\text{C}.$

TABLE 3.2
TEMPERATURE DEPENDENCE OF THE BODNER-PARTOM MODEL
CONSTANTS FOR B1900+Hf

$$n = 1.055 \quad T \leq 863.4^{\circ}\text{C}$$

$$n = -1.0524 + \frac{2.394.74}{T} \quad 863.4^{\circ}\text{C} \leq T \leq 1093^{\circ}\text{C}$$

$$Z_0 = Z_2 = 2700 \text{ MPa} \quad T \leq 838^{\circ}\text{C}$$

$$Z_0 = Z_2 = -4950 + \frac{8.5 \times 10^6}{(T+273)} \text{ MPa} \quad 838^{\circ}\text{C} \leq T \leq 1093^{\circ}\text{C}$$

$$A_1 = A_2 = 1.319 \times 10^9 \exp \left[- \frac{30580}{(T+273)} \right] \text{ sec}^{-1} \quad T \leq 1093^{\circ}\text{C}$$

monitoring system, a thermal strain compensator, and a cooling system for the test specimen. A schematic of the TMF testing system is illustrated in Figure 3.1. The specimens could be subjected to controlled axial extension or compression at a prescribed temperature-time history. The dynamic temperature monitoring system, which consists of a number of thermocouples and isolation amplifiers, was constructed at SwRI and was used both for temperature control and for measuring the temperature profile along the gauge length of the test specimen. The thermal strain compensator, also built at SwRI, is an electronic circuit device which reproduces the thermal strain of the test specimen at a given temperature. As indicated in Figure 3.1, the input to the thermal strain compensator is temperature (from the temperature controller), and the output is a voltage signal corresponding to the thermal strain of the test specimen at that temperature. In a TMF test, the thermal strain signal is added to the prescribed mechanical strain signal in the MTS machine controller.

The thermomechanical test specimens were of tubular geometry, as shown in Figure 3.2(c), and were heated by induction heating and cooled both externally and internally by forced cold air (at RT). Internal cooling was accomplished by flowing room temperature air through the center of the tubular specimens and the grip system. The forced cold air flow was regulated with solenoid-operated flow distribution manifolds. The performance of the TMF testing system was evaluated by cycling from 538 to 982°C. Figure 3.3 shows good agreement between the prescribed temperature setting and the temperature on the specimen measured by the thermocouple located at the center of the specimen. The temperature distribution along the gauge length of the specimen was within 20°C of the prescribed temperature. This temperature gradient was

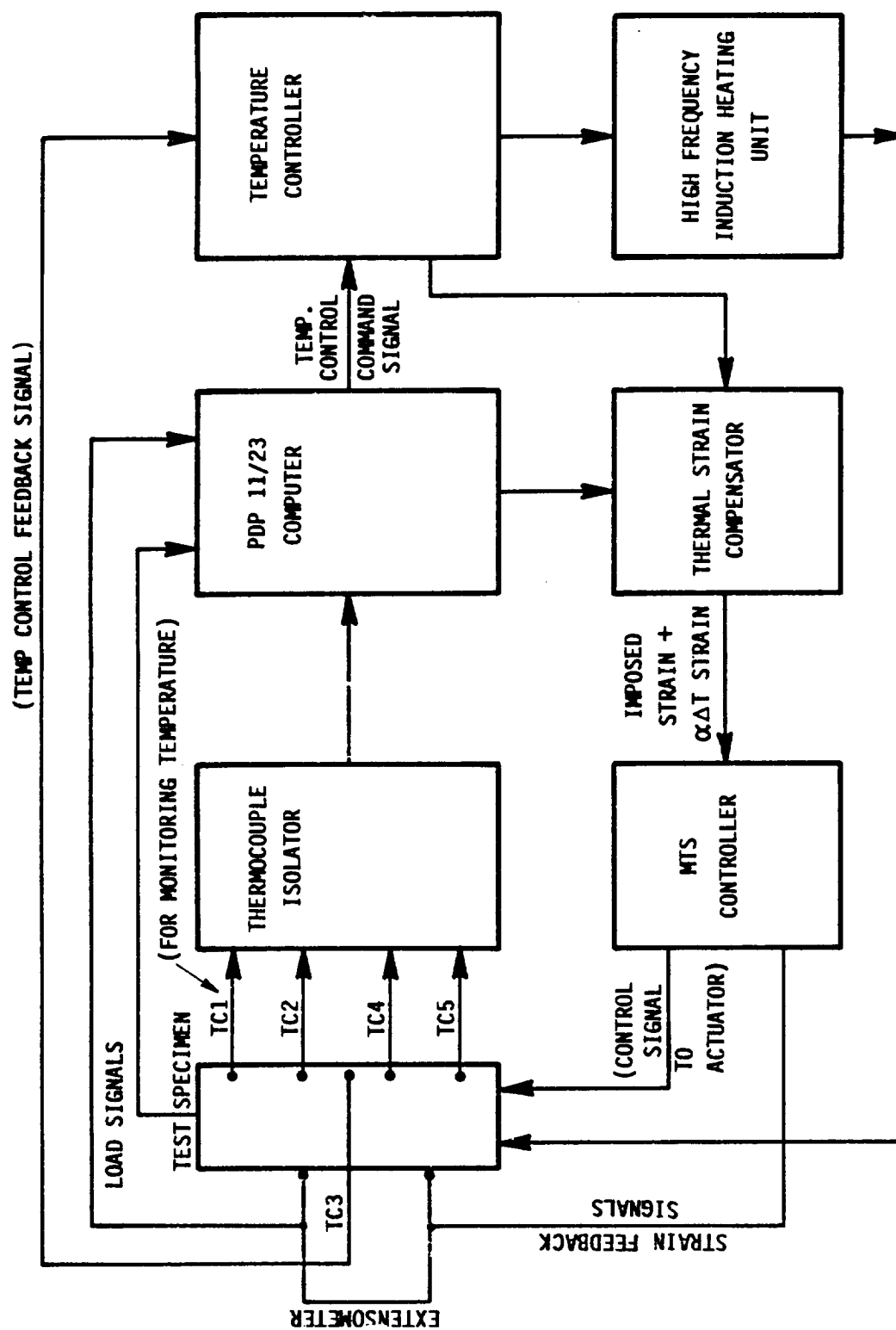


FIGURE 3.1 A SCHEMATIC OF THE THERMOMECHANICAL TESTING SYSTEM

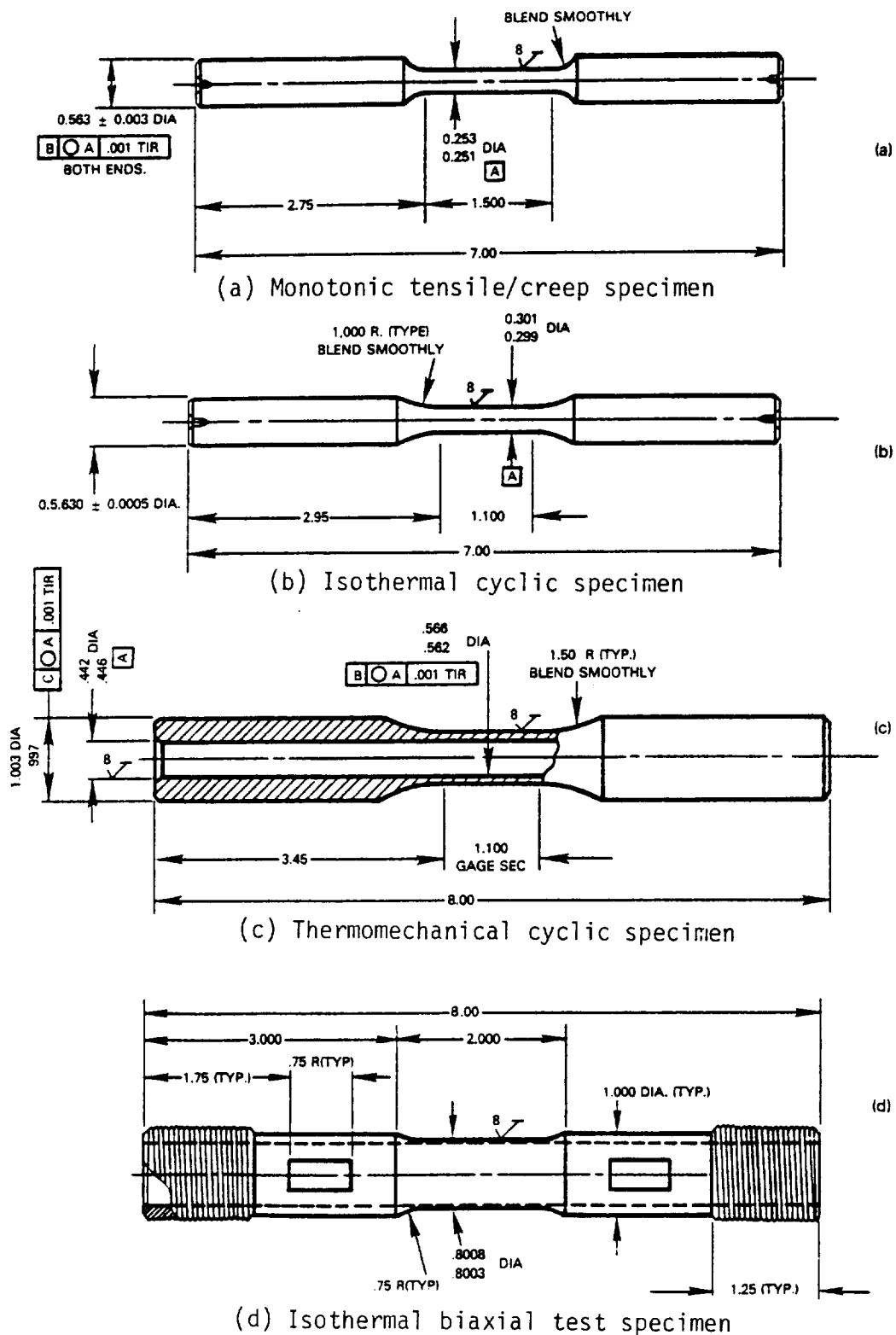


FIGURE 3.2 SPECIMEN DESIGNS UTILIZED IN VARIOUS CONSTITUTIVE TESTS
(All units are in inches.)

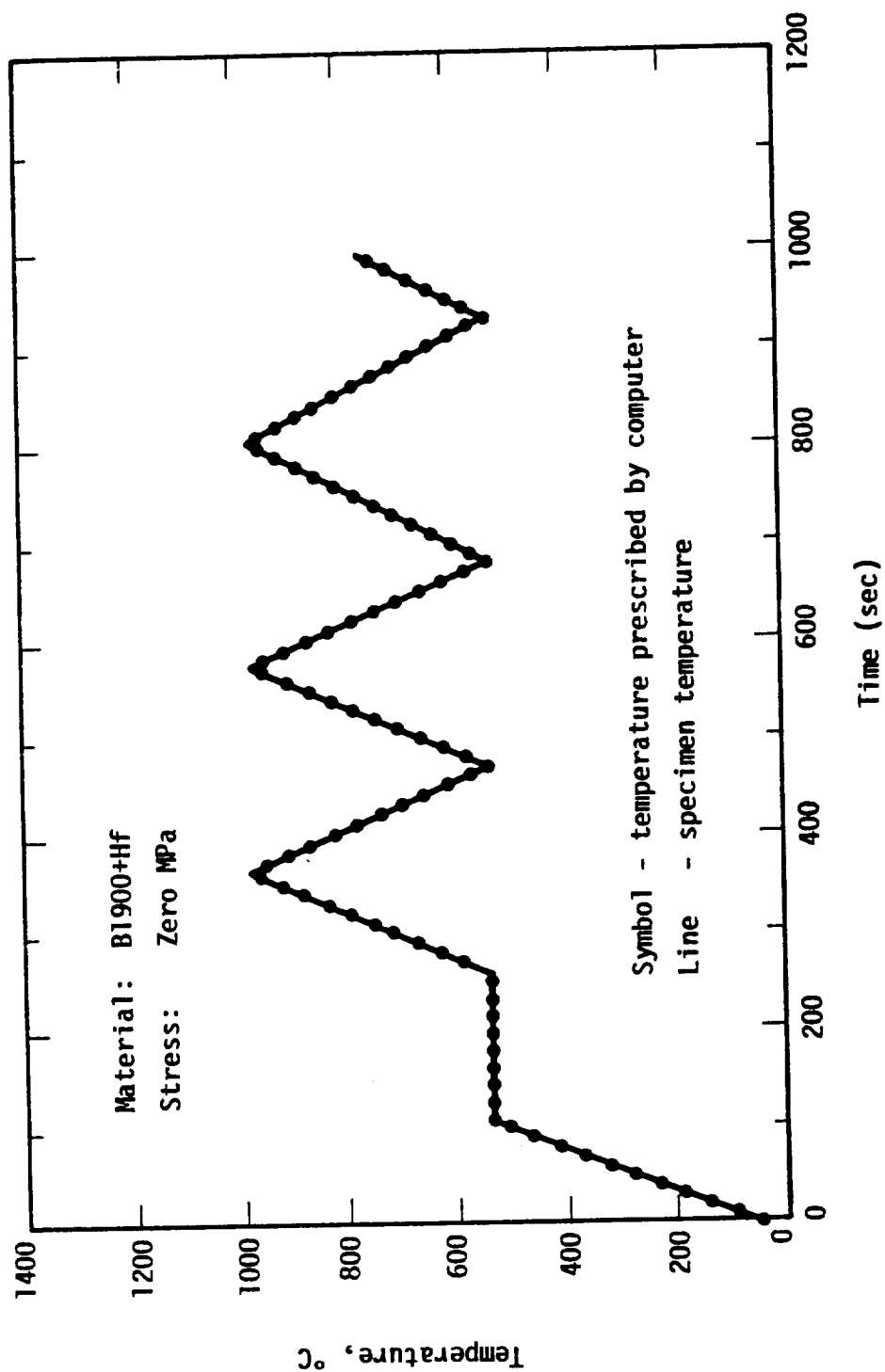


FIGURE 3.3 COMPARISON OF PRESCRIBED TEMPERATURE WITH SPECIMEN (MEASURED) TEMPERATURE

less than 9°C during heating but a 20°C gradient occurred along the axial direction of the gauge length of the specimen during cooling. The lower part of the specimen was persistently hotter than the prescribed temperature because of the direction of internal cooling air flow.

For calibrating the thermal strain compensator, the thermal strain values of B1900+Hf and Mar-M247 were measured by heating the specimens, at zero load, from 38°C to 982°C and then cycling between 538°C to 982°C for ten cycles. Figure 3.4 shows that the thermal strain of B1900+Hf is a nonlinear function of temperature. Consistent thermal strains were obtained during thermal cycling indicating good reproducibility. The thermal strain data of Mar-M247 are identical to those of B1900+Hf. After calibration, the thermal strain compensator was evaluated by performing TMF strain cycling using the thermal strain compensator as the control input. Such a thermomechanical strain cycle should ideally lead to zero stress on the specimen. The maximum thermal stress observed on specimens under these check tests was less than 14 MPa.

Figure 3.5 shows a close-up view of a TMF specimen under test during TMF cycling at temperatures between 538 to 982°C. In addition to the induction coils, Figure 3.5 shows the small copper tubings used for external cooling and the externally mounted extensometer which is attached to the specimen through ceramic reach-rods. The reach-rods are placed on two small indents which are 25.4 mm apart and within the gauge length of the specimen.

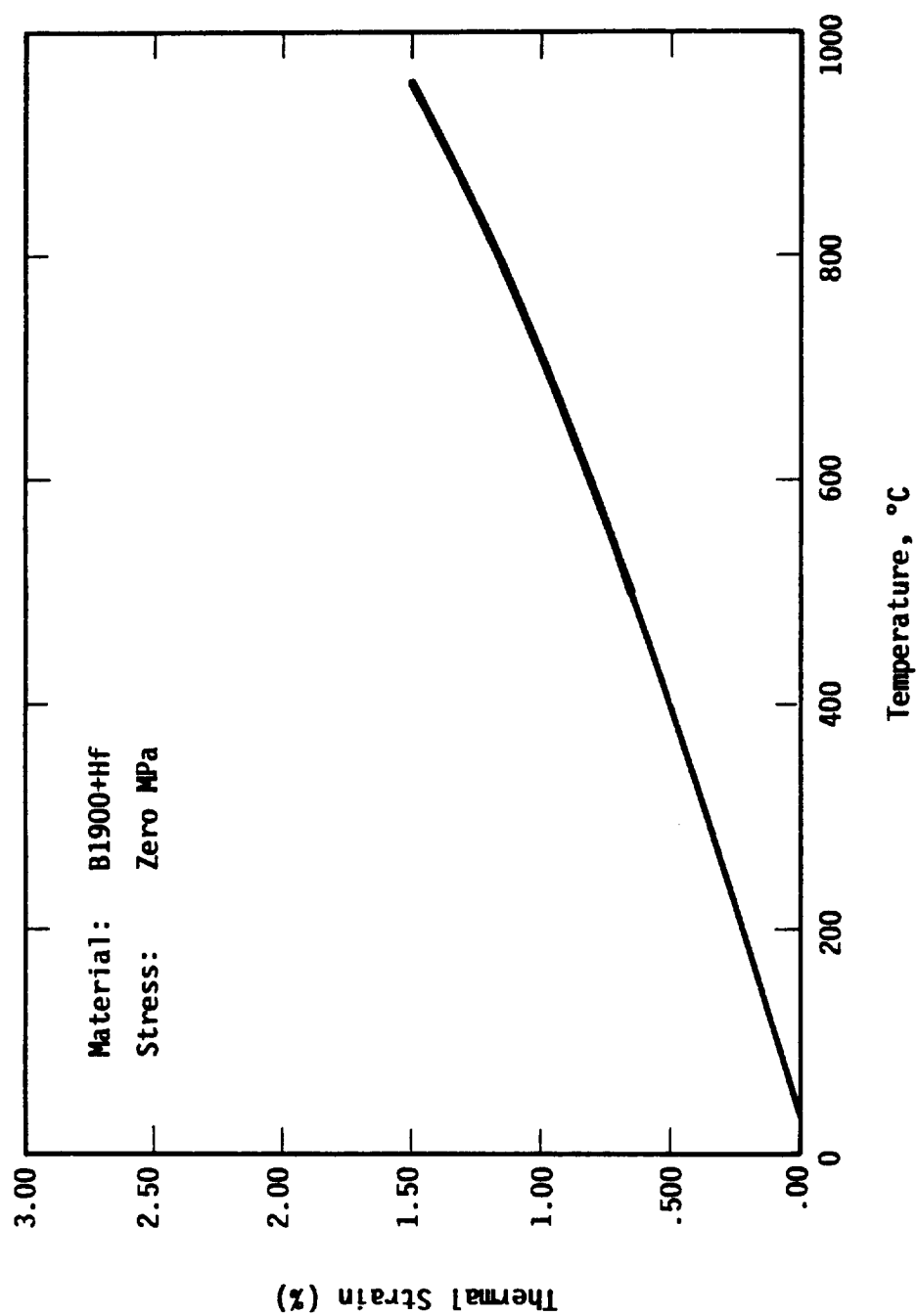


FIGURE 3.4 THERMAL STRAIN OF B1900+Hf SPECIMEN HEATED FROM 38°C TO 538°C AND THEN CYCLED AT ZERO LOAD FROM 538°C TO 982°C FOR TEN CYCLES

ORIGINAL PAGE IS
OF POOR QUALITY



FIGURE 3.5 A CLOSE-UP VIEW OF A THERMOMECHANICAL CYCLIC SPECIMEN UNDER CYCLING FROM 538°C TO 982°C. The specimen is heated by induction heating and cooled by feeding cold (RT) air internally through the tubular specimen and externally using small copper tubes.

3.3.2 Non-isothermal Loading Paths

A number of experiments involving various thermomechanical loading paths were used to test the unified constitutive approach. The test matrix, shown in Table 3.3, consisted of simple as well as complicated paths of strain and temperature. Four types of nonisothermal tests were performed: (1) step temperature tensile tests; (2) step temperature creep tests; (3) step temperature cyclic tests; (4) thermomechanical fatigue (TMF) tests. The strain-time and thermal history for these tests are schematically illustrated in Figures 3.6-3.9.

As shown in Table 3.3, six-step temperature tensile tests were performed. In these tests, the specimens were pulled at a constant strain rate up to a strain level of 1-2% at an initial temperature T_1 . With continued straining, the test temperature was then changed at a prescribed heating or cooling rate until it reached T_2 . After an additional 0.5% strain at T_2 , the test temperature was changed again to T_3 in a similar manner. In some cases the specimen failed after only one temperature change.

In the step temperature creep experiments, the specimens were first subjected to a constant stress σ_1 at temperature T_1 until a steady creep rate was reached. The test temperature and the imposed stress were then changed to T_2 and σ_2 , respectively. After a steady state creep rate was attained, the test conditions reverted back to σ_1 and T_1 if the specimen was still intact.

Six step temperature cyclic tests were performed. As indicated in Table 3.3, two of the test specimens were subjected to fully reversed strain cycling with a strain range of $\pm 0.4\%$ at T_1 . After cyclic saturation, the temperature was raised to T_2 and held at the peak strain for two hours. The test temperature was then lowered to T_1 , and the specimen was cycled again at

TABLE 3.3
TEST MATRIX FOR THERMOMECHANICAL CONSTITUTIVE TESTING
OF B1900+Hf

(1.) Step Temperature Tensile Tests:

Specimen	Test #	$\dot{\epsilon}$, sec ⁻¹	T_1 , °C	T_2 , °C	T_3 , °C	\dot{T} , °C/sec
K9	1	1×10^{-4}	538	760	538	4.4
K2	2	1×10^{-4}	760	982	760	4.4
K1	3	1×10^{-4}	982	760	982	4.4
K5	4	1×10^{-4}	760	982	760	4.4
K4	5	4×10^{-6}	760	982	760	0.44
K3,K11	6	1×10^{-4}	760	538		4.4
1A	6A	1×10^{-4}	871	649		4.4

(2.) Step Temperature Creep Tests:

Specimen	Test #	σ_1 , MPa	T_1 , °C	σ_2 , MPa	T_2 , °C	\dot{T} , °C/sec
K8	7	690	649	427	871	4.4
K6	8	690	760	215	982	4.4
K7	9	215	982	690	760	-4.4

(3.) Step Temperature Cyclic Tests:

Specimen	Test #	$\Delta\epsilon_1$, %	T_1 , °C	$\Delta\epsilon_2$	T_2 , °C	$R\left(\frac{\epsilon_{\min}}{\epsilon_{\max}}\right)$	\dot{T} , °C/sec
K17	10	± 0.4	538	hold at peak strain	760	-1	4.4
K16	11	± 0.4	538	hold at peak strain	982	-1	4.4
K12	12	± 0.4	538	± 0.4	982	-1	4.4
	13	± 0.4	760	± 0.4	538	-1	4.4
K13	14	± 0.4	982	± 0.4	538	-1	-4.4

TABLE 3.3 (CONTINUED)
TEST MATRIX FOR THERMOMECHANICAL CONSTITUTIVE TESTING
OF B1900+Hf

(4.) Thermomechanical Cyclic Tests:

<u>Specimen</u>	<u>Test #</u>	<u>T, °C/sec</u>	<u>T Range, °C</u>	<u>$\dot{\epsilon}$, sec⁻¹</u>	<u>$\Delta\epsilon$, %</u>	<u>Loading Mode</u>
1B	15	2.8	538-760	1×10^{-4}	$\pm .4$	in-phase
		1.85	538-760	1×10^{-4}	$\pm .6$	in-phase
1D	16	2.8	538-760	1×10^{-4}	$\pm .4$	out-of-phase
		1.85	538-760	1×10^{-4}	$\pm .6$	out-of-phase
1E	17	5.6	538-982	1×10^{-4}	$\pm .4$	out-of-phase
		3.7	538-982	1×10^{-4}	$\pm .6$	out-of-phase
1C	18 (Coated Specimens)	5.6	538-982	1×10^{-4}	$\pm .4$	out-of-phase
		3.7	538-982	1×10^{-4}	$\pm .6$	out-of-phase

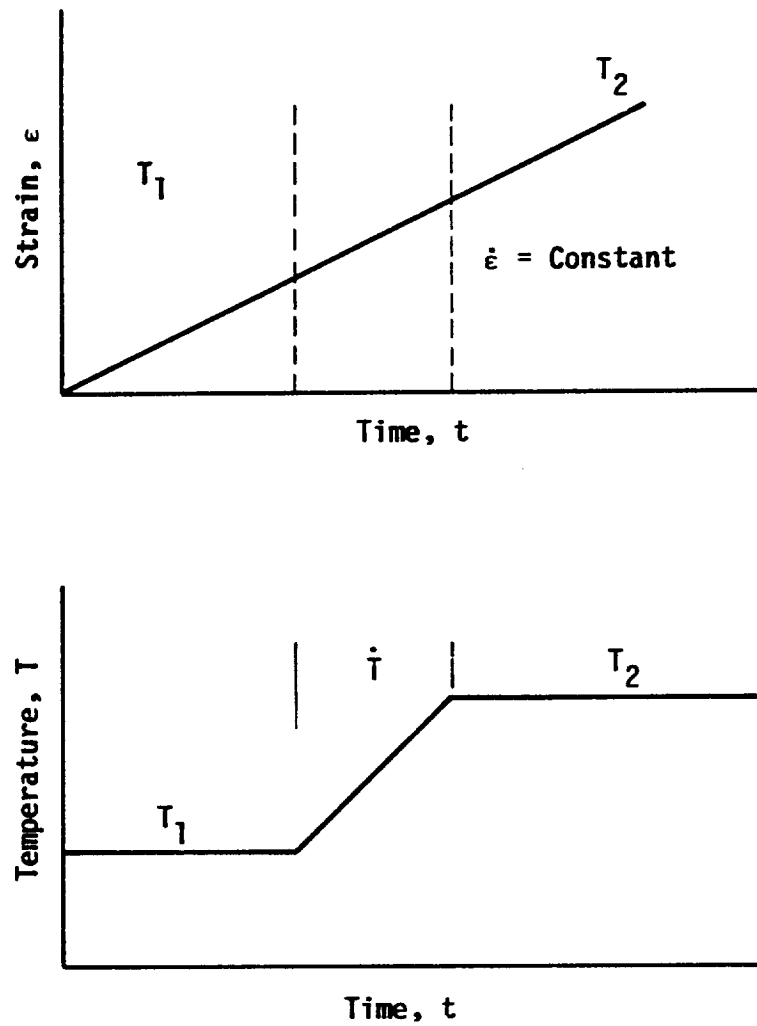


FIGURE 3.6 STRAIN-TIME AND TEMPERATURE-TIME HISTORIES FOR STEP TEMPERATURE TENSILE TESTS. In some cases, more than one temperature change is planned.

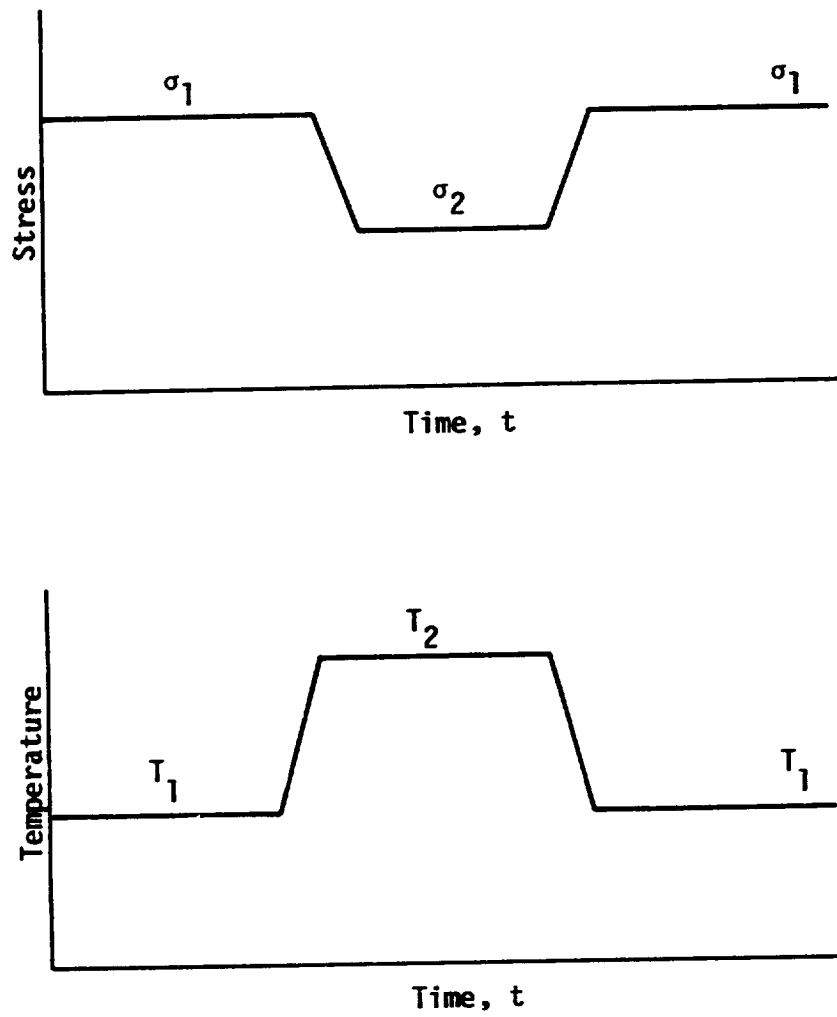


FIGURE 3.7 STRESS-TIME AND TEMPERATURE-TIME HISTORIES FOR STEP TEMPERATURE CREEP TESTS

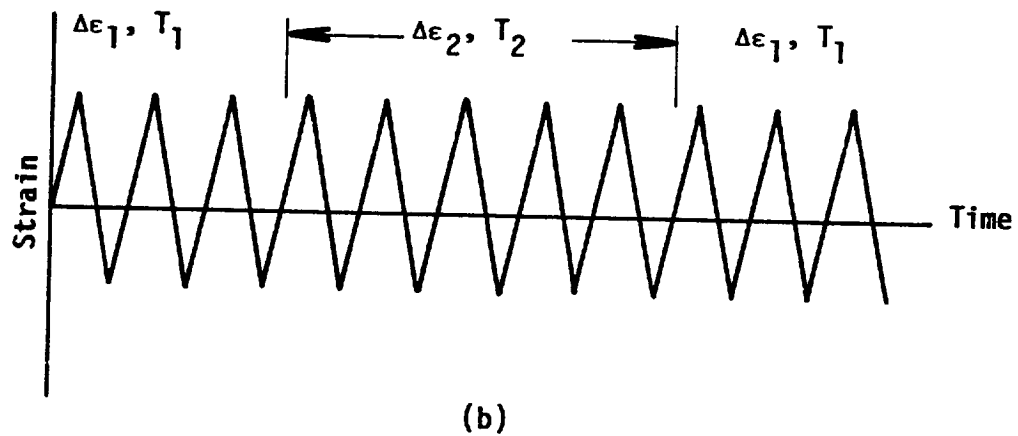
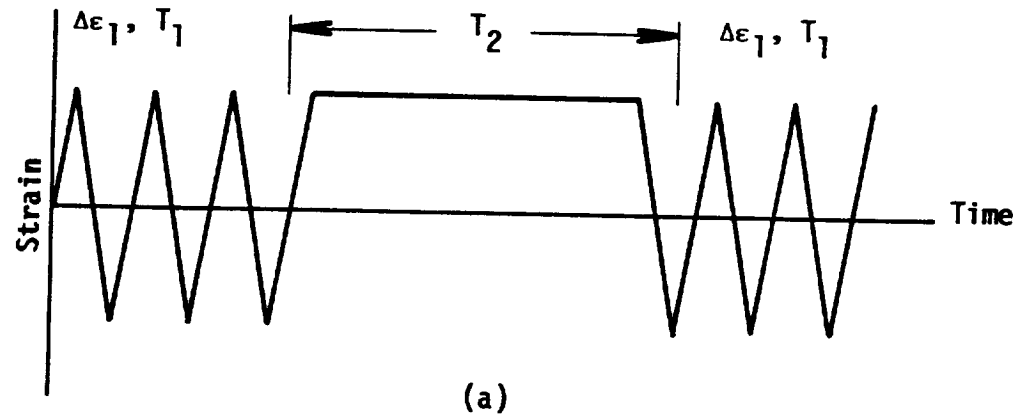


FIGURE 3.8 STRAIN-TIME HISTORIES FOR STEP TEMPERATURE CYCLIC TESTS. (a) Strain hold after temperature change from T_1 to T_2 , and (b) strain cycling after temperature change from T_1 to T_2 .

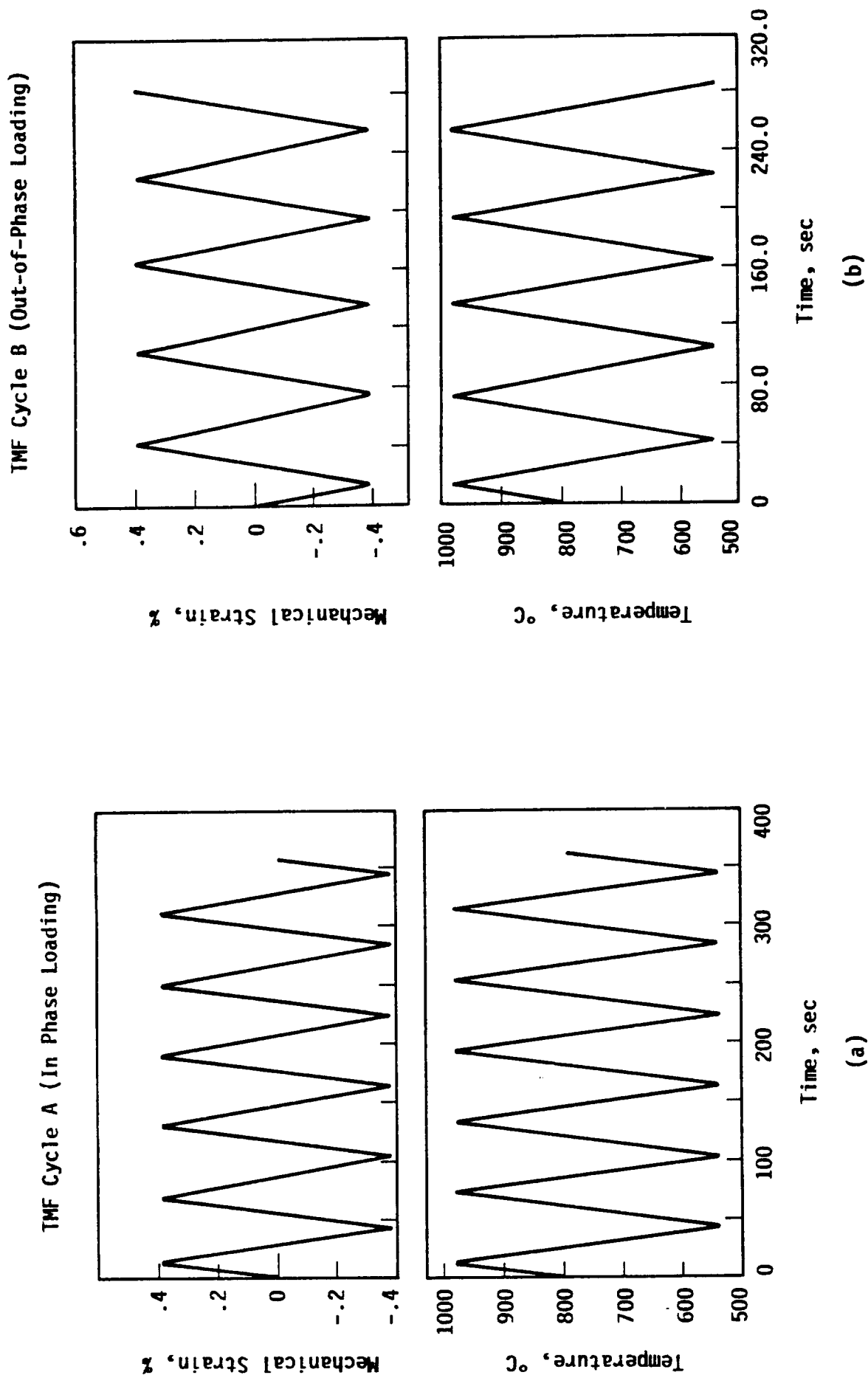


FIGURE 3.9 TMF LOADING HISTORIES OF TRIANGULAR WAVEFORM: (a) IN-PHASE LOADING, (b) OUT-OF-PHASE LOADING

$\pm 0.4\%$ strain until cyclic saturation was again obtained. In the other four cyclic tests, the specimens were cycled initially at $\pm 0.4\%$ strain at T_1 until cyclic saturation. The temperature was then changed to T_2 while cycling at $\pm 0.4\%$ strain continued. After cyclic saturation at T_2 occurred, the test temperature reverted back to T_1 with continued cycling.

Four thermomechanical fatigue tests were performed using transgranular waveforms with the imposed temperature and strain being either in-phase [Figure 3.9(a)] or out-of-phase [Figure 3.9(b)]. In the former case, the temperature and strain imposed on the specimen increased and decreased linearly with time in similar manner reaching their respective maxima and minima at the same time. For the out-of-phase tests, temperature and strain varied linearly with time in opposite directions, e.g., a temperature increase was coupled to an imposed strain decrease (compression). The strain maxima occurred at the minimum temperature, while the maximum temperature occurred at the minimum strain. Both an in-phase and an out-of-phase cycle were performed for TMF cycling between 538 to 760°C. Only the out-of-phase cycle was performed for TMF cycling between 538 to 982°C. For examining coating effects, this out-of-phase cycle was also applied to the B1900+Hf specimen coated with yttrium-stabilized zirconia. All the four TMF tests were performed for strain ranges of $\pm 0.4\%$ and $\pm 0.6\%$ at a strain rate of $1 \times 10^{-4} \text{ sec}^{-1}$.

3.4 Results: Experiment and Model

3.4.1 Nonisothermal Tensile Tests

Figure 3.10 shows the nonisothermal (step temperature) tensile tests conducted in the 760-982°C temperature range where thermal recovery is

important but without the possible complications of strain aging. The imposed strain rate was $1 \times 10^{-4} \text{ sec}^{-1}$ and the heating or cooling rate was 4.4°C/sec . In one of the tests, the specimen (K3) was pulled isothermally at 760°C to 2% strain. In a second test, the specimen (K1) was pulled at 982°C to a strain of 1%, and the temperature was then decreased at 4.4°C/sec to 760°C . The temperature reached 760°C at a strain of 1.5%, and the specimen was then pulled isothermally at 760°C . The results in Figure 3.10 show that the nonisothermal specimen (K1) exhibited similar stress-strain behavior at 760°C and appears to reach approximately the same value of saturation stress as the isothermally tested specimen (K3) indicating little thermal history effect. In a third test (Specimen K2), the test temperature was initially at 760°C and was then increased to 980°C after 1% strain. In this case, the stress-strain behavior of the nonisothermal specimen (K2) at 982°C was also consistent with that extrapolated from the isothermal curve for 982°C (K1); i.e., the same value of stress at steady-state conditions. These results indicate that the steady-state tensile deformation behavior of B1900+Hf in the range of 760 - 982°C depends on the current test temperature but not on the thermal history.

Before a comparison of model and experiment is presented for the results shown in Figure 3.10, it is instructive to compare these nonisothermal test data, which are based on tubular specimens, with previously obtained isothermal data of round-bar specimens. Such a comparison, shown in Figure 3.11, reveals that the tubular specimens used for the nonisothermal tests are somewhat weaker at 982°C but stronger at 760°C than the round-bar specimens. Figure 3.12 shows the nonisothermal stress-strain curves predicted by the Bodner-Partom model using material constants based on isothermal test data (round-bar specimens). Qualitatively, there is good agreement between theory

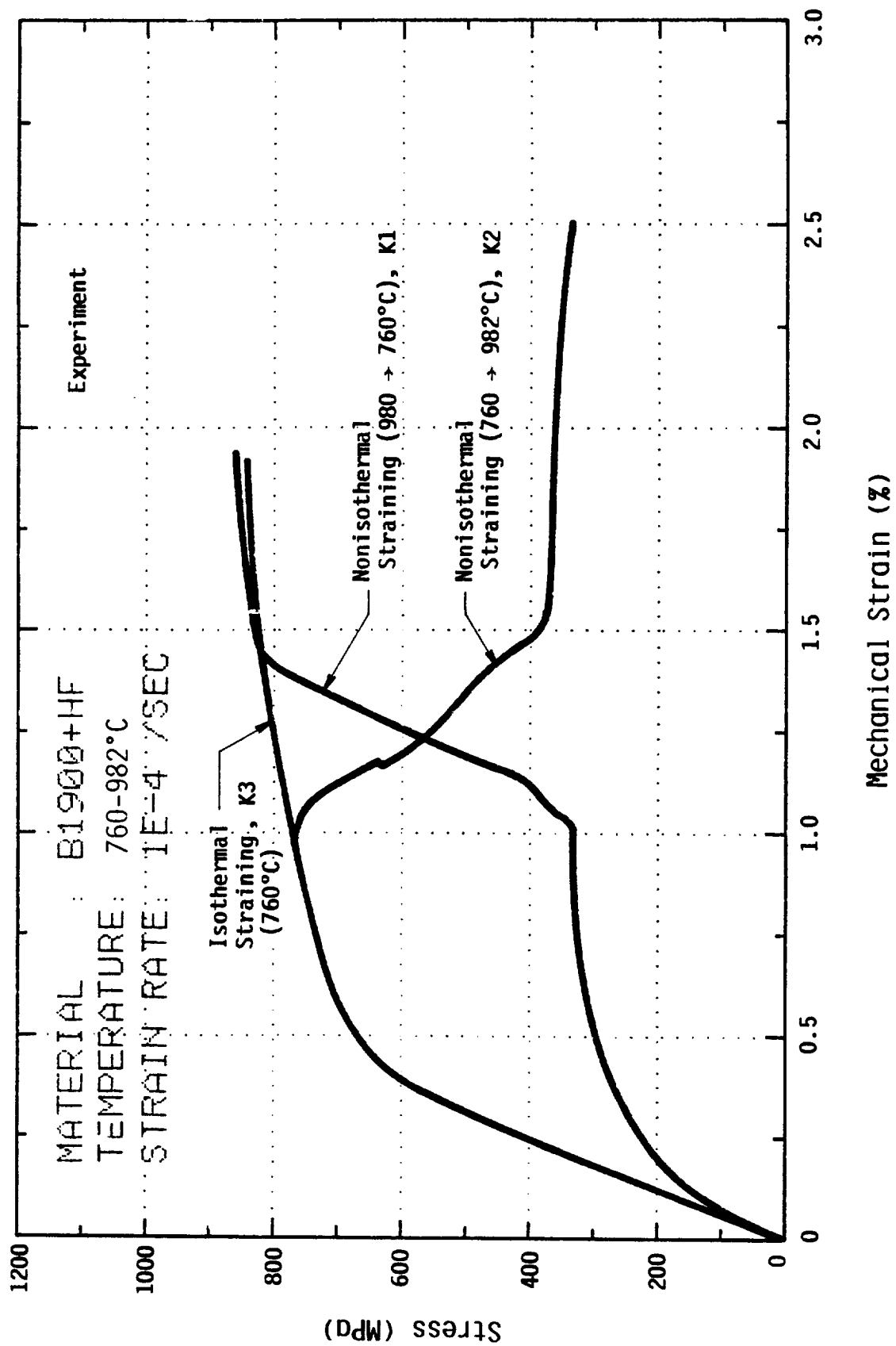


FIGURE 3.10. NONISOTHERMAL TENSILE RESULTS COMPARED WITH ISOTHERMAL TENSILE DATA AT 760°C

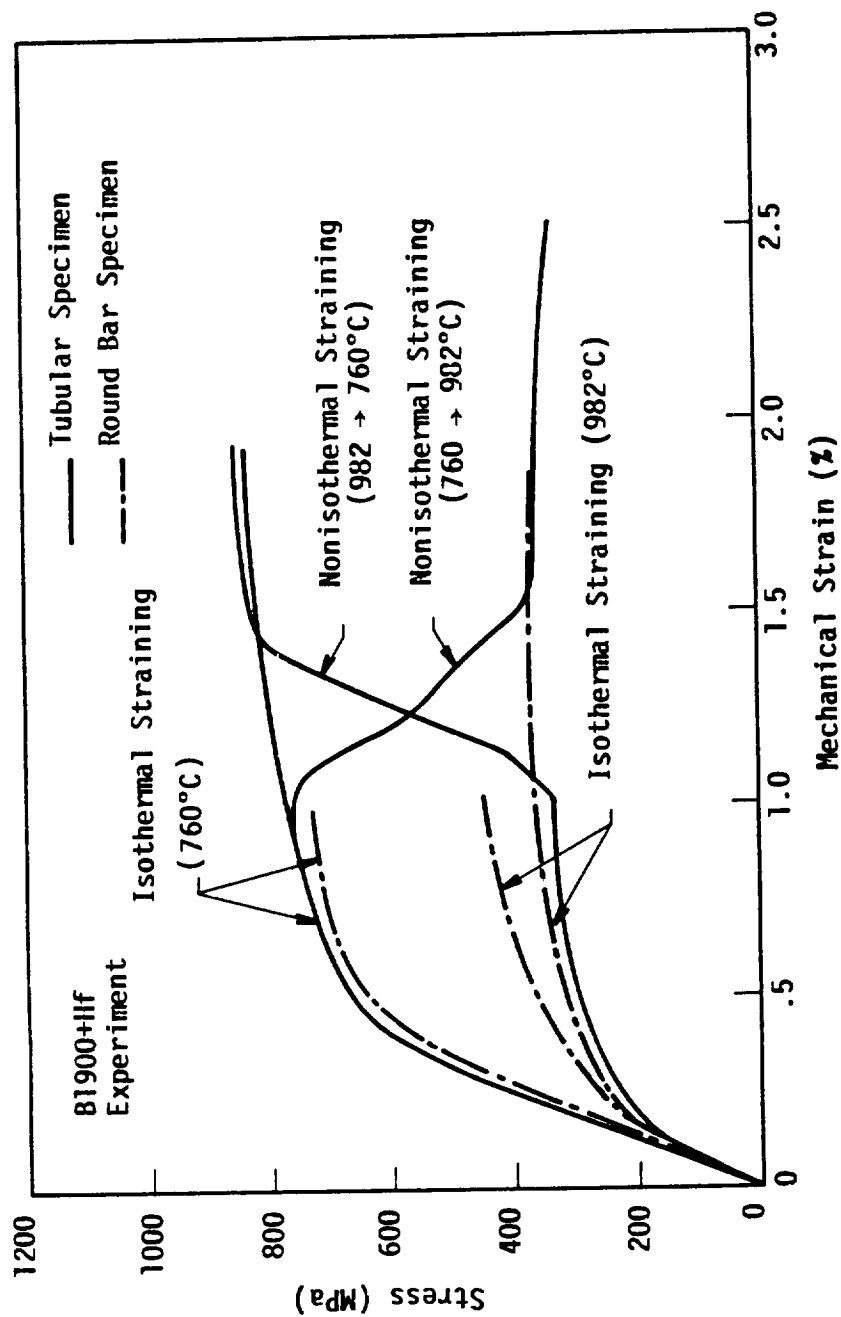


FIGURE 3.11 COMPARISON OF NONISOTHERMAL TENSILE RESULTS WITH ISOTHERMAL TENSILE DATA OBTAINED BASED ON ROUND-BAR SPECIMENS FROM BOTH THE BASE AND OPTIONAL PROGRAMS

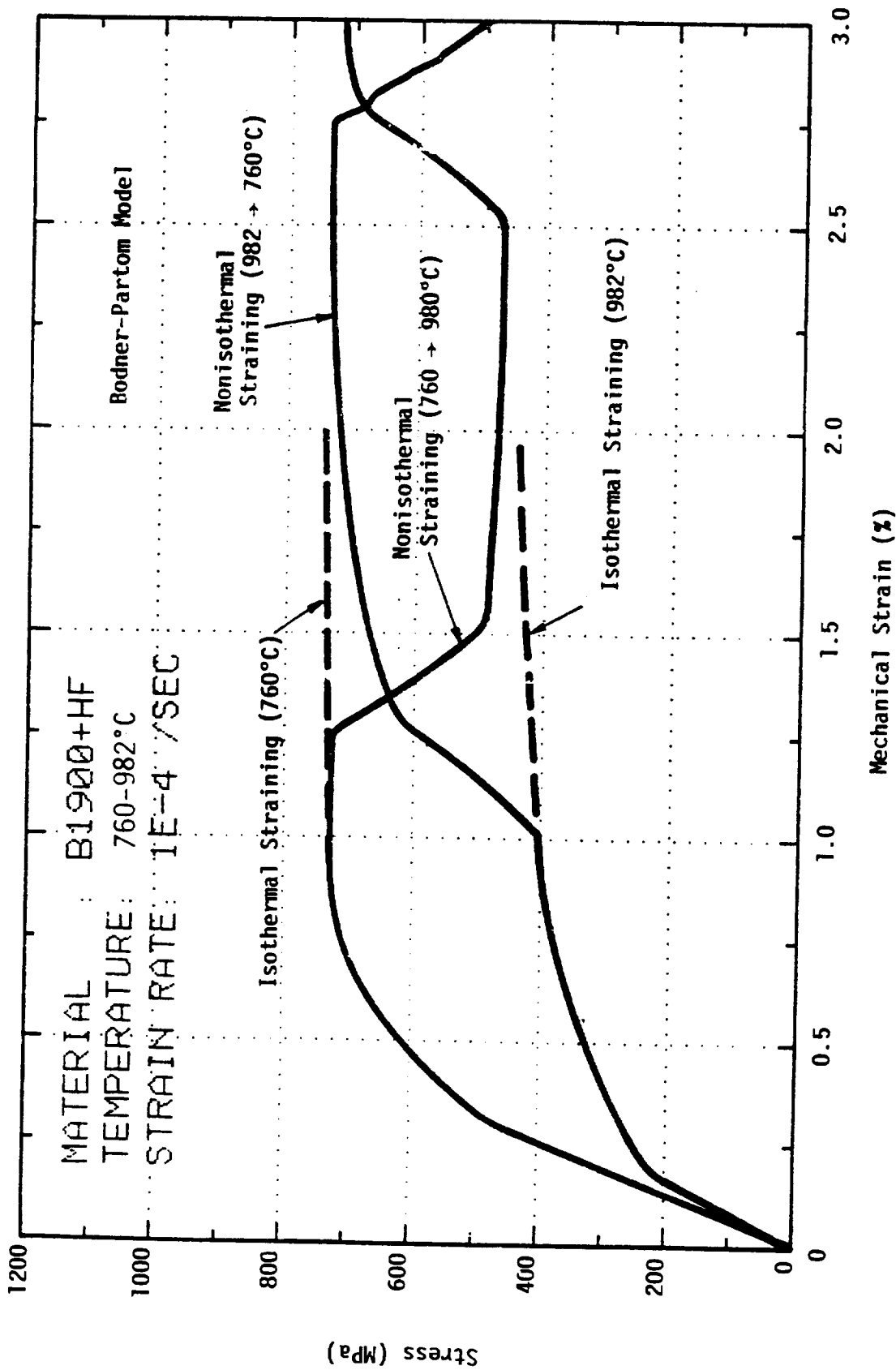


FIGURE 3.12 BODNER-PARTOM MODEL PREDICTIONS OF NONISOTHERMAL TENSILE CURVES COMPARED TO ISOTHERMAL TENSILE CURVES

and experiment, as both the experimental and the predicted results indicate that absence of a thermal history effect on the steady-state or saturation stress at a given imposed strain rate. Quantitative comparisons of theory and experiment in Figures 3.13 and 3.14 indicate that the Bodner-Partom model overpredicts the stress at 982°C, underpredicts that at 760°C. The discrepancies appear because the model constants were determined from the isothermal baseline data which are slightly different than that of the tubular specimens used in the nonisothermal tensile experiments tested under the same conditions.

Nonisothermal tensile tests were also conducted in the 538 to 760°C temperature range where strain aging effects could possibly occur [23]. In these tests, the specimens were strained at a constant rate of 10^{-4} sec^{-1} at an initial temperature T_1 to a strain of $\approx 2\%$. The test temperature was then changed to T_2 at a heating (or cooling) rate of 4.4°C/sec while constant straining continued. In all cases, the specimen temperature stabilized at T_2 at $\epsilon \geq 2.5\%$. Figure 3.15 shows the nonisothermal tensile test results for B1900+Hf for the two cases: (1) straining initially at 538°C with the temperature subsequently raised to 760°C (Specimen K9), and (2) straining initially at 760°C with the temperature reduced to 538°C (Specimen K3 and K11). The results in Figure 3.15 indicate that the nonisothermal, plastic flow behavior of B1900+Hf at 760°C (Specimen K9) is in agreement with that extrapolated from the isothermal data (Specimen K3 and K11). This behavior suggests that there is no thermal history effect on plastic flow, and it is consistent with the nonisothermal tensile data obtained in the temperature range of 760 to 982°C. On the other hand, the plastic flow behavior of B1900+Hf at 538°C appears to depend, in part, on thermal history since different values of the

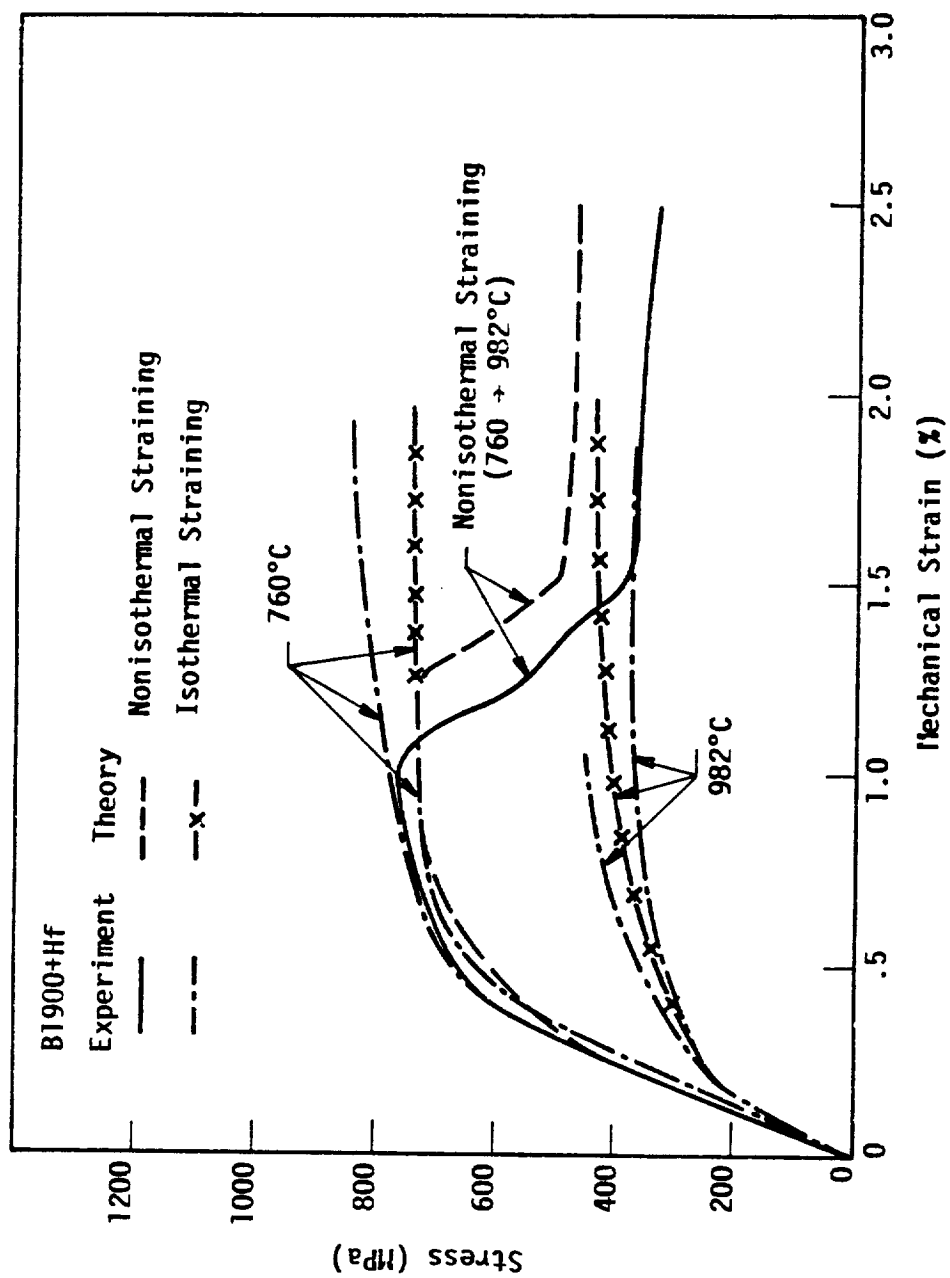


FIGURE 3.13 COMPARISON OF PREDICTED AND EXPERIMENTAL NONISOTHERMAL TENSILE CURVES FOR STRAINING AT $\dot{\epsilon} = 1 \times 10^{-4}$ SEC $^{-1}$ WITH TEMPERATURE CHANGE FROM 760°C TO 982°C WITH ISOTHERMAL DATA

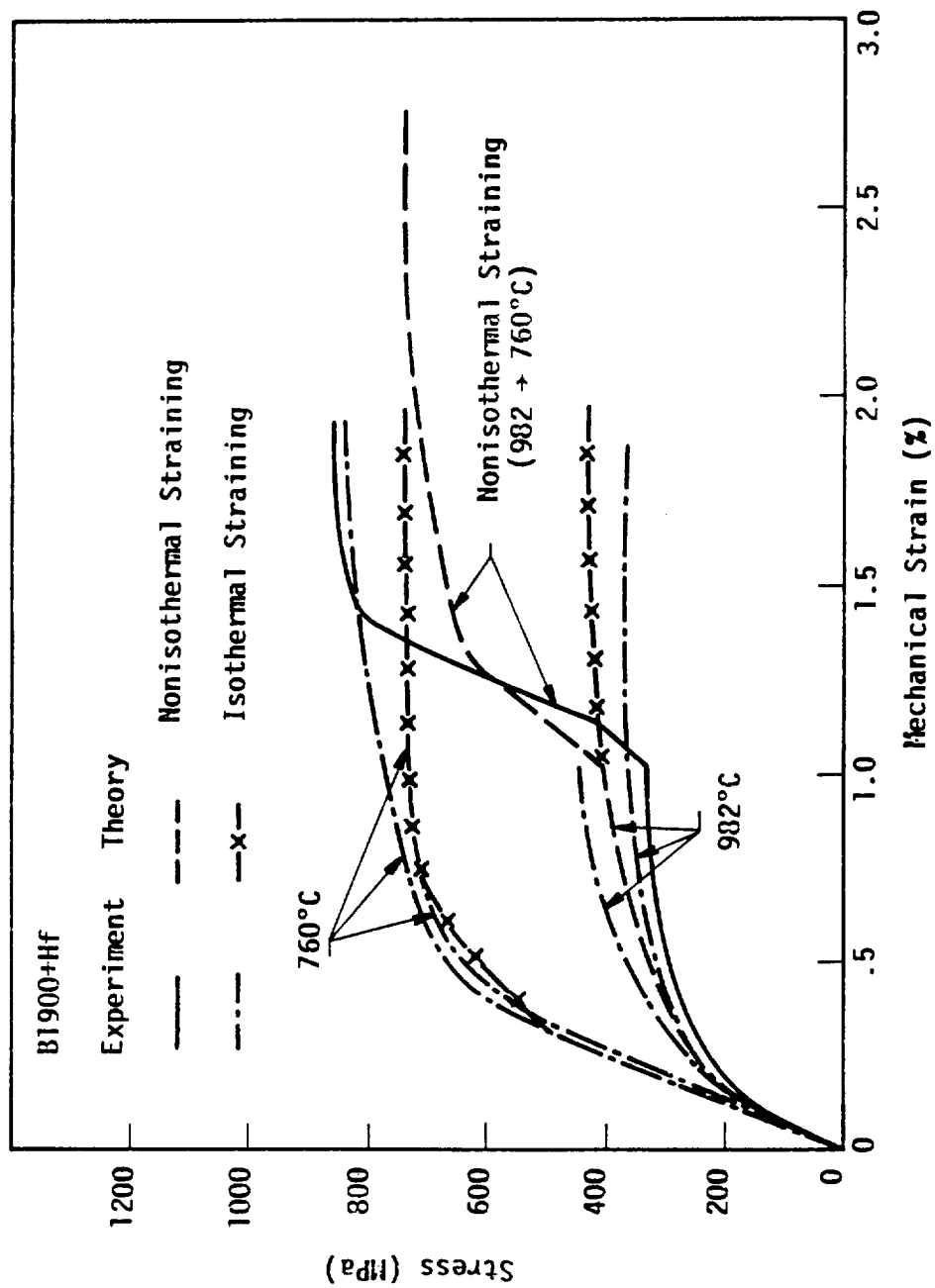


FIGURE 3.14 COMPARISON OF PREDICTED AND EXPERIMENTAL NONISOTHERMAL TENSILE CURVES FOR STRAINING AT $\dot{\epsilon} = 1 \times 10^{-4}$ SEC $^{-1}$ WITH TEMPERATURE CHANGE FROM 982°C TO 760°C WITH ISOTHERMAL DATA

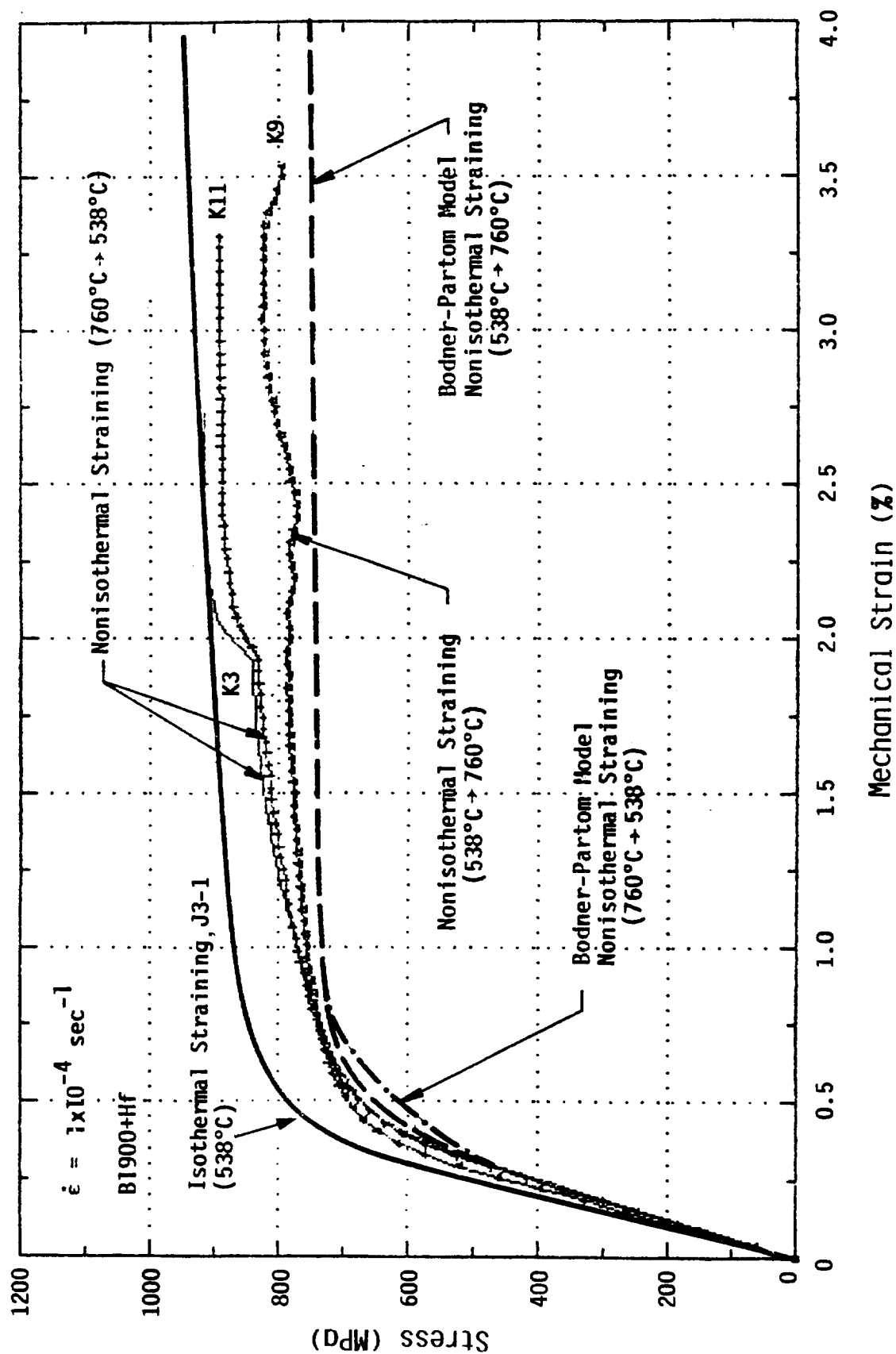


FIGURE 3.15. COMPARISON OF NONISOTHERMAL TENSILE RESULTS WITH MODEL PREDICTIONS FOR SPECIMENS TESTED IN THE 538-760°C TEMPERATURE RANGE

saturation stress were obtained under isothermal and nonisothermal straining conditions.

To further clarify the deformation behavior of B1900+Hf in the temperature range of 538–760°C, an isothermal tensile test was performed at 538°C under a strain rate of $1 \times 10^{-4} \text{ sec}^{-1}$ (Specimen J3-1). Figure 3.15 shows that a large variation in the stress-strain behavior of B1900+Hf is observed between Specimen J3-1 and K9 at 538°C. The response curve for Specimen J3-1 is in reasonable agreement with those of Specimens K3 and K11 for the portions at which $T = 538^\circ\text{C}$. From Figure 3.15, it is clear that there is a large scatter in the isothermal data for B1900+Hf at 538°C. It is therefore not possible to conclude from these tests whether there is a thermal history effect associated with plastic straining of B1900+Hf in the "strain aging" regime (538–760°C). This question will be raised again in relation to the nonisothermal cyclic tests.

3.4.2 Nonisothermal Creep Tests

The effects of thermal history on the steady-state creep behavior of B1900+Hf were investigated by performing step-temperature creep tests. In these tests, the specimens were subjected to a series of load and temperature histories designed to demonstrate whether or not the steady-state creep rate at a given stress and temperature depends on thermal history. Figure 3.16 shows the nonisothermal creep results obtained by applying an initial stress of 215 MPa at 982°C (to Specimen K7) until a steady-state creep condition is reached ($\dot{\epsilon} = 1.3 \times 10^{-6} \text{ sec}^{-1}$). The temperature and the imposed stress were then changed to 760°C and 690 MPa, respectively, for which the steady-state creep rate became $7.5 \times 10^{-7} \text{ sec}^{-1}$. Subsequently, the stress was changed back

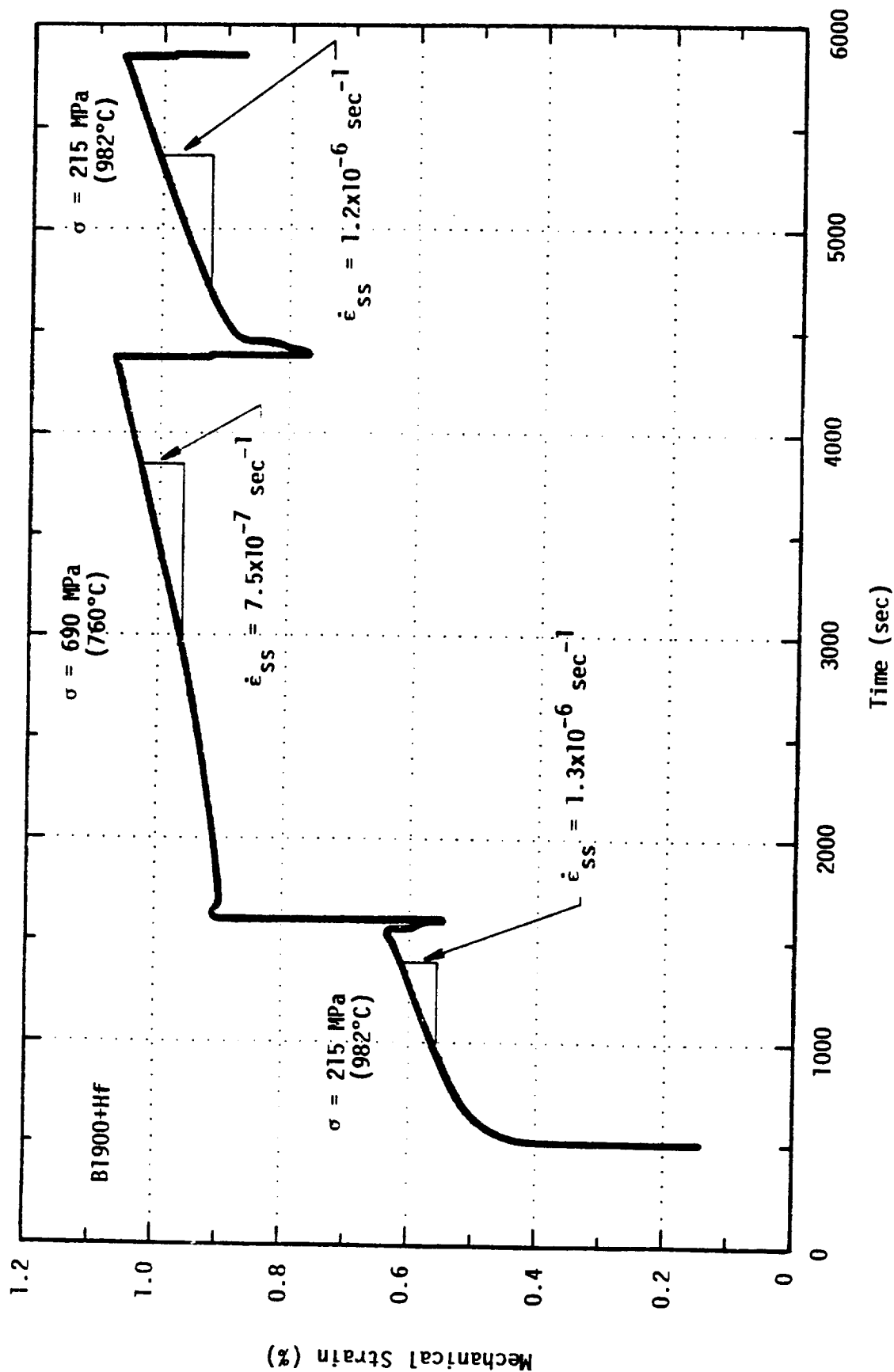


FIGURE 3.16 NONISOTHERMAL CONSTANT LOAD CREEP DATA OF B1900+Hf FOR TEST CONDITIONS OF $\sigma = 215$ MPa AND $T = 982^\circ\text{C}$ WITH SUBSEQUENT STRESS AND TEMPERATURE CHANGES TO $\sigma = 690$ MPa AND $T = 760^\circ\text{C}$ AND FINALLY TO $\sigma = 215$ MPa AND $T = 982^\circ\text{C}$

to 215 MPa and the temperature to 982°C. The new steady-state creep rate then becomes $1.2 \times 10^{-6} \text{ sec}^{-1}$, which is essentially the same as that obtained initially under similar test conditions. In Figure 3.17, the specimen (K6) was initially subjected to 690 MPa and 760°C which upon reaching steady state conditions, was changed to 215 MPa and 982°C. Examination of the test results in Figures 3.16 and 3.17 indicates that the steady-state creep rate of B1900+Hf depends on temperature and the applied stress, but not on the thermal history to within the experimental error. This conclusion also holds for creep behavior at 649°C. As shown in Figure 3.18, the creep rate for B1900+Hf at 690 MPa and 649°C, both before and after creep at 871°C and 427 MPa, was essentially zero. Because of the lack of thermal history effects, comparison of the nonisothermal creep data with those obtained isothermally in Figure 3.19 indicates good agreement between the two set of creep data, as well as with the Bodner-Partom and Walker models.

3.4.3 Nonisothermal Cyclic Tests

As in the nonisothermal tensile tests, the nonisothermal (step temperature) cyclic tests were performed at temperature ranges either in the thermal recovery regime ($T > 760^\circ\text{C}$) or the "strain-aging" range ($538^\circ\text{C} < T < 760^\circ\text{C}$). In Figure 3.20, the specimen was strained at $\pm 0.4\%$ at 538°C until cyclic saturation. The test temperature was then increased to 760°C and was held at peak strain (0.4%) for two hours. There was a slight stress relaxation during strain hold, as shown in Figure 3.21(a). After reducing the test temperature to 538°C, strain cycling was resumed at $\pm 0.4\%$, and the obtained saturated hysteresis stress-strain loops were essentially identical to those observed before the strain hold. The Bodner-Partom model predicted hysteresis loops, shown in Figure 3.21(b), which show fair agreement in the stress levels, both during cycling and strain hold.

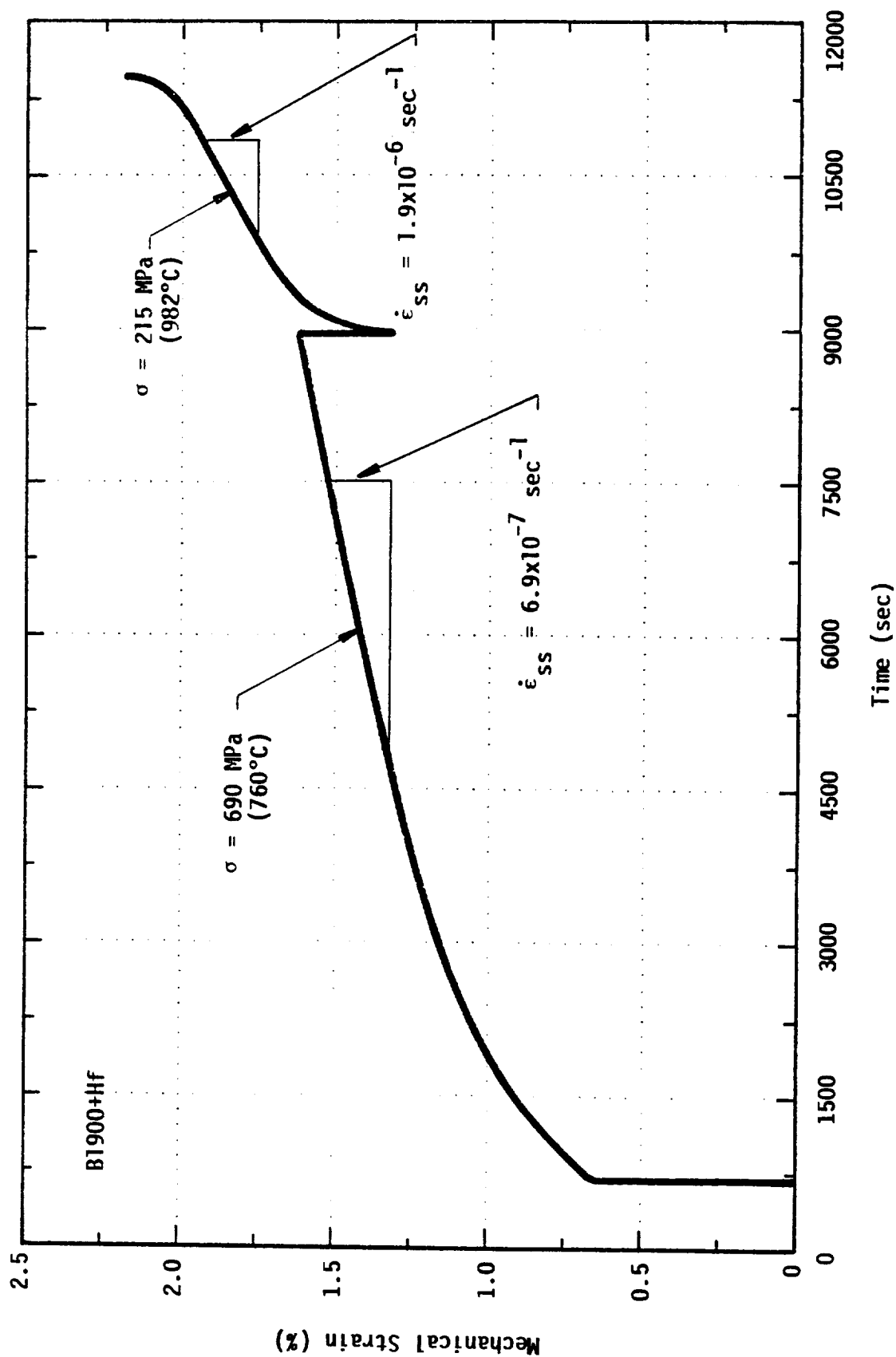


FIGURE 3.17 NONISOTHERMAL CONSTANT LOAD CREEP DATA OF B1900+Hf FOR TEST CONDITIONS OF $\sigma = 690$ MPa AND $T = 760^\circ\text{C}$ WITH SUBSEQUENT STRESS AND TEMPERATURE CHANGES TO $\sigma = 215$ MPa AND $T = 982^\circ\text{C}$

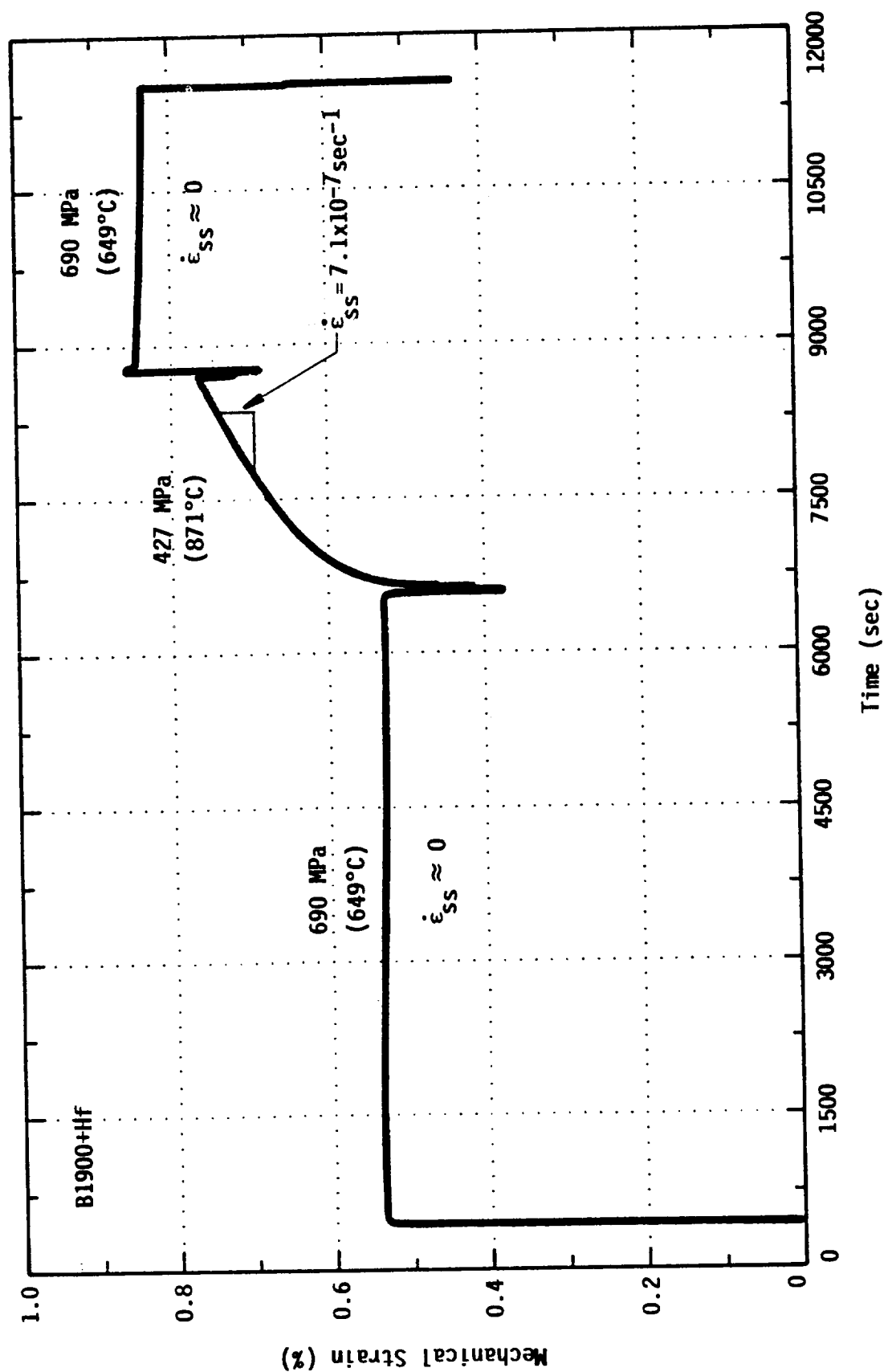


FIGURE 3.18 NONISOTHERMAL CONSTANT LOAD CREEP DATA OF B1900+Hf FOR TEST CONDITIONS OF
 $\sigma = 690 \text{ MPa}$ AND $T = 649^\circ\text{C}$ WITH SUBSEQUENT STRESS AND TEMPERATURE CHANGES
 TO $\sigma = 427 \text{ MPa}$ AND $T = 871^\circ\text{C}$ AND FINALLY TO $\sigma = 690 \text{ MPa}$ AND $T = 649^\circ\text{C}$

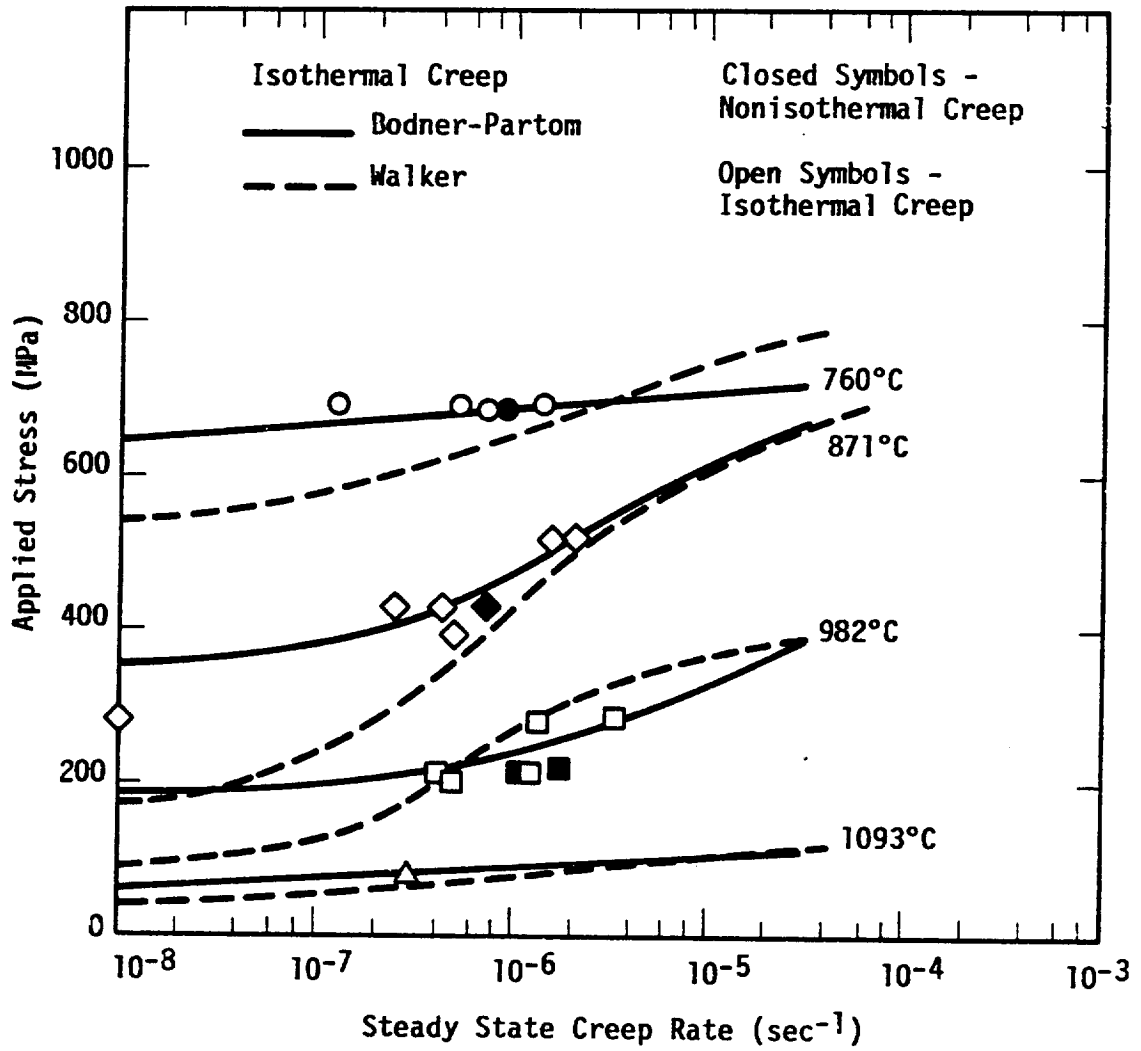


FIGURE 3.19 COMPARISON OF NONISOTHERMAL CREEP DATA WITH ISOTHERMAL CREEP DATA AND MODEL PREDICTIONS

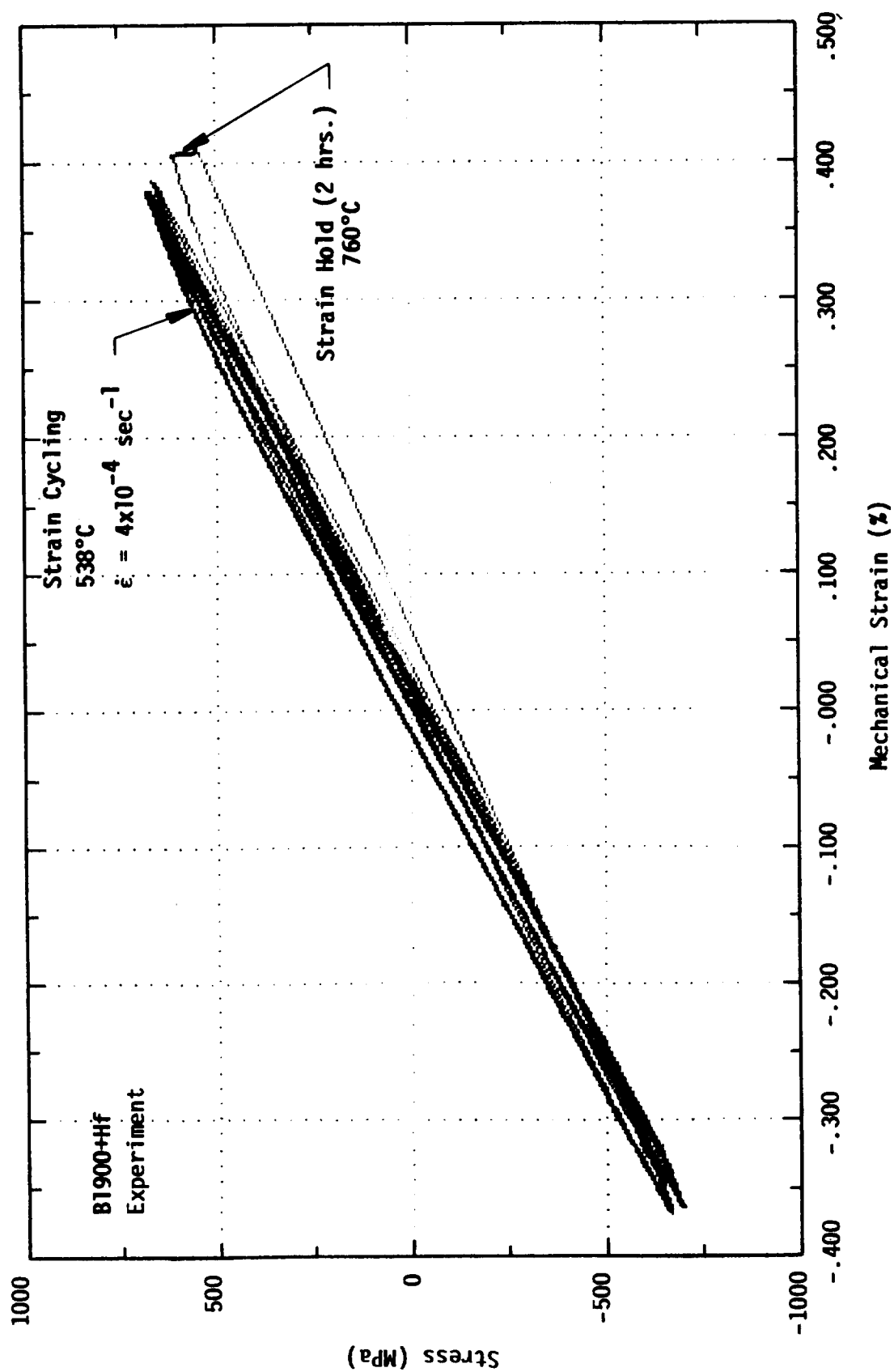


FIGURE 3.20 STRESS-STRAIN RESPONSE OF B1900+Hf SUBJECTED TO STRAIN CYCLING AT 538°C UNTIL CYCLIC SATURATION, STRAIN HOLD AT 760°C FOR TWO HOURS, AND THEN STRAIN CYCLING AT 538°C. The applied strain range is $\approx \pm 0.4\%$ at $\dot{\epsilon} = 4 \times 10^{-4} \text{ sec}^{-1}$.

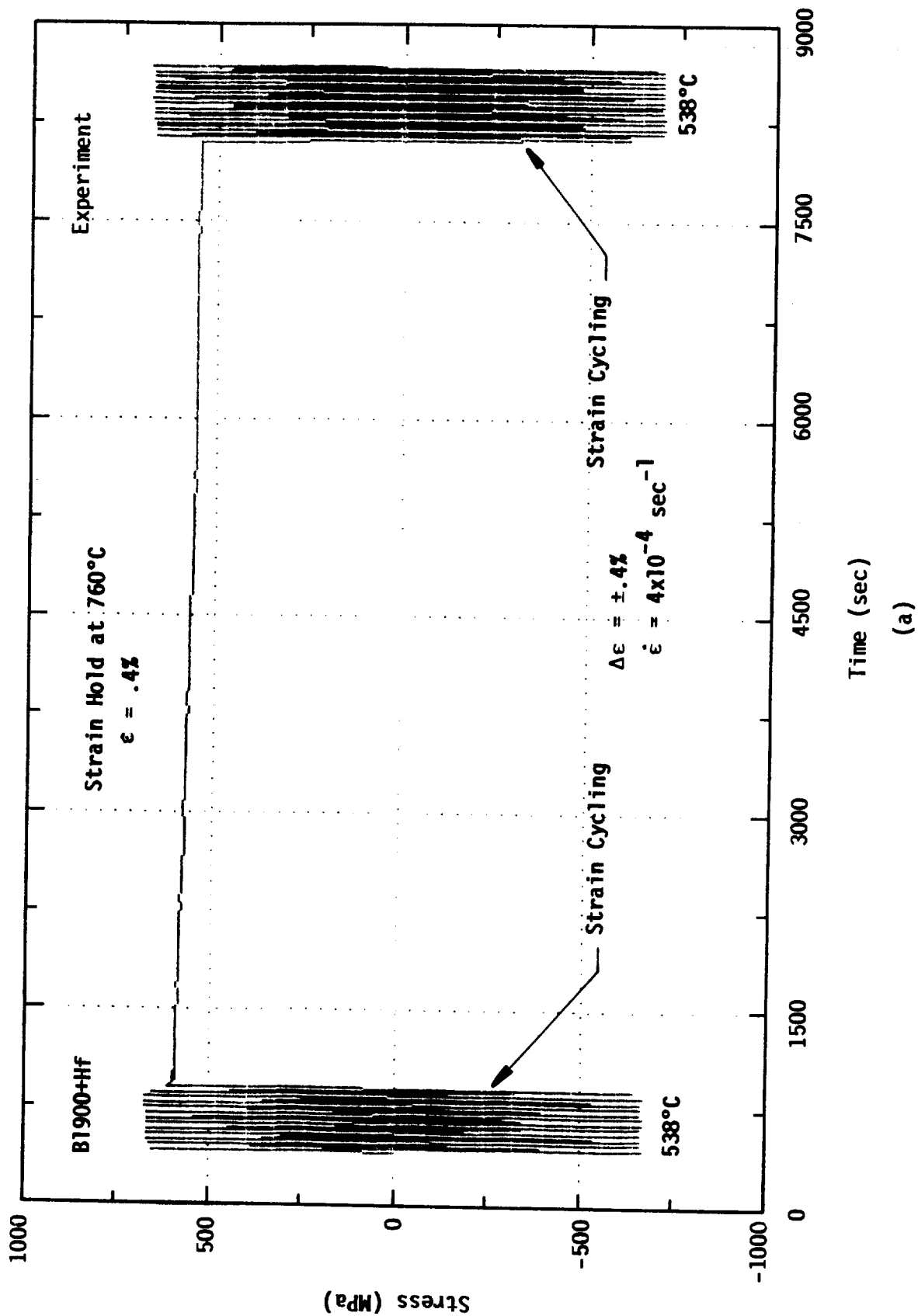


FIGURE 3.21 STRESS-TIME RESPONSE OF B1900+Hf SUBJECTED TO STRAIN CYCLING AT 538°C UNTIL CYCLIC SATURATION, STRAIN HOLD AT 760°C FOR TWO HOURS, AND THEN STRAIN CYCLING AT 538°C. The applied strain range is $\approx \pm.4\%$ at $\dot{\epsilon} = 4 \times 10^{-4} \text{ sec}^{-1}$: (a) experiment, and (b) model prediction.

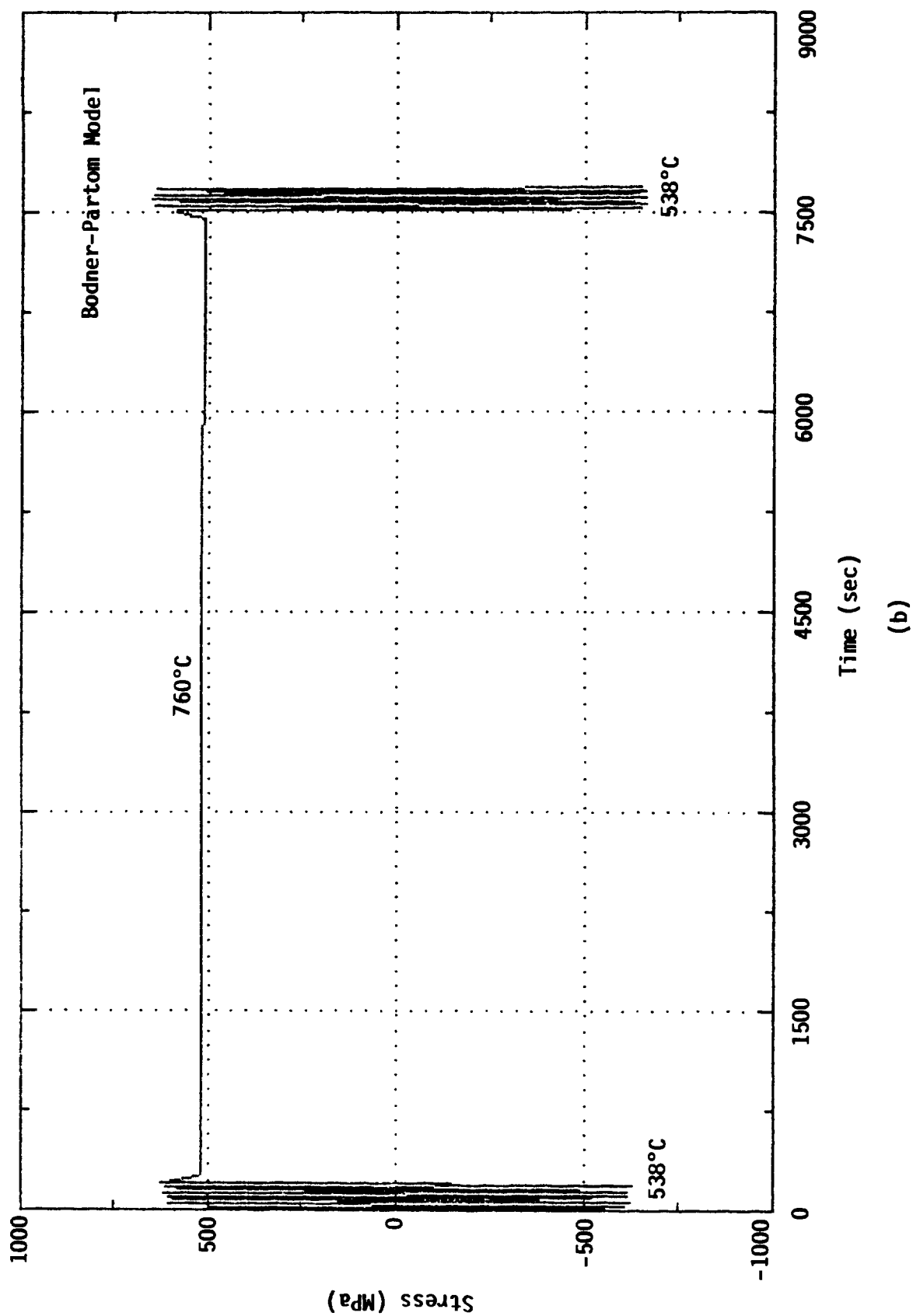


FIGURE 3.21 (CONTINUED) STRESS-TIME RESPONSE OF B1900+Hf SUBJECTED TO STRAIN CYCLING AT 538°C UNTIL CYCLIC SATURATION, STRAIN HOLD AT 760°C FOR TWO HOURS, AND THEN STRAIN CYCLING AT 538°C. The applied strain range is $\approx \pm 4\%$ at $\dot{\epsilon} = 4 \times 10^{-4} \text{ sec}^{-1}$: (a) experiment, and (b) model prediction.

A strain cycle similar to the one described in the previous paragraph was conducted on another specimen, but with strain hold at 982°C (Figure 3.22). Increasing the temperature for strain hold increased the amount of stress relaxation [Figure 3.23(a)]. Subsequent strain cycling at 538°C resulted in saturated hysteresis loops which were again essentially identical to those obtained before the strain hold. The Bodner-Partom model calculations for this strain cycle are shown in Figure 3.23(b).

Additional cyclic tests were conducted under nonisothermal and continuous straining conditions. Figure 3.24 shows the hysteresis loops for B1900+Hf strained at $\dot{\epsilon} = 4 \times 10^{-4} \text{ sec}^{-1}$ and 538°C until cyclic saturation. The test temperature was then increased to 982°C, while the specimen was under concurrent strain cycling. After cyclic saturation occurred at 982°C, the test temperature was reduced to 538°C with the specimen under the same imposed strain cycling conditions. The subsequent cyclic saturated hysteresis loops at 538°C were found to be identical to those obtained before the nonisothermal histories were imposed (Figure 3.24). Rearranging the test temperature sequences to strain cycling at 982°C, 538°C, and then 982°C produced similar results with the cyclic saturated hysteresis loops for 982°C before and after thermal excursion to 538°C being identical (Figure 3.25).

Figure 3.26(a) shows the nonisothermal cyclic results for the case in which the specimen (1F) was cycled at $\Delta\epsilon = \pm 0.4\%$ initially at 760°C. After cyclic saturation, the test temperature was reduced to 538°C while the same strain cycling conditions were maintained. When cyclic saturation was achieved at 538°C, the temperature was then increased to 760°C, and strain cycling continued until saturation. The whole strain/temperature cycling histories were also repeated for $\Delta\epsilon = \pm 0.6\%$, and the results are shown in Figure 3.26(b). As shown in Figures 3.26(a) and (b), the cyclically saturated

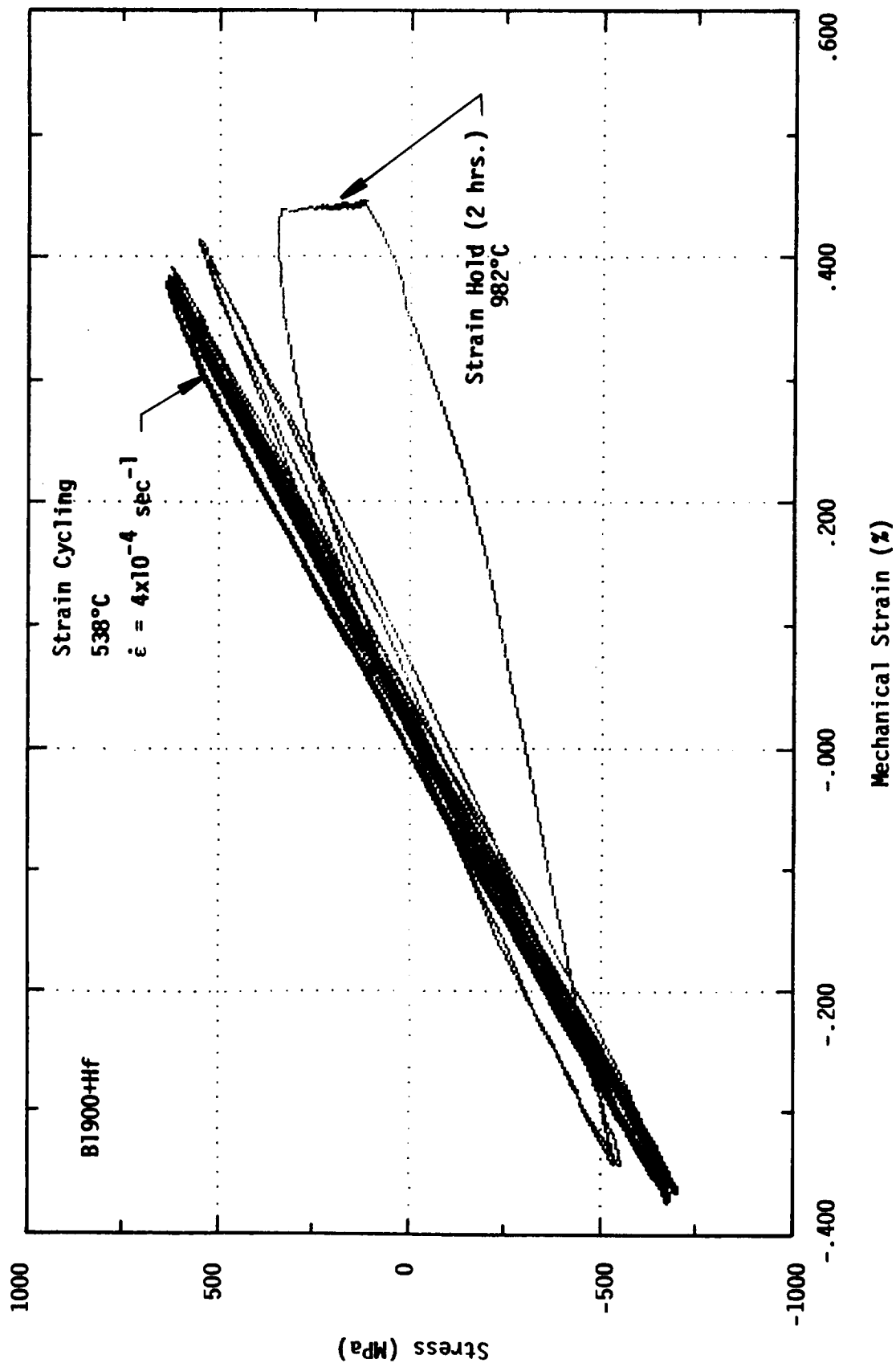


FIGURE 3.22 STRESS-STRAIN RESPONSE OF B1900+Hf SUBJECTED TO STRAIN CYCLING AT 538°C UNTIL CYCLIC SATURATION, STRAIN HOLD AT 982°C FOR TWO HOURS, AND THEN STRAIN CYCLING AT 538°C. The applied strain range is $\approx \pm 0.4\%$ at $\dot{\epsilon} = 4 \times 10^{-4} \text{ sec}^{-1}$.

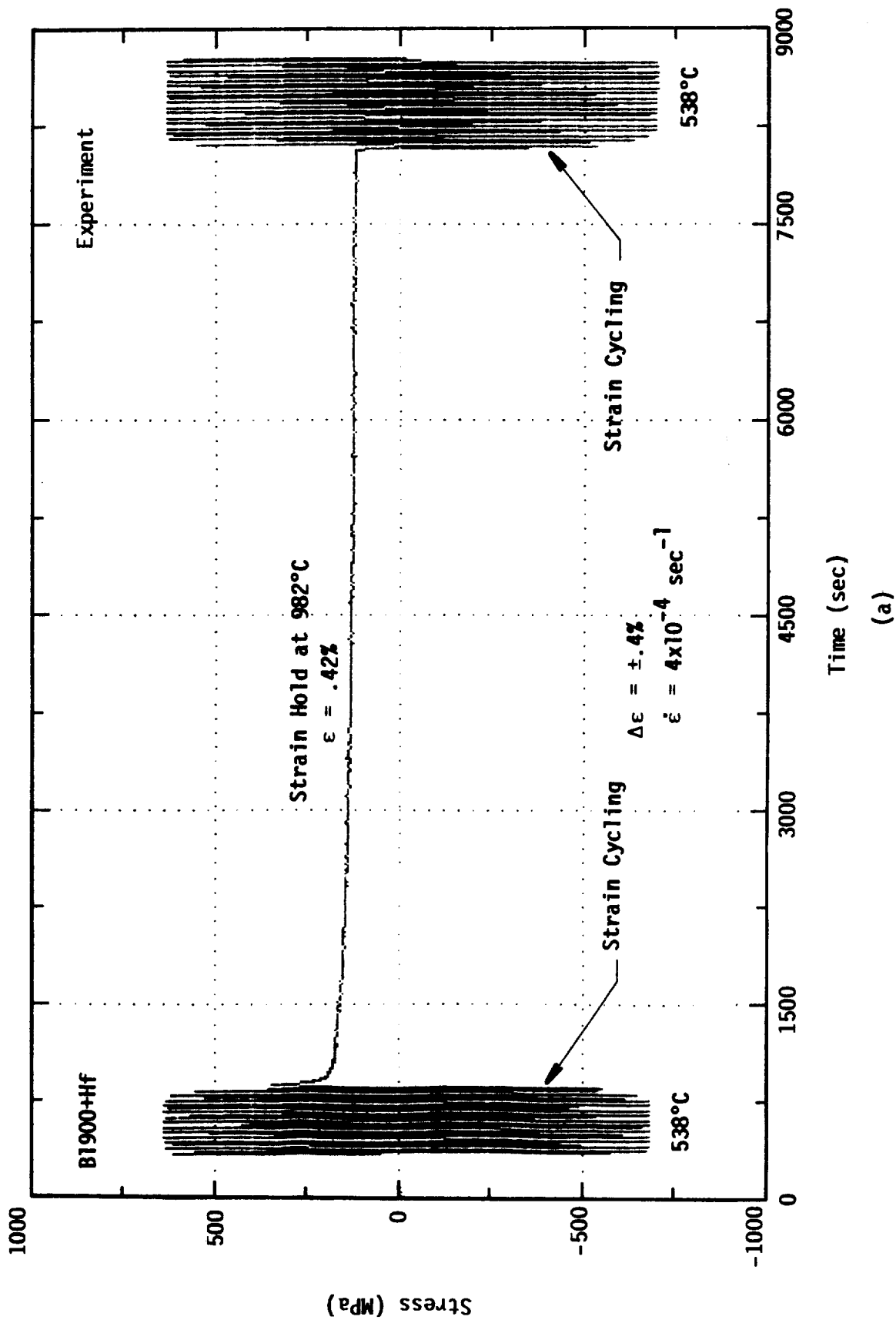


FIGURE 3.23 STRESS-TIME RESPONSE OF B1900+HF SUBJECTED TO STRAIN CYCLING AT 538°C UNTIL CYCLIC SATURATION, STRAIN HOLD AT 982°C FOR TWO HOURS, AND THEN STRAIN CYCLING AT 538°C. The applied strain range is $\approx \pm 0.4\%$ at $\dot{\epsilon} = 4 \times 10^{-4} \text{ sec}^{-1}$: (a) experiment, and (b) model prediction.

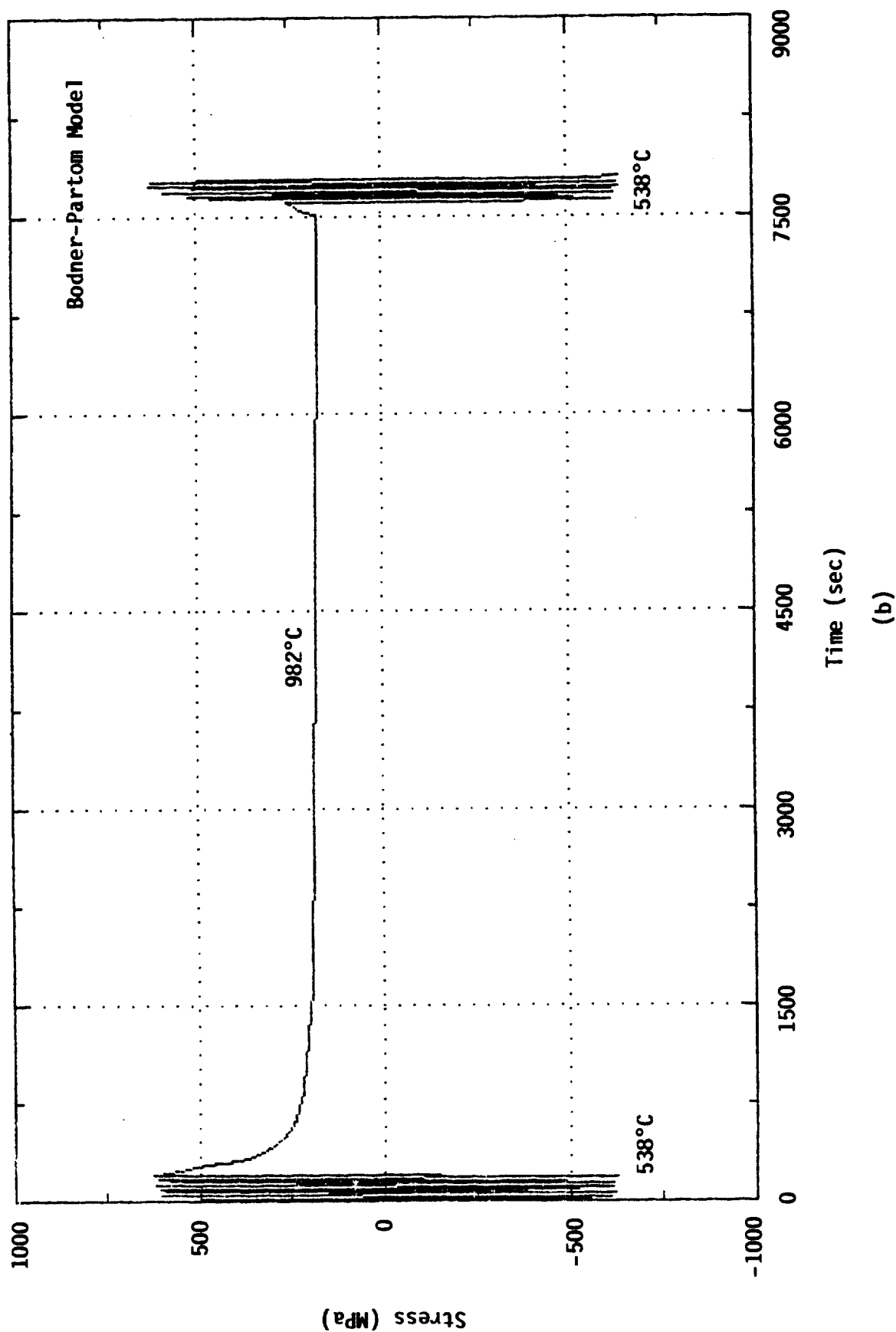


FIGURE 3.23 (CONTINUED) STRESS-TIME RESPONSE OF B1900+Hf SUBJECTED TO STRAIN CYCLING AT 538°C UNTIL CYCLIC SATURATION, STRAIN HOLD AT 982°C FOR TWO HOURS, AND THEN STRAIN CYCLING AT 538°C. The applied strain range is $\approx \pm 0.4\%$ at $\dot{\epsilon} = 4 \times 10^{-4} \text{sec}^{-1}$: (a) experiment, and (b) model prediction.

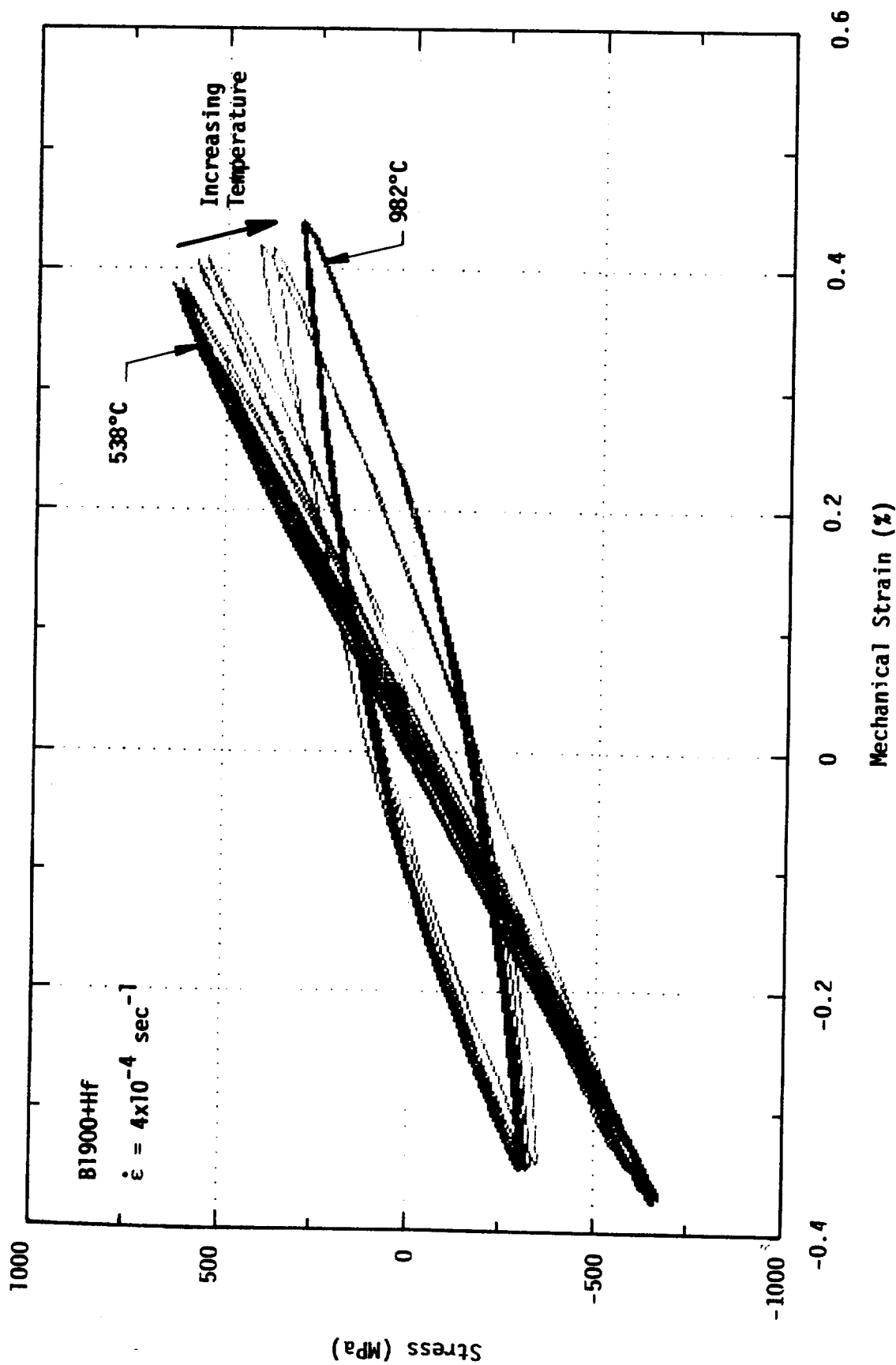


FIGURE 3.24 STRESS-STRAIN RESPONSE OF B1900+Hf SUBJECTED TO STRAIN CYCLING (1) AT 538°C UNTIL CYCLIC SATURATION, (2) AT 982°C UNTIL CYCLIC SATURATION, AND (3) AT 538°C UNTIL CYCLIC SATURATION. The applied strain range is $\approx \pm 0.4\%$ at $\dot{\epsilon} = 4 \times 10^{-4} \text{ sec}^{-1}$. The hysteresis loops in (1) and (3) are essentially identical.

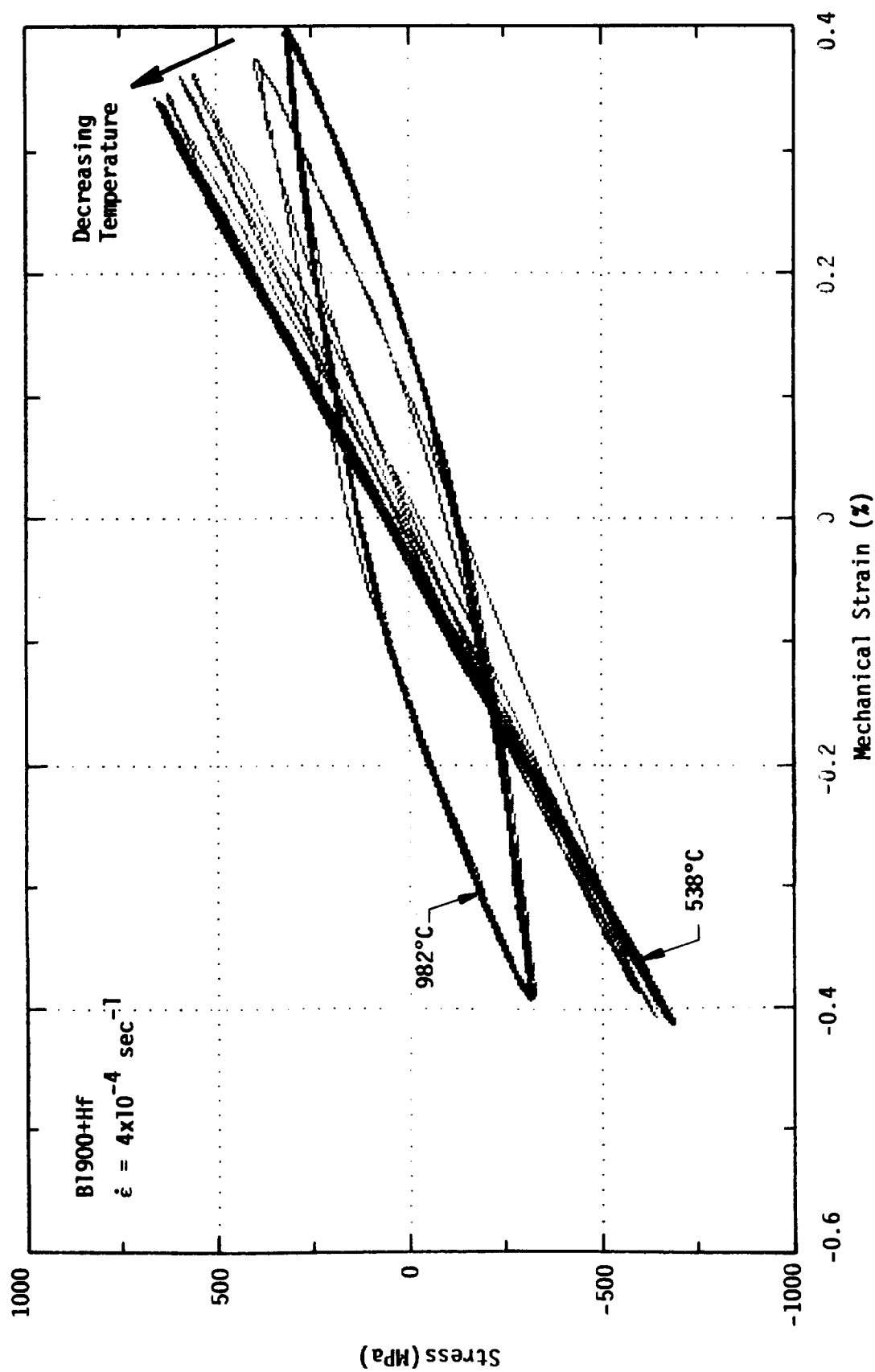


FIGURE 3.25 STRESS-STRAIN RESPONSE OF B1900+Hf SUBJECTED TO STRAIN CYCLING (1) AT 982°C UNTIL CYCLIC SATURATION, (2) AT 538°C UNTIL CYCLIC SATURATION, AND (3) AT 982°C UNTIL CYCLIC SATURATION. The applied strain range is $\pm 0.4\%$ at $\dot{\epsilon} = 4 \times 10^{-4} \text{ sec}^{-1}$. The hysteresis loops in (1) and (3) are essentially identical.

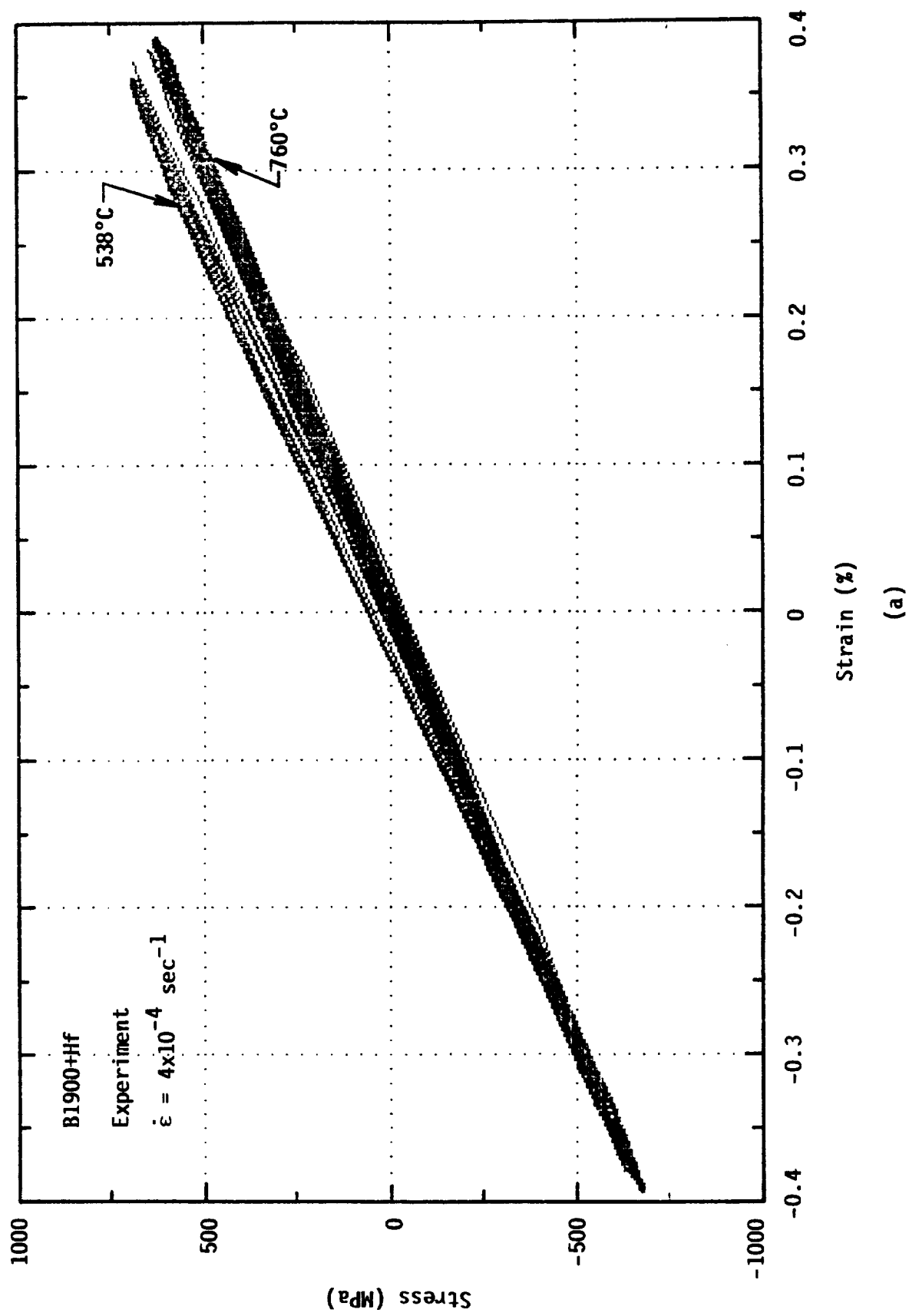


FIGURE 3.26 HYSTERESIS LOOPS OF B1900+Hf SUBJECTED TO STRAIN CYCLING AT 760°C WITH SUBSEQUENT TEMPERATURE CHANGES TO 538°C AND 760°C: (a) $\Delta\epsilon = \pm 0.4\%$ and (b) $\Delta\epsilon = \pm 0.6\%$. The temperature changes were made after cyclic saturation was obtained

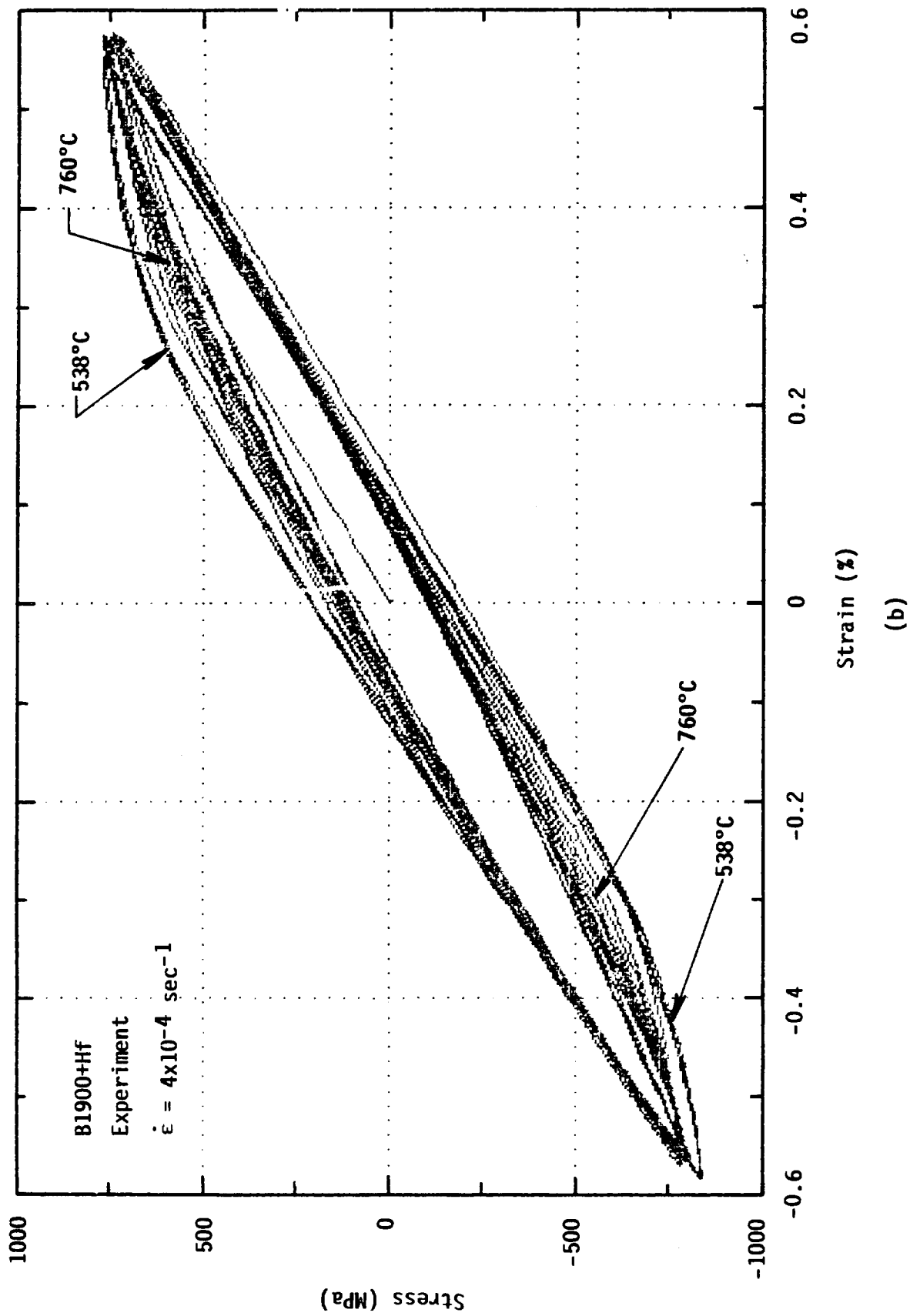


FIGURE 3.26 (CONTINUED) HYSTERESIS LOOPS OF B1900+HF SUBJECTED TO STRAIN CYCLING AT 760°C WITH SUBSEQUENT TEMPERATURE CHANGES TO 538°C AND 760°C: (a) $\Delta\epsilon = \pm 0.4\%$ and (b) $\Delta\epsilon = \pm 0.6\%$. The temperature changes were made after cyclic saturation was obtained.

hysteresis loops of B1900+Hf for $T = 760^{\circ}\text{C}$ do not depend on thermal history when strain cycled at $\Delta\epsilon \approx \pm 0.4\%$ and $\Delta\epsilon \approx \pm 0.6\%$ with temperature changes from 760°C to 538°C and then back to 760°C .

Comparisons of the nonisothermal cyclic data with previously obtained isothermal cyclic data shown in Figures 3.27, 3.28, and 3.29 for 538°C , 760°C , and 982°C , respectively, indicate that the stress ranges of saturated hysteresis loops at a given strain range are independent of thermal history for specimens tested in either the strain aging regime (538°C) or in the regime where thermal recovery is important (982°C). These results are consistent with previous tensile and creep data obtained in the thermal recovery regime, which indicated that the saturation stresses and the steady state creep rates depend on the current temperature and loading conditions, but are independent of thermal history.

3.4.4 Thermomechanical Fatigue Tests

Two of the thermomechanical fatigue tests were performed in the temperature range of 538°C to 760°C . The strain rate was $1 \times 10^{-4} \text{ sec}^{-1}$, and the imposed strain ranges were $\pm 0.4\%$ and $\pm 0.6\%$ in each of the tests. In one test with Specimen 1B, the imposed strain was in-phase with temperature as both strain and temperature increased or decreased linearly with time. For the other test, on Specimen 1D, the imposed strain varied out-of-phase with temperature. Test results for both the in-phase and out-of-phase cycles in Figures 3.30-3.33 showed cyclic hardening at the hot end of the cycles (760°C) but not at the cold end (538°C). For the thermomechanical cycles at $\pm 0.6\%$ strain range, the Bodner-Partom model predictions are in good agreement with experiment as shown in Figures 3.31 and 3.33. For cases at which $\Delta\epsilon = \pm 0.4\%$, as shown in Figures 3.30 and 3.32, the Bodner-Partom model predicted

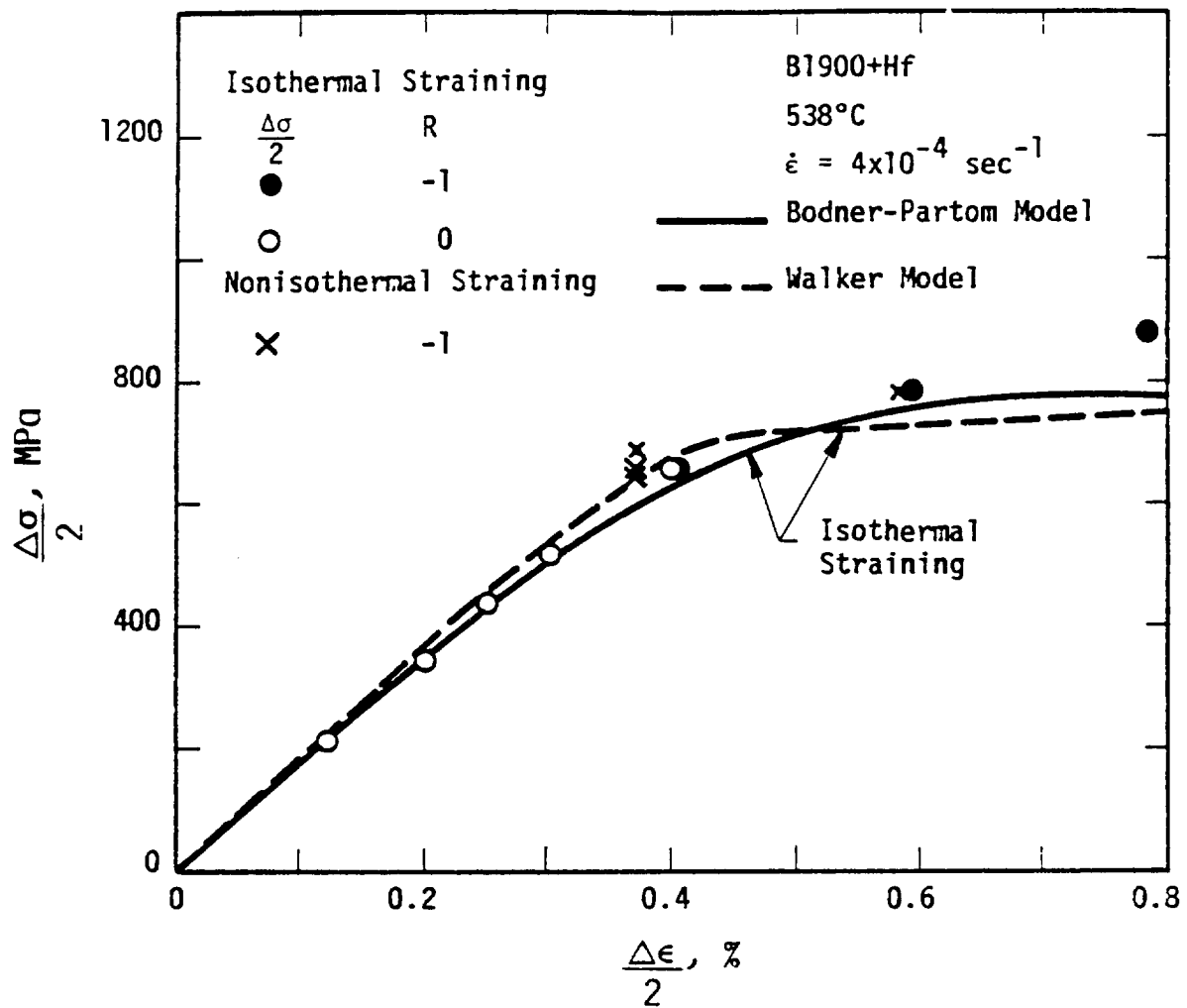


FIGURE 3.27 COMPARISON OF ISOTHERMAL AND NONISOTHERMAL CYCLIC DATA OF B1900+Hf AT 538°C

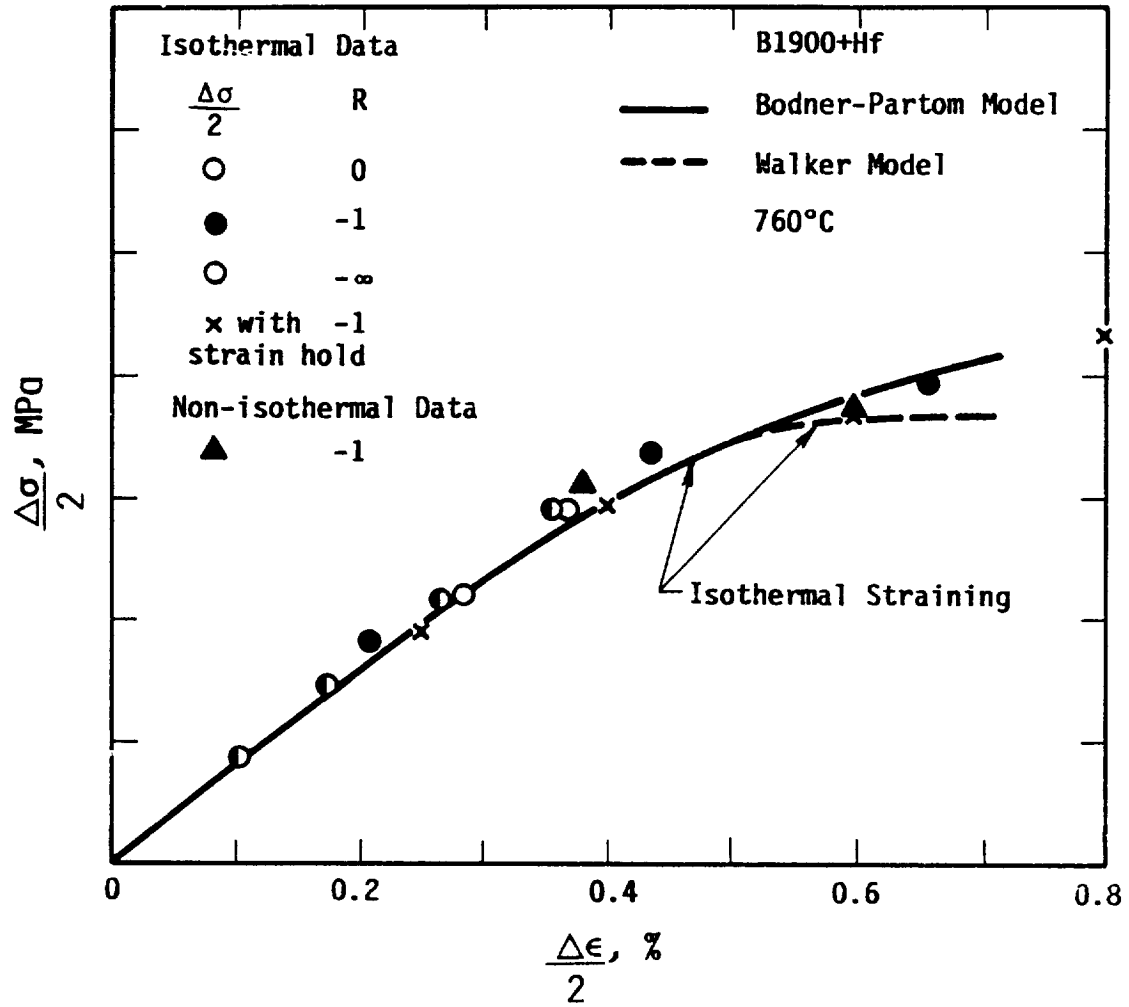


FIGURE 3.28 COMPARISON OF ISOTHERMAL AND NONISOTHERMAL CYCLIC DATA OF B1900+Hf AT 760°C

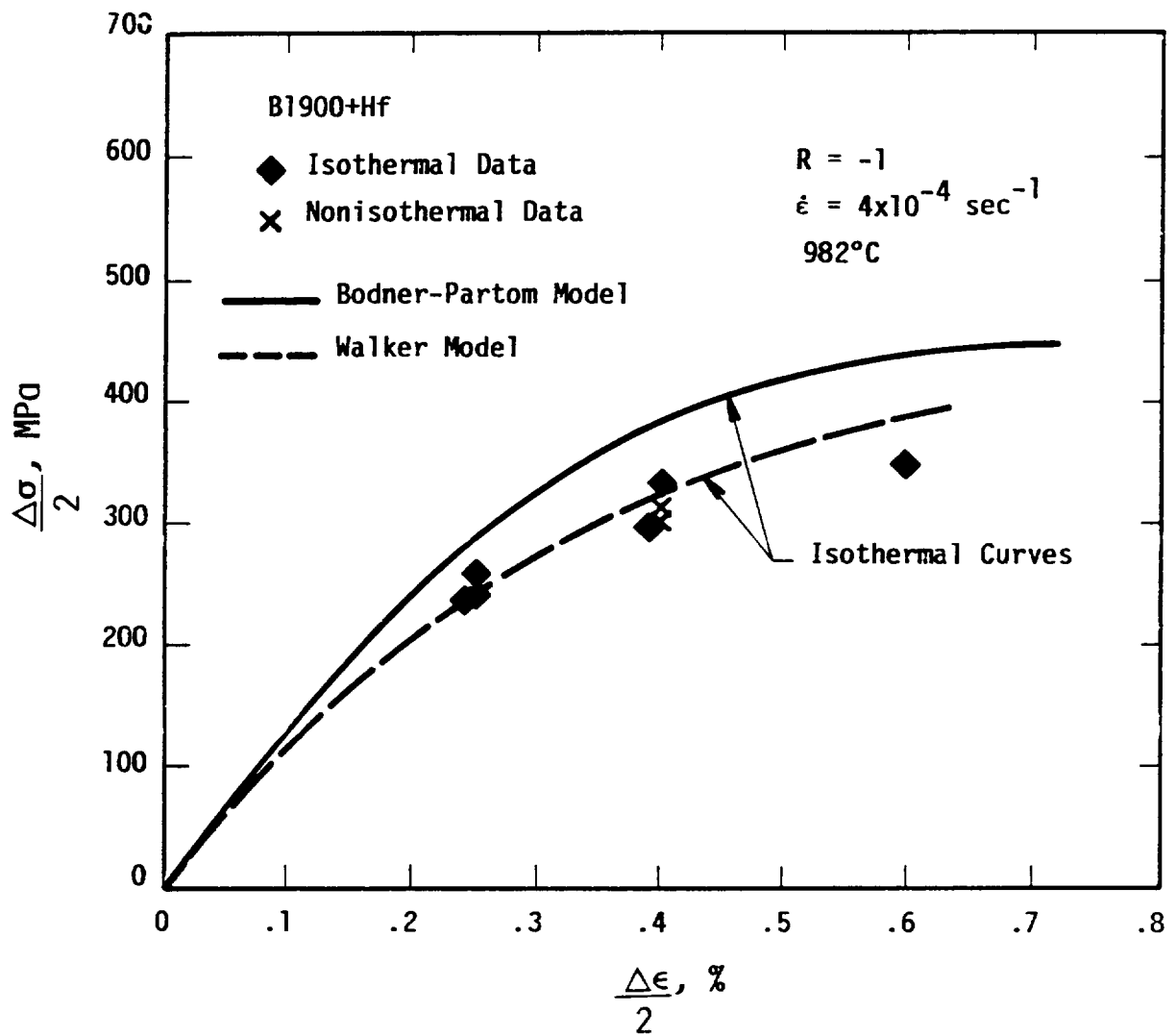


FIGURE 3.29 COMPARISON OF ISOTHERMAL AND NONISOTHERMAL CYCLIC DATA OF B1900+Hf AT 982°C

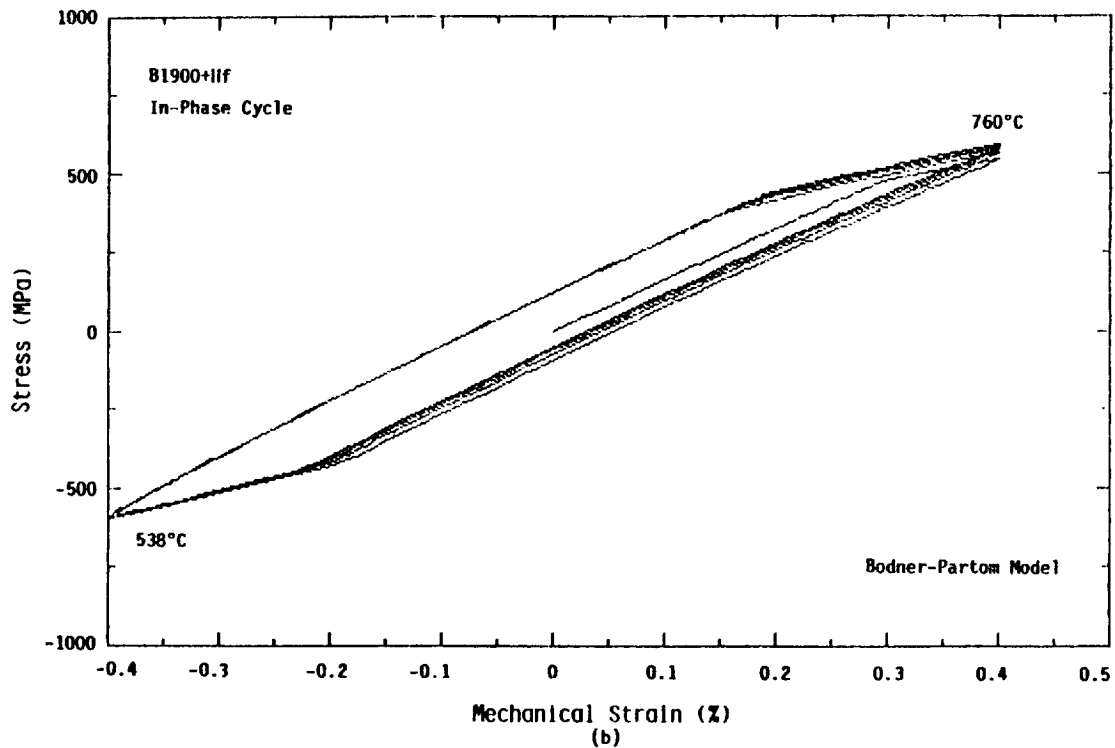
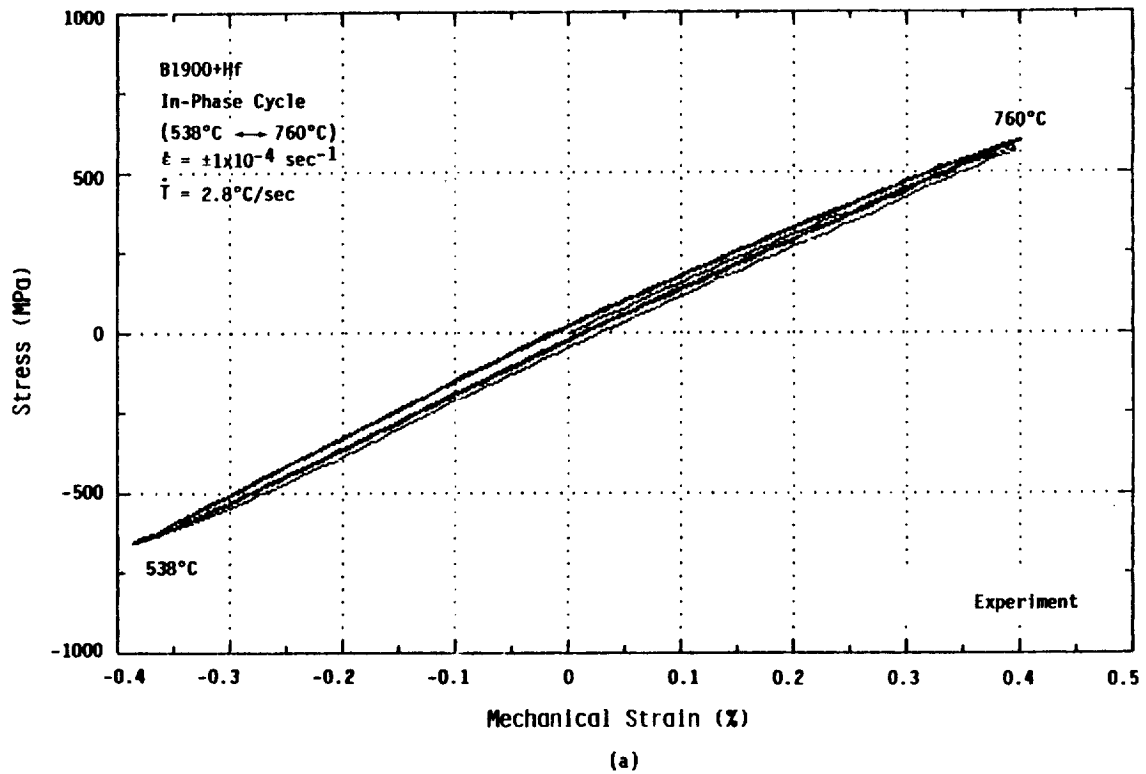


FIGURE 3.30 HYSTERESIS LOOPS OF B1900+Hf SUBJECTED TO IN-PHASE TMF
 LOADING UNDER A MECHANICAL STRAIN RANGE OF $\pm 0.4\%$:
 (a) experiment, and (b) Bodner-Partom model calculations.

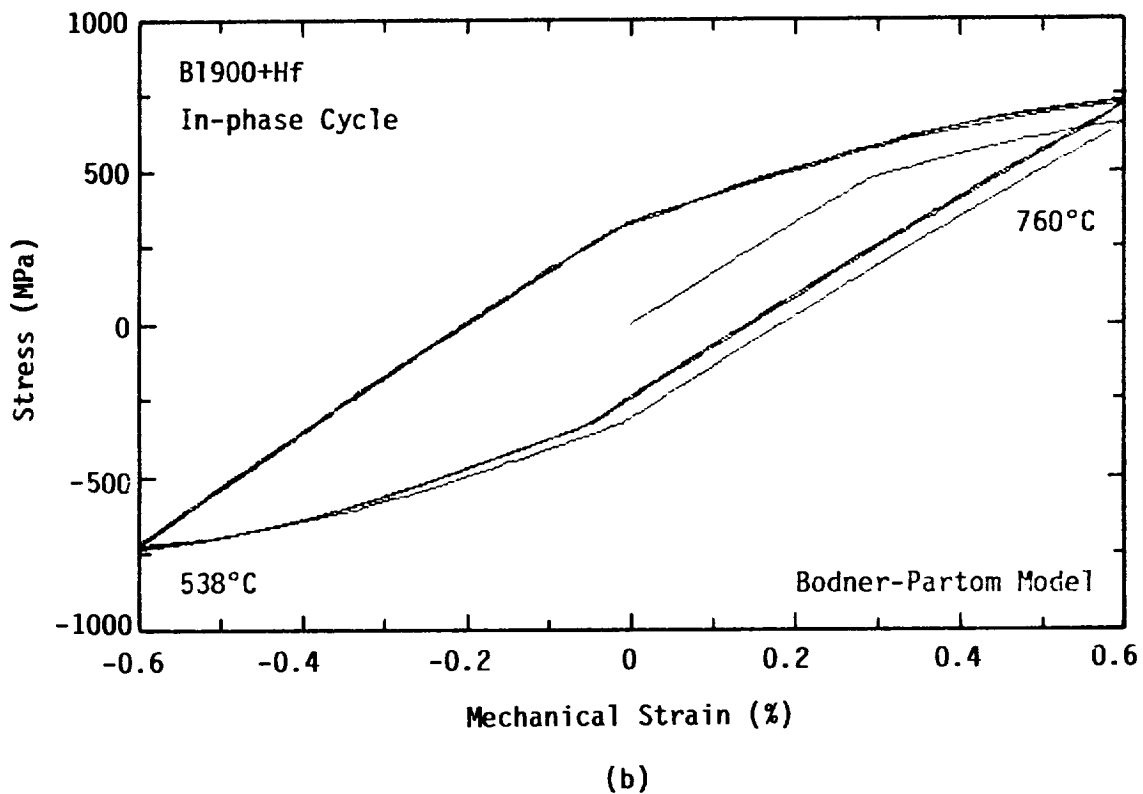
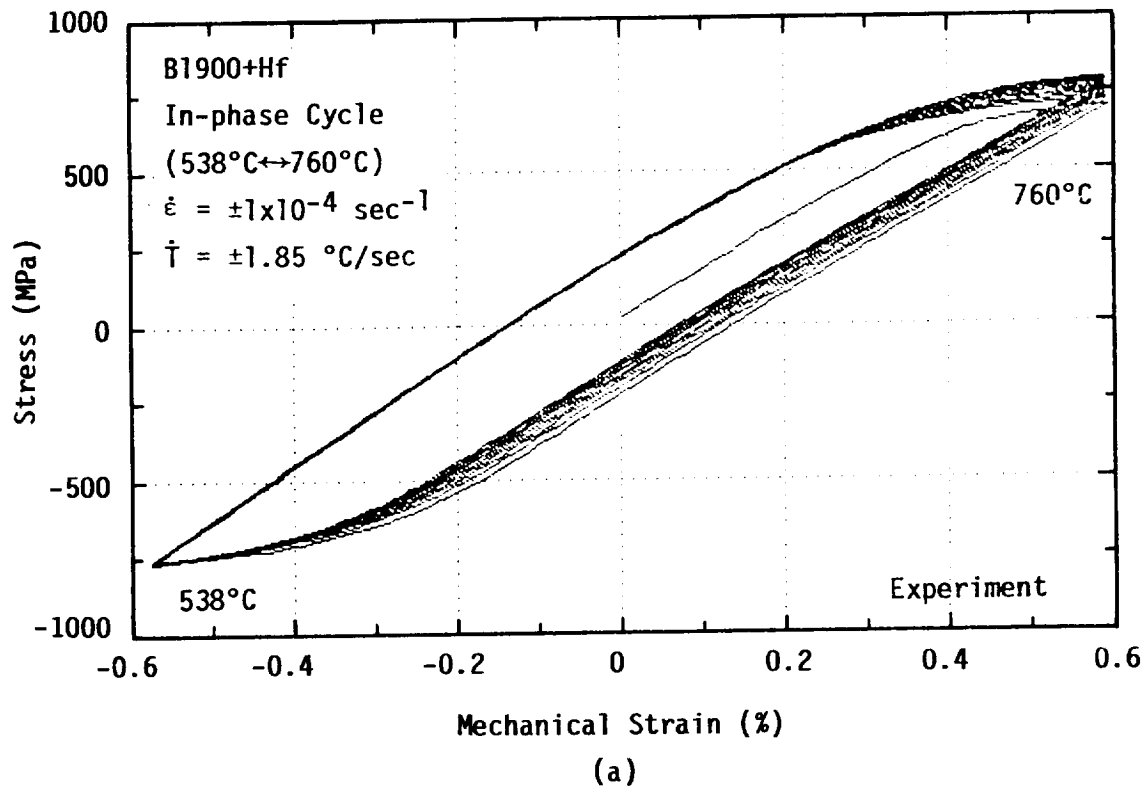


FIGURE 3.31 HYSTERESIS LOOPS OF B1900+Hf SUBJECTED TO IN-PHASE TMF
 LOADING UNDER A MECHANICAL STRAIN RANGE OF $\pm 0.6\%$:
 (a) experiment, and (b) Bodner-Partom model calculation.

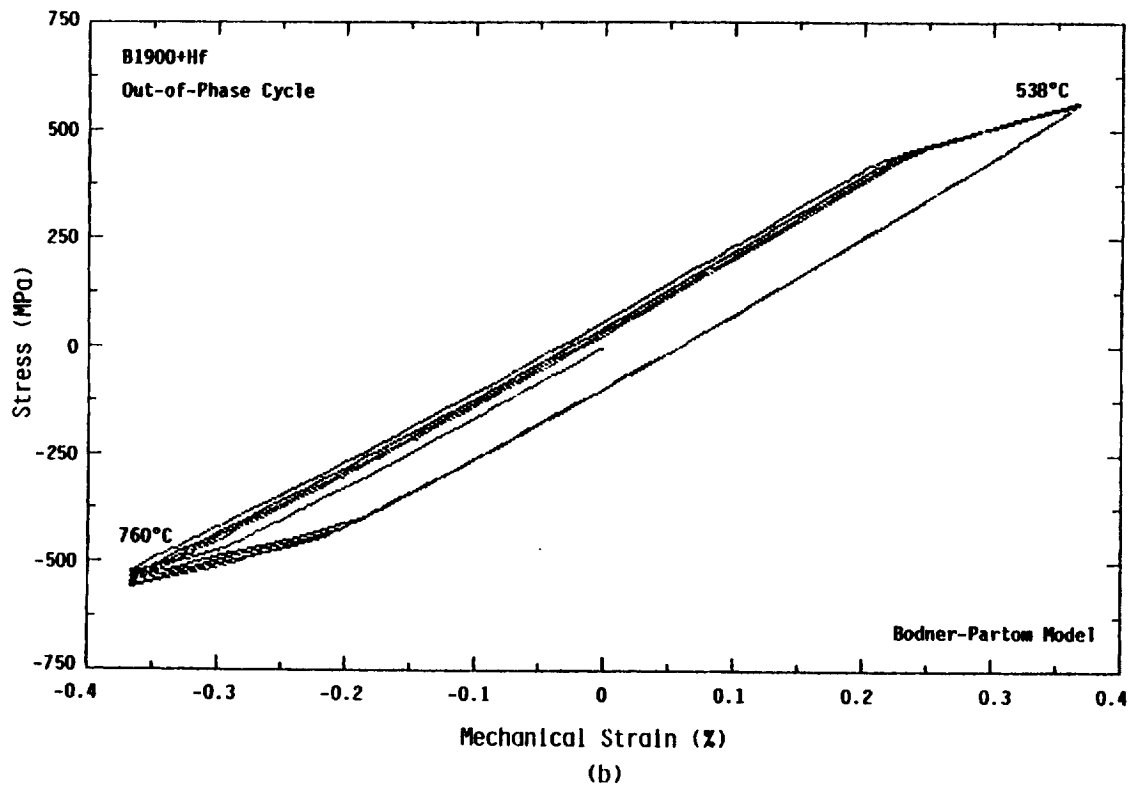
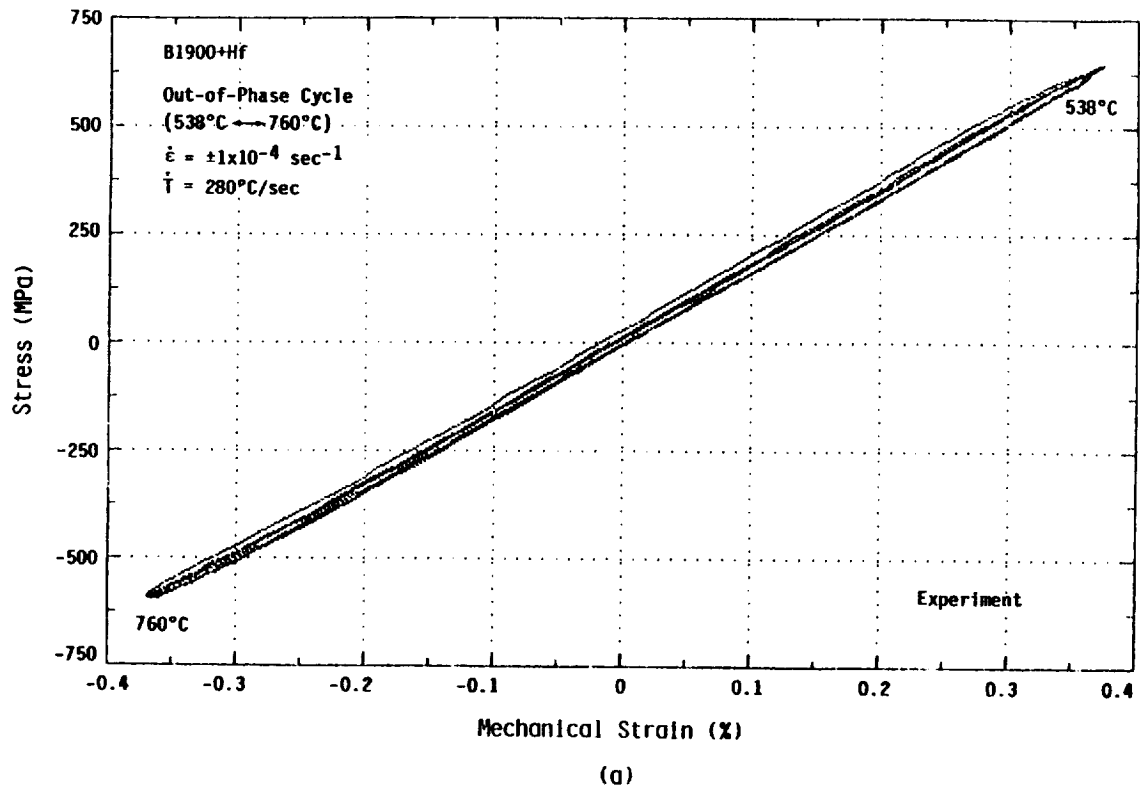
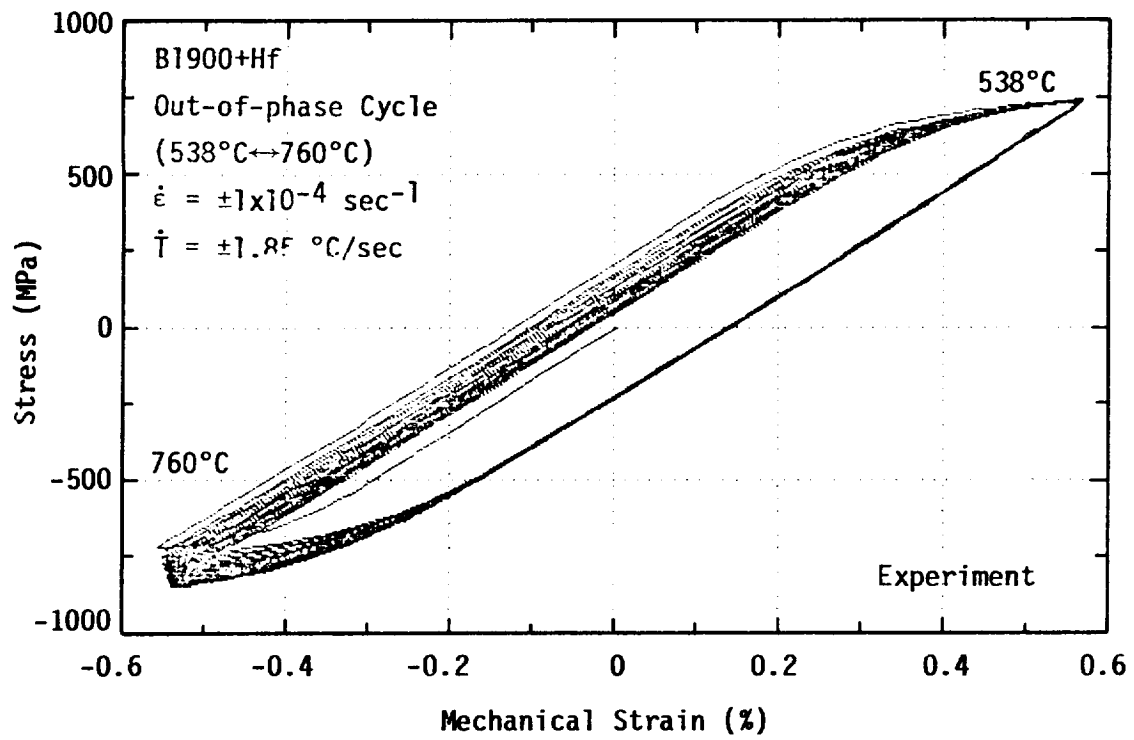
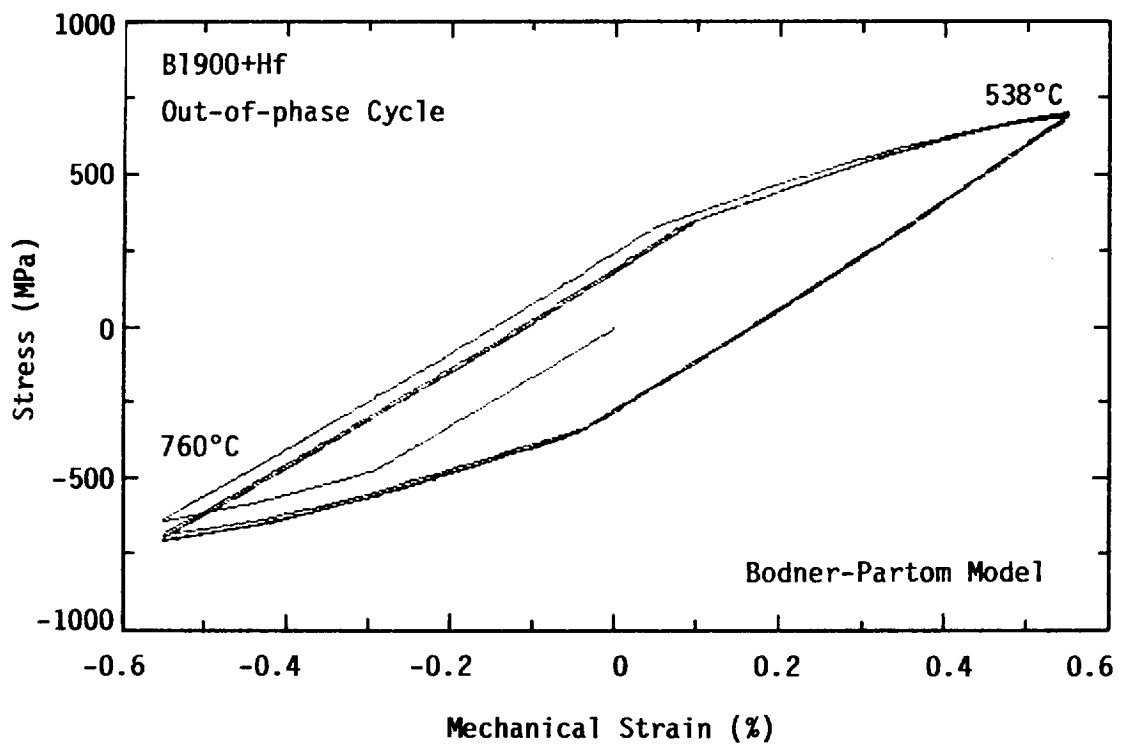


FIGURE 3.32 HYSTERESIS LOOPS OF B1900+Hf SUBJECTED TO OUT-OF-PHASE TMF LOADING UNDER A MECHANICAL STRAIN RANGE OF $\approx \pm 0.37\%$ IN THE 538-760°C RANGE: (a) experiment, and (b) Bodner-Partom model calculation.



(a)



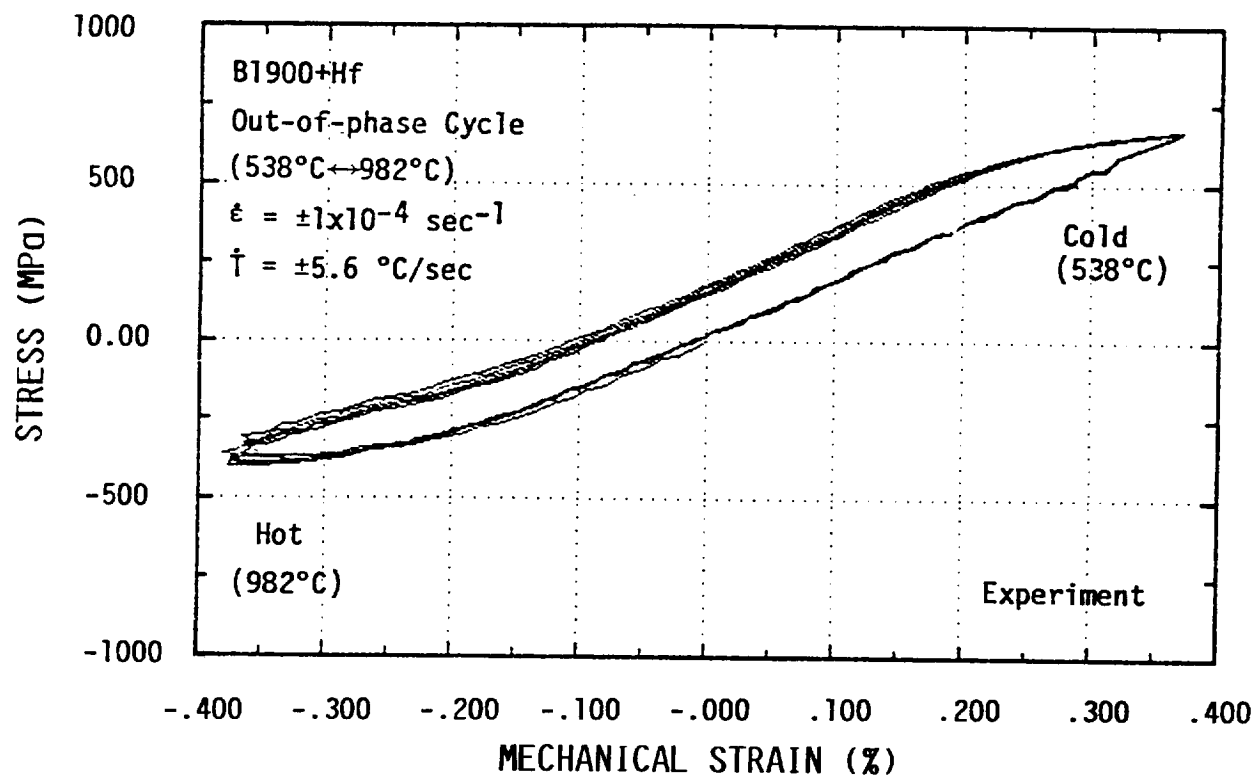
(b)

FIGURE 3.33 HYSTERESIS LOOPS OF B1900+Hf SUBJECTED TO OUT-OF-PHASE TMF LOADING UNDER A MECHANICAL STRAIN RANGE OF $\approx \pm 0.55\%$ IN THE 538 TO 760°C RANGE: (a) experiment, and (b) Bodner-Partom model calculation.

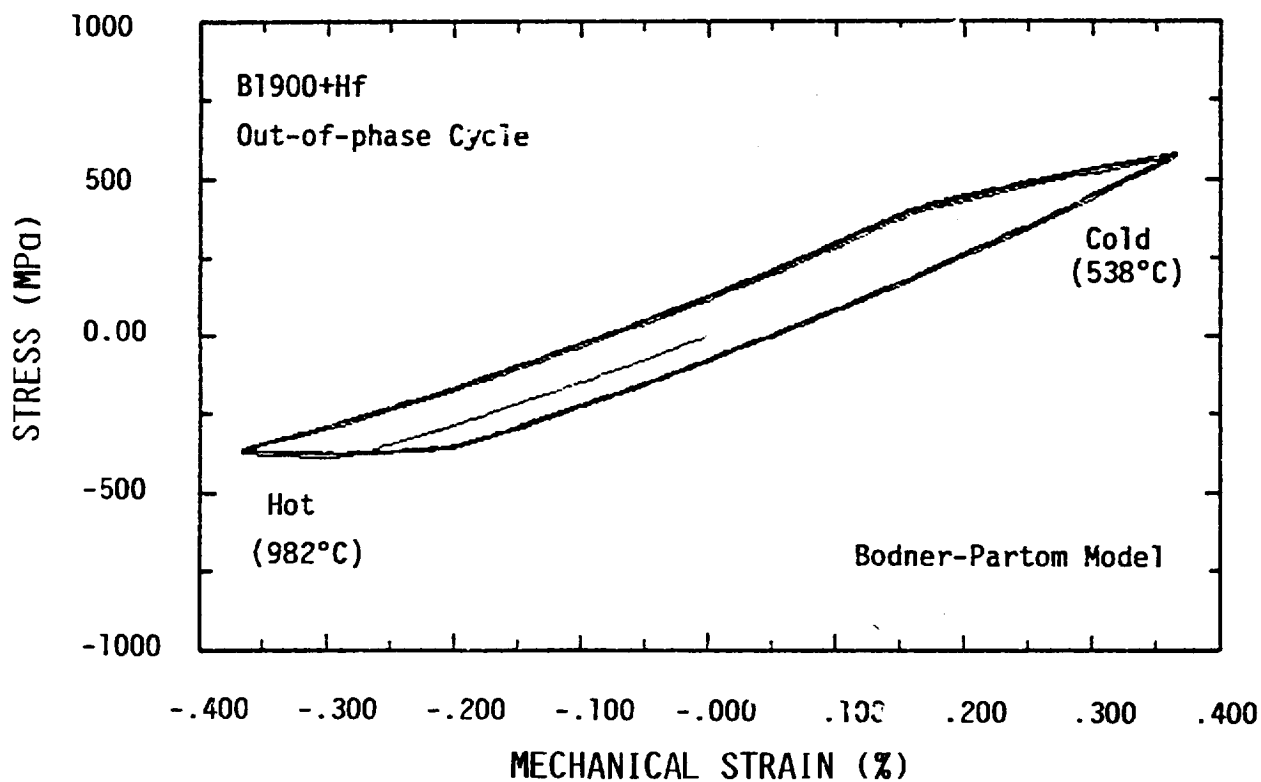
TMF loops are larger than that observed in the experiments. The discrepancies are primarily due to the small strain values ($\pm 0.4\%$) in the near yield region of the stress-strain curves, which is very sensitive to specimen variation and small differences in the values of the model constants. An interesting computational result is that the constitutive model does indicate some degree of cyclic hardening at the hot end of the cycle. This asymmetrical cyclic hardening is less pronounced than the test results and saturates more rapidly at the higher strain range.

The third thermomechanical fatigue test was an out-of-phase TMF cycle conducted in the temperature range of 538°C to 982°C at $\pm 0.4\%$ and $\pm 0.6\%$ strain ranges. Under these conditions, thermal recovery is present at the hot end of the cycle (982°C), while strain aging might be present at the cold end ($538\text{--}760^{\circ}\text{C}$). The type of unusual, asymmetric cyclic hardening observed in the two previous TMF cycles was not present in these strain cycles as shown in Figures 3.34 and 3.35. Comparison of the predicted curves with experimental results indicates good overall agreement between theory and experiment with slight underprediction of the stress near the cold end of the cycle (538°C). It should be noted that all the TMF calculations shown in Figures 3.30–3.35 were based on the Bodner-Partom model without any strain aging terms and which used material constants obtained from isothermal data.

The fourth TMF test was conducted on a B1900+Hf specimen (Specimen 1C) that was plasma sprayed with a yttrium-stabilized zirconia coating. The applied TMF cycle was identical to the out-of-phase cycle shown in Figures 3.34 and 3.35. The stress-strain response of the coated specimen, shown in Figures 3.36(a) and 3.36(b) for $\Delta\epsilon = \pm 0.4\%$ and $\pm 0.6\%$, respectively,

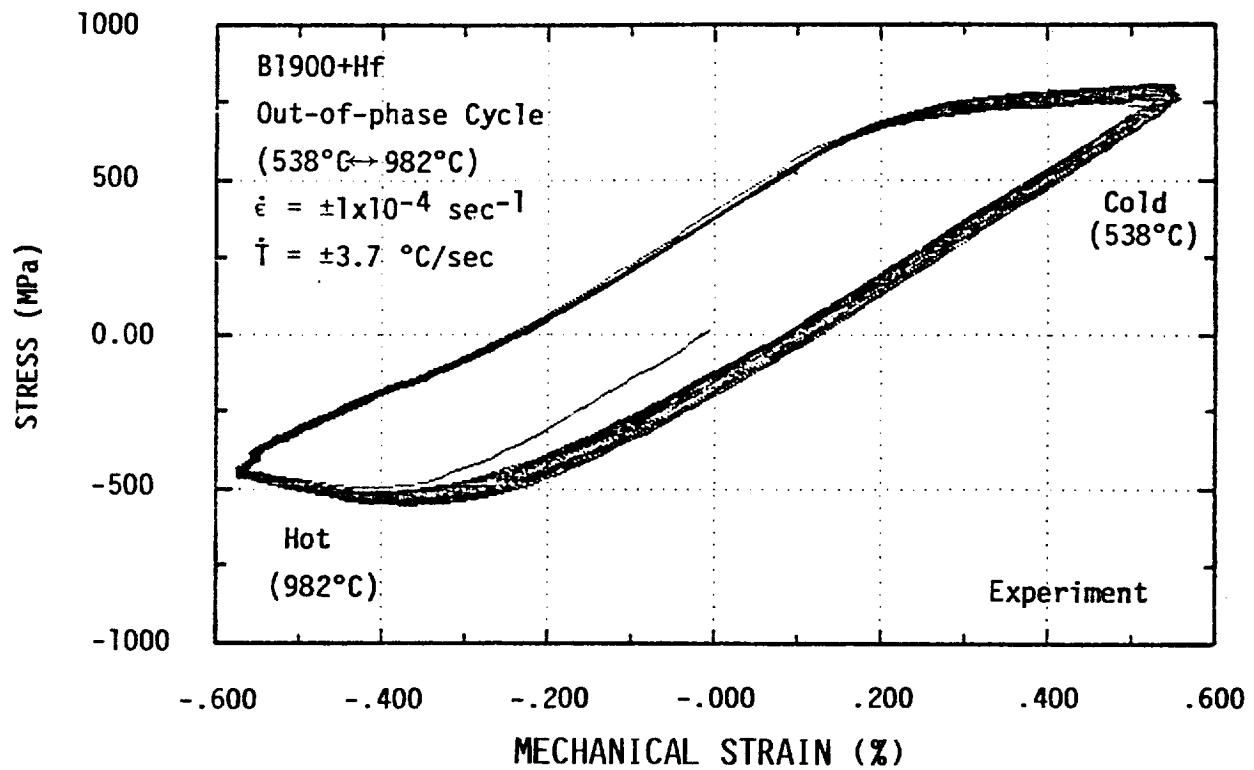


(a)

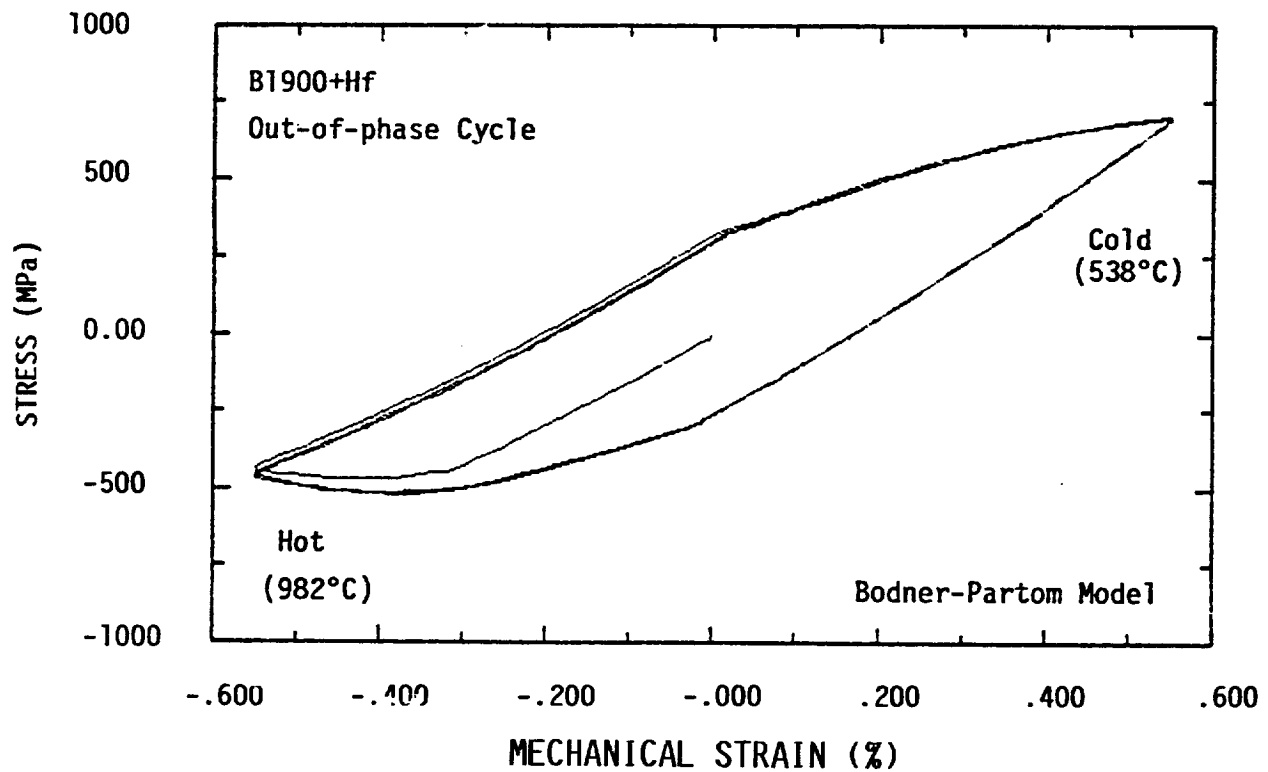


(b)

FIGURE 3.34 HYSTERESIS LOOPS OF B1900+Hf SUBJECTED TO OUT-OF-PHASE TMF LOADING IN THE 538 TO 982°C RANGE AND A MECHANICAL STRAIN RANGE OF $\pm 0.37\%$: (a) experiment, and (b) Bodner-Partom model calculation.



(a)



(b)

FIGURE 3.35 HYSTERESIS LOOPS OF B1900+Hf SUBJECTED TO OUT-OF-PHASE TMF LOADING IN THE 538 TO 982°C RANGE AND A MECHANICAL STRAIN RANGE OF $\pm 0.58\%$: (a) experiment, and (b) Bodner-Partom model calculation.

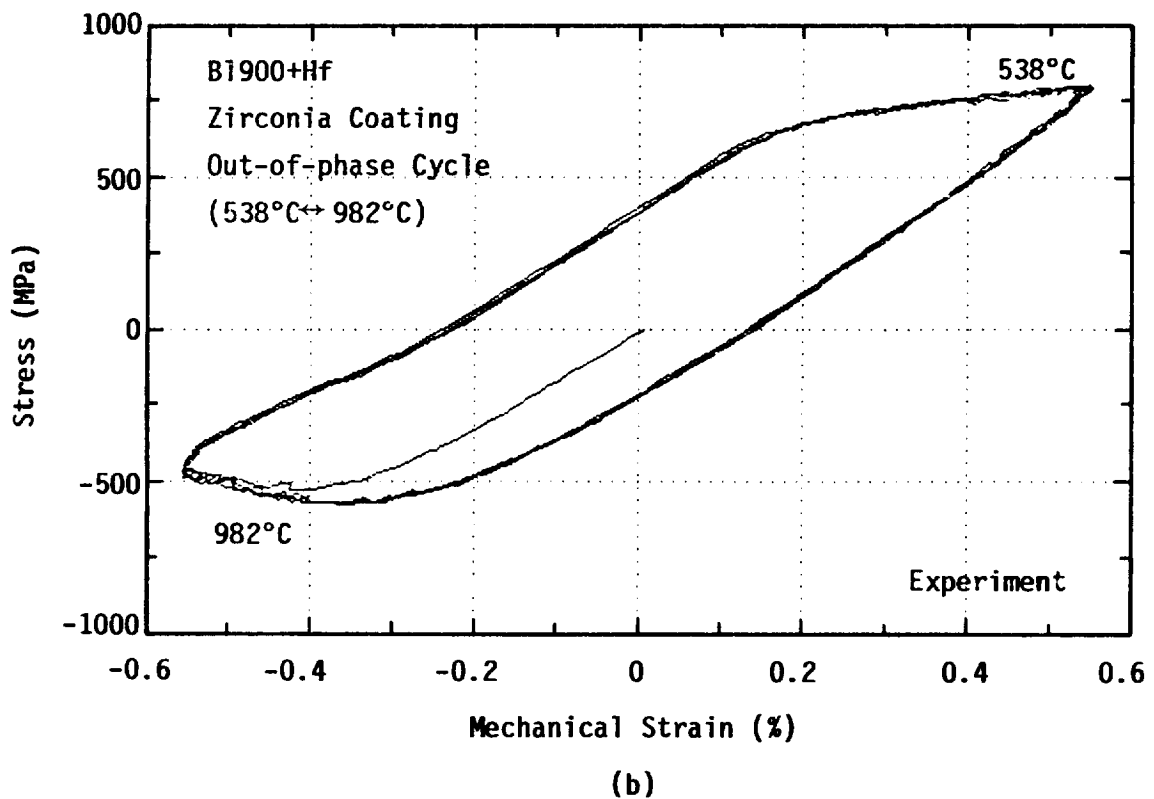
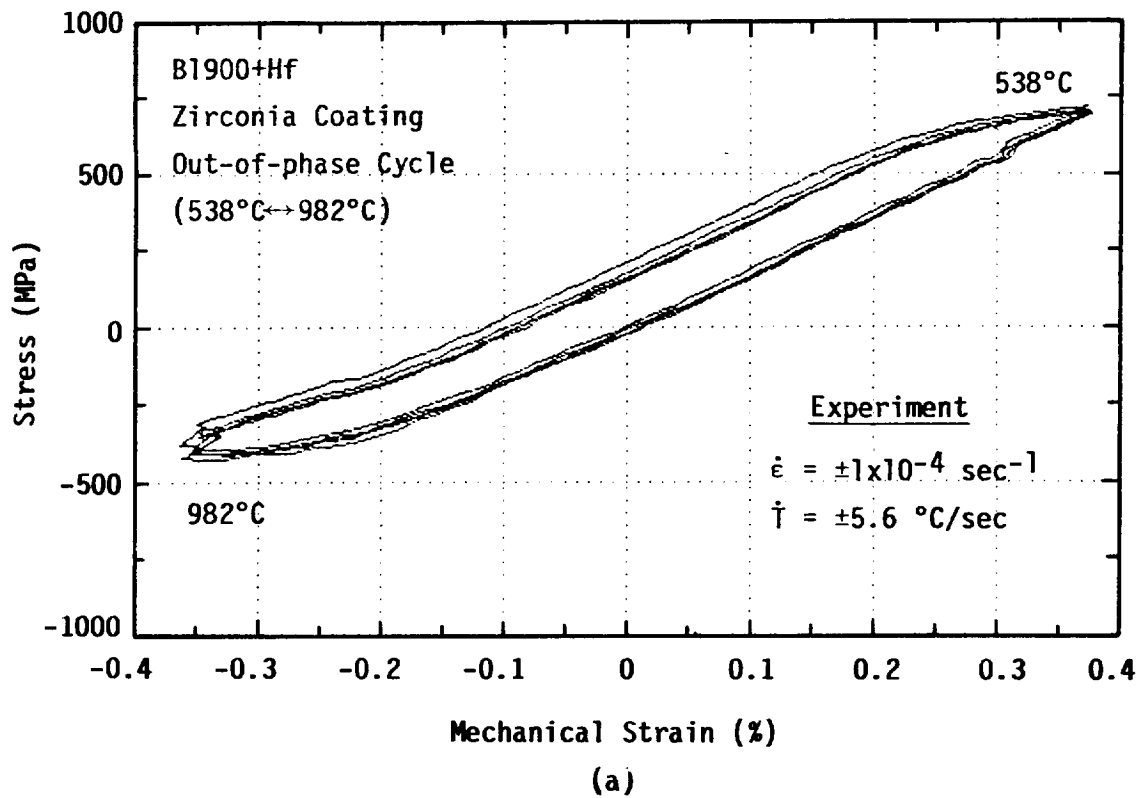


FIGURE 3.36 EXPERIMENTAL HYSTERESIS LOOPS OF B1900+Hf WITH YTTRIUM-STABILIZED ZIRCONIA COATING SUBJECTED TO OUT-OF-PHASE TMF LOADING IN THE 538 TO 982°C RANGE: (a) $\Delta\epsilon = \pm 0.4\%$, AND (b) $\Delta\epsilon = \pm 0.6\%$.

is identical to that of the uncoated specimen (Specimen 1D). In Figure 3.36, only the thickness of the metal substrate was used to compute the stress from the measured force. These results indicate that the ceramic coating did not support any loads under the imposed conditions.

Several interesting observations were made with regard to the coated specimen: (1) cold spots were observed during TMF testing, and (2) bulges of the ceramic coating were observed after the TMF test. The cold spots and bulges could be the result of coating delamination along the coating/substrate interface. Microcracks were also observed on the ceramic coating, as illustrated in Figure 3.37.

3.5 Microstructure, Deformation Modes and Dislocation Structure

Transmission electron microscopy (TEM) was performed on selected B1900+Hf specimens to determine the influence of load and thermal history on the deformation structure of the alloy. The objectives of these efforts were as follow: (1) to identify the deformation mechanisms responsible for possible thermal-history effects in the B1900+Hf material, (2) to identify microstructural changes, if any, associated with particular thermomechanical paths, and (3) to provide information for relating the unified constitutive approach to the underlying deformation mechanisms and dislocation structures. As discussed earlier, thermal-history effects in the inelastic deformation of metals have generally been attributed to strain aging and other microstructural influences. However, there is evidence in the literature which indicates that Ni_3Al exhibits anomalous deformation behavior in the intermediate temperature range (538–760°C) [16]. Since B1900+Hf contains approximately 60% ($\pm 5\%$) volume fraction of Ni_3Al , the possibility exists that thermal-history

ORIGINAL PAGE IS
OF POOR QUALITY

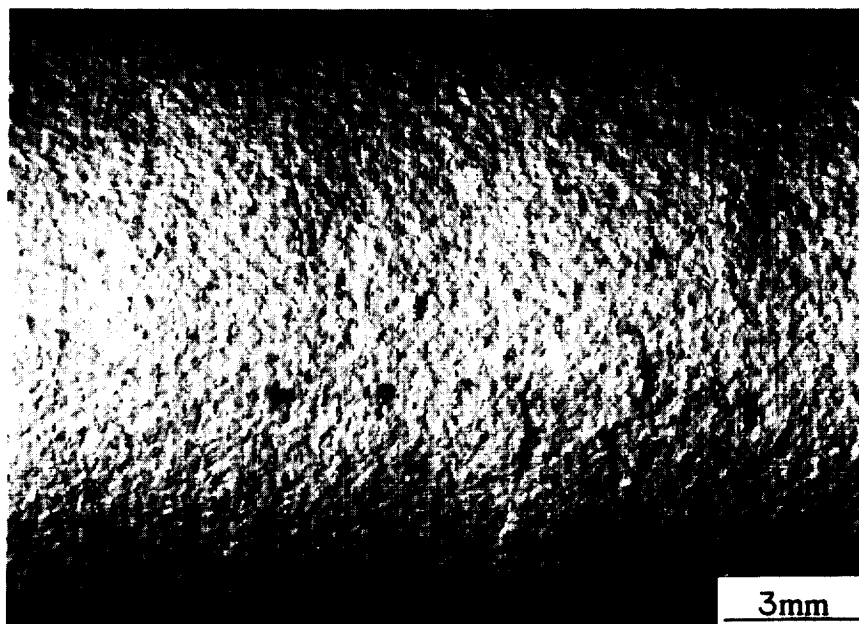


FIGURE 3.37 MICROCRACKS OBSERVED IN THE COATED B1900+Hf
SPECIMEN SUBJECTED TO AN OUT-OF-PHASE TMF
LOADING

effects in B1900+Hf could be caused by Ni_3Al rather than by strain aging or changes in the microstructure. The TEM efforts were therefore intended to provide results for testing various proposals concerning thermal-history effects in the plastic deformation of metals.

For the reason described above, the TEM efforts at SwRI were focused primarily on tests in which the specimens were deformed under nonisothermal conditions. In the companion Isotropic Life Prediction Contract, Moreno and his co-workers [24] at Pratt-Whitney Aircraft have examined the microstructure and the dislocation structures of the same B1900+Hf alloy deformed under isothermal conditions. In order to develop a more complete picture of the deformation behavior of B1900+Hf, important results from Moreno and associates for the isothermal B1900+Hf specimens will also be briefly reviewed. The results for the nonisothermally deformed specimens will then be presented and integrated with those of the isothermal specimens.

Preparation of the TEM foils from the deformed B1900+Hf specimens involved sectioning and mechanical polishing of the specimens into thin 3 mm diameter disks followed by electropolishing of the disks into thin foils. Final thinning of the disks was performed in a Fischione jet electropolisher with a solution of 300 ml methanol, 220 ml ethylene glycol, and 30 ml perchloric acid maintained at -38°C . Following thinning, the precipitate and dislocation structure of the foils were characterized in a Philips 301 transmission electron microscope.

3.5.1 Microstructure

As reported in a previous NASA report, the B1900+Hf material used in the present program was part of a single heat, designated W-0098, obtained

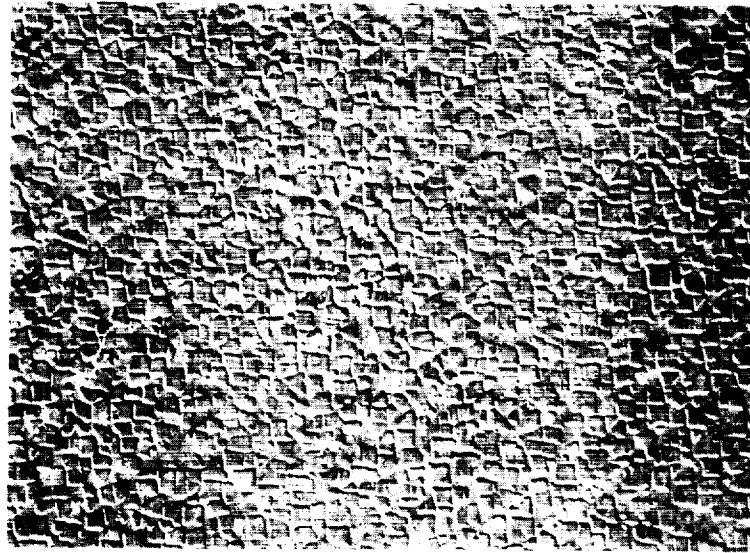
from Certified Alloy Products, Inc., Long Beach, California. The chemical composition, casting conditions, and heat-treatments of the B1900+Hf test bars were reported [2]. As indicated in the micrographs shown in Figure 3.38, the microstructure of B1900+Hf consists of mostly cuboidal γ' in a γ matrix. The γ' size is approximately 0.6 μm in the as-cast material and is 0.9 μm in the heat-treated condition. The volume fraction of γ' is approximately 60%.

Transmission electron microscopy performed at SwRI on deformed, nonisothermally tested B1900+Hf specimens has revealed three types of γ' morphologies, including cuboidal γ' , spaghetti (elongated) γ' , and spherical γ' of two different sizes which are shown in Figures 3.39(a), (b), and (c), respectively. These four types of γ' were observed in all of the nonisothermally deformed B1900+Hf specimens. They were all sheared by dislocations with the highest dislocation density being in the γ phase or at the γ/γ' interface. In most cases, the γ' morphology, as revealed by TEM replicas shown in Figure 3.38, was of the cuboidal form.

3.5.2 Dislocation Structures

3.5.2.1 Isothermal Specimens

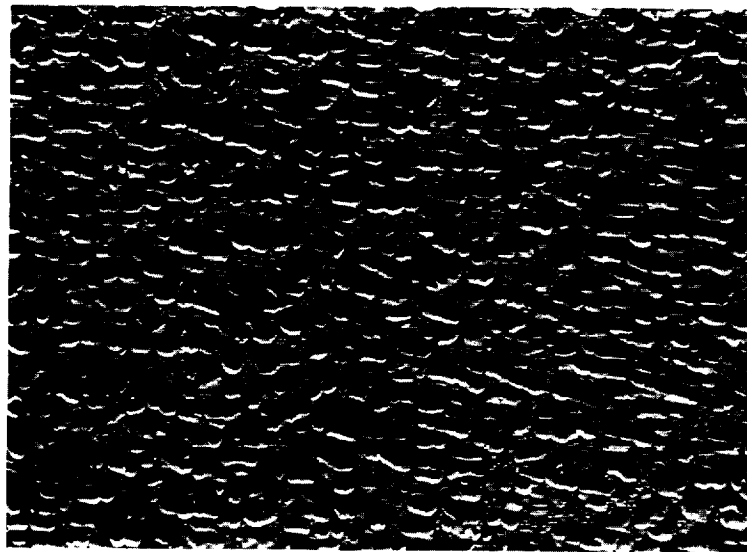
In the Fatigue Life Prediction Contract, Moreno and his co-workers [24] examined the dislocation structure in B1900+Hf specimens deformed under isothermal loading. With the permission of the NASA manager, Dr. G. Halford, for the Fatigue Life Contracts, the results of Moreno, et al. [24] are summarized in this section for the purposes of comparing them with the nonisothermal results. For tensile specimens deformed at 538-1093°C at a strain of 1-1.5%, the dislocations in B1900+Hf were found mostly in



As-Cast

$\gamma' = 0.6 \mu\text{m}$

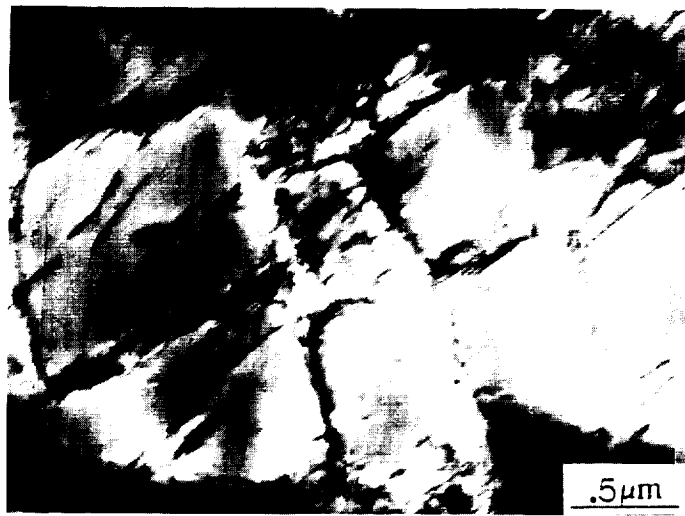
10 μm



Fully Heat Treated $\gamma' = 0.9 \mu\text{m}$

10 μm

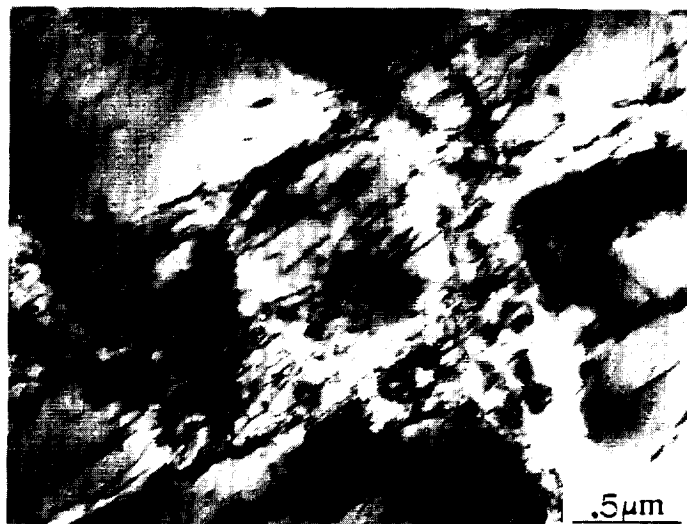
FIGURE 3.38 GAMMA PRIME (γ') SHOWS INCREASE WITH HEAT TREATMENT



(a)



(b)



(c)

ORIGINAL PAGE IS
OF POOR QUALITY

FIGURE 3.39 THE MORPHOLOGIES OF γ' OBSERVED IN DEFORMED B1900+Hf: (a) cuboidal γ' , (b) spaghetti γ' , (c) spheroidal γ' .

the γ phase and at the γ/γ' interface forming a cellular network around the γ' precipitates. Figure 3.40 shows that the dislocation network is very distinctive in specimens deformed at temperatures above 760°C, but is less distinctive at 538°C. In general, the dislocation density in the cellular network decreases with increasing test temperature which is probably due to static thermal recovery. Microtwins are also present in specimens tested at 760°C.

The dislocation structure found in isothermal creep specimens also consisted mostly of cellular networks surrounding the γ' . This is illustrated in Figures 3.41(a),(b), and (c) for creep specimens at (1) 982°C under a stress of 283 MPa for 4.1 hours, (2) at 871°C under a stress of 427 MPa for 20.6 hours, and (3) at 760°C under a stress of 600 MPa for 134.8 hours, respectively. The creep strain for these specimens was approximately 3%, and the reduction in area was 2.4-4.9%. Note also that dislocation segments are present in the γ' of these specimens. As in the tensile specimens, microtwins are observed in specimens subject to creep at 760°C.

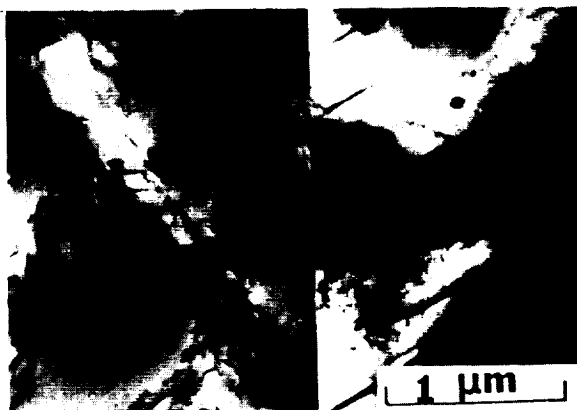
The dislocation structures of low-cycle fatigue specimens tested isothermally at 538 and at 871°C are shown in Figures 3.42 and 3.43, respectively. In both cases, the imposed strain ranges were 0.25%. The dislocation structures consist mostly of dislocation segments in γ and at the γ/γ' interface. Dislocation segments in γ' are also observed. Distinctive cellular dislocation networks, however, do not occur in these specimens primarily because the applied strain ranges are almost completely elastic.

3.5.2.2 Nonisothermal Specimens

Six specimens of B1900+Hf were selected for dislocation structure characterization in the present program, and their loading histories are



A



B



C



D



E

- A. 538°C, 1.5% Strain
- B. 760°C, 1.3% Strain
- 760°C, 4.5% Strain
- C. 871°C, 1.2% Strain
- D. 982°C, 1.2% Strain
- E. 1093°C, 1.0% Strain

TENSILE

FIGURE 3.40 COMPOSITE TEM PHOTOS OF TENSILE TESTED B1900+Hf SPECIMENS AT VARIOUS TEMPERATURES, FROM MORENO, et al. [23]

ORIGINAL PAGE IS
OF POOR QUALITY

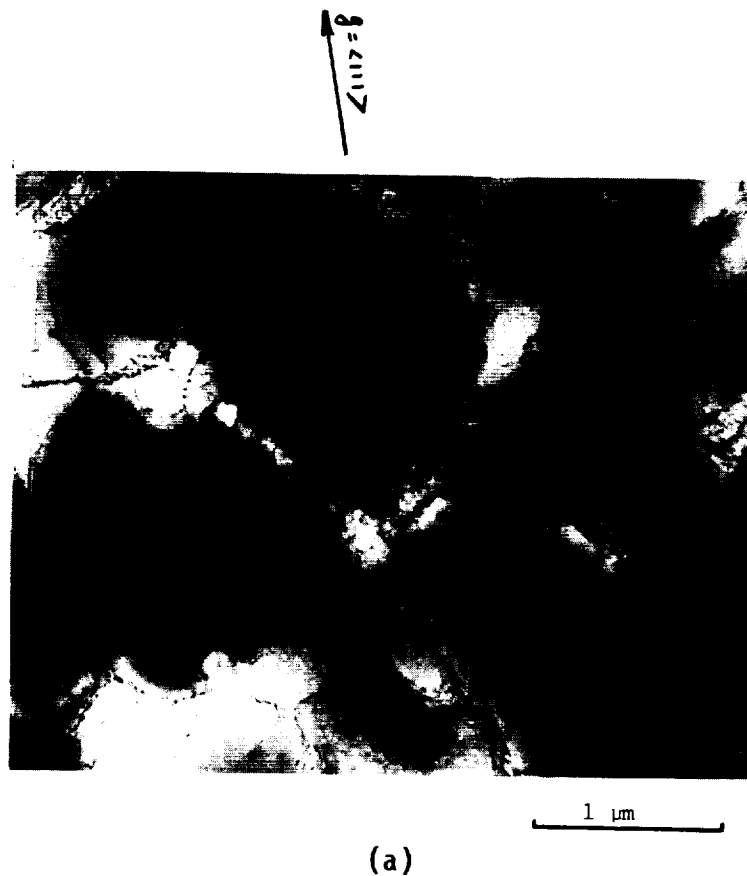


FIGURE 3.41 DISLOCATION NETWORKS OBSERVED IN ISOTHERMAL CREEP SPECIMENS OF B1900+Hf: (a) creep tested at 982°C/283 MPa for 4.1 hours; (b) creep tested at 871°C/427 MPa for 20.6 hours; and (c) creep tested at 760°C/600 MPa for 134.8 hours. Results are from Moreno, et al. [23]

ORIGINAL PAGE IS
OF POOR QUALITY

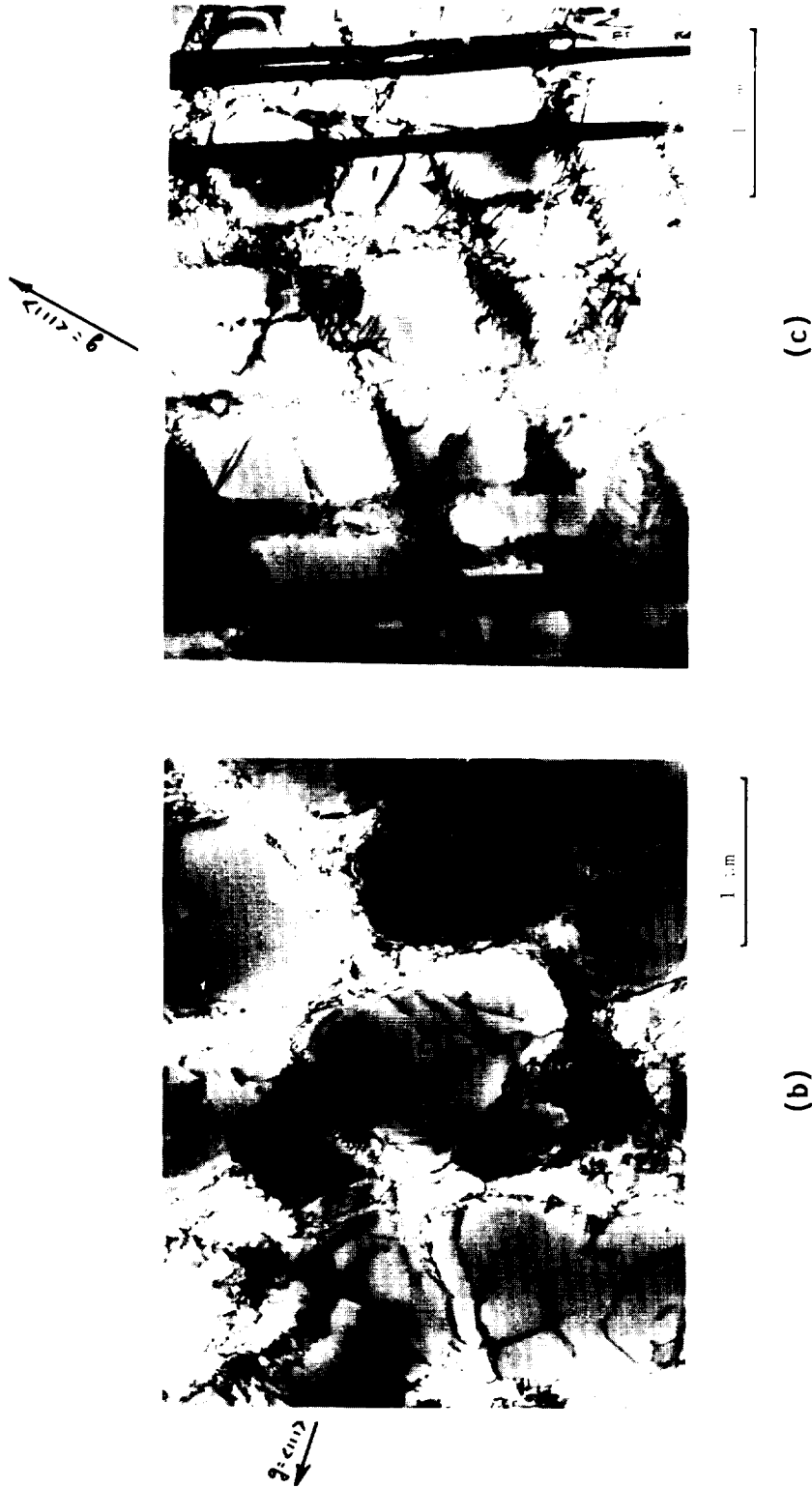


FIGURE 3.41 (CONTINUED) DISLOCATION NETWORKS OBSERVED IN ISOTHERMAL CREEP SPECIMENS OF B1900+Hf: (a) creep tested at 982°C/283 MPa for 4.1 hours; (b) creep tested at 871°C/427 MPa for 20.6 hours; and (c) creep tested at 760°C/600 MPa for 134.8 hours. Results are from Moreno, et al. [23]

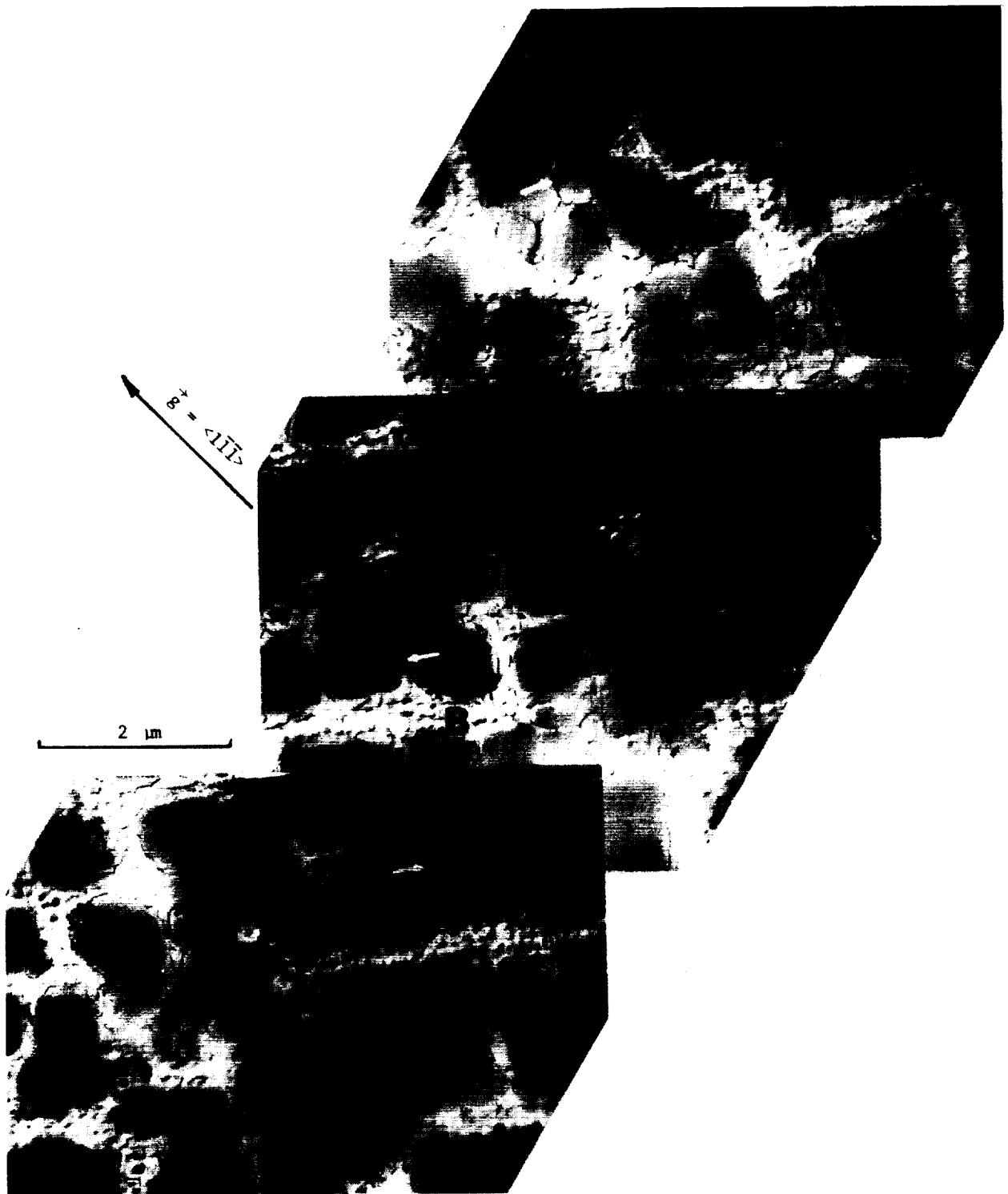


FIGURE 3.42 DISLOCATION STRUCTURES AFTER BEING LCF TESTED AT 538°C (1000°F), 10 cpm, $\Delta\epsilon = \pm 0.25\%$ FOR 12,500 CYCLES, FROM MORENO, ET AL. [23]



FIGURE 3.43 DISLOCATION STRUCTURE AFTER BEING LCF TESTED AT 871°C (1600°F), 10 cpm,
 $\Delta\epsilon = \pm 0.25\%$ FOR 2,965 CYCLES, FROM MORENO, ET AL. [23]

summarized in Table 3.4. One of these is an isothermal tensile specimen, three are nonisothermal tensile specimens, and the remaining two are thermomechanical fatigue specimens. These specimens were selected for the purpose of illustrating the effects of thermomechanical loading path on the dislocation structure. Figures 3.44-3.49 show the typical dislocation structures of the six specimens listed in Table 3.4. The main observations of the dislocation structures in the B1900+Hf specimens which are summarized in Table 3.5 are as follows: (1) there are extremely high dislocation densities in γ and at the γ/γ' interface in specimens (Specimens J3-1, K3, K9, and 1D) tested at the intermediate temperatures (538-760°C); (2) there are no large differences in the dislocation structures between the isothermal and nonisothermal tensile specimens except that there are more straight dislocations in the γ' of Specimen J3-1 than in Specimen K3; (3) the dislocation density is reduced in specimens exposed to temperatures $> 760^\circ\text{C}$ (Specimens K2 and 1E) because of thermal recovery; (4) straight dislocations are observed in γ' in Specimen 1D which was thermomechanically cycled between 538 and 760°C, while curved (wavy) dislocations are observed in Specimen 1E which was thermomechanically cycled between 538 and 982°C. It is also important to note that all specimens exhibited extremely dense dislocations in the γ and in the γ/γ' interface cellular networks surrounding the γ' which is consistent with the previous observations by Moreno, et al. Stacking faults were occasionally observed in B1900+Hf, but microtwins were not observed in any of the specimens tested.

The Burgers vectors of the straight and curved dislocations in the γ' of Specimens 1D and 1E were identified using the conventional two-beam extinction technique. In this technique, the two orientations of the \vec{g} vector

TABLE 3.4

**B1900+Hf SPECIMENS SELECTED FOR MICROSTRUCTURAL CHARACTERIZATION
USING TRANSMISSION ELECTRON MICROSCOPY**

<u>Specimen</u>	<u>Test Temp, °C</u>	<u>Strain History</u>	<u>Final Specimen Temp, °C</u>
J3-1	538	Tensile test	538
K2	760/982/760	Step temperature tensile test	764
K3	760/538	Step temperature tensile test	538
K9	538/760	Step temperature tensile test	740
1D	538 → 760	TMF	649
1E	538 → 982	TMF	649

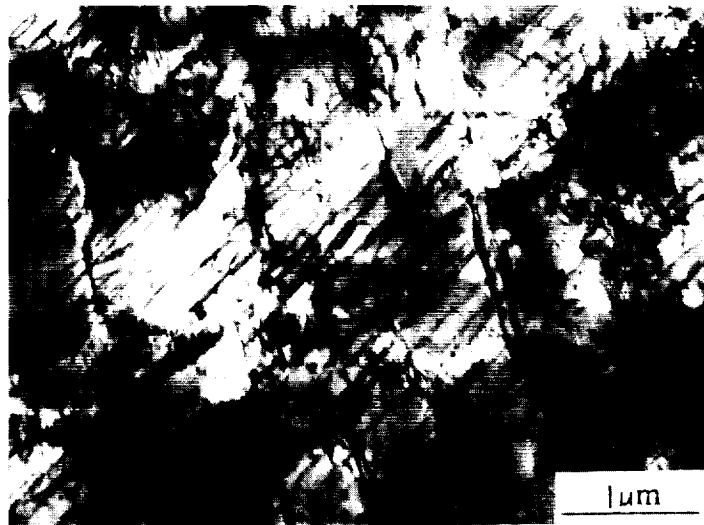


FIGURE 3.44 TEM MICROGRAPH OF SPECIMEN J3-1 SHOWING COMBINATION OF STRAIGHT AND WAVY DISLOCATION IN γ' AND EXTREMELY HIGH DISLOCATION DENSITY IN γ AND AT γ/γ' INTERFACE

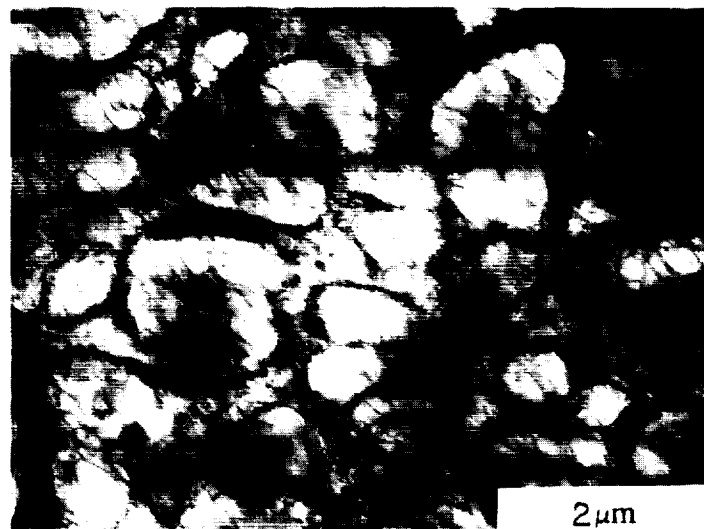
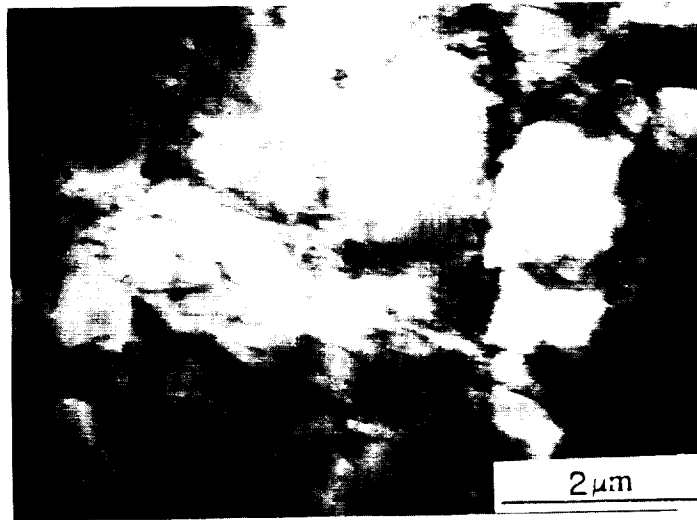


FIGURE 3.45 TEM MICROGRAPH OF SPECIMEN K2 SHOWING LOW DISLOCATION DENSITY IN γ , HIGH DISLOCATION DENSITY AT γ/γ' INTERFACE AND CURVED (WAVY) DISLOCATIONS IN γ'



ORIGINAL PAGE IS
OF POOR QUALITY

FIGURE 3.46 TEM MICROGRAPH OF SPECIMEN K3 SHOWING EXTREMELY HIGH DISLOCATION DENSITY IN γ AND AT γ/γ' INTERFACE, AND RELATIVELY LOW DENSITY OF STRAIGHT AND WAVY DISLOCATIONS IN γ'



FIGURE 3.47 TEM MICROGRAPH OF SPECIMEN K9 SHOWING SIMILAR DISLOCATION STRUCTURES AS IN SPECIMEN K3



FIGURE 3.48 TEM MICROGRAPH OF SPECIMEN 1D SHOWING EXTREMELY HIGH DISLOCATION DENSITY IN γ AND AT γ/γ' INTERFACE, AND HIGH DENSITY OF STRAIGHT DISLOCATIONS IN γ'

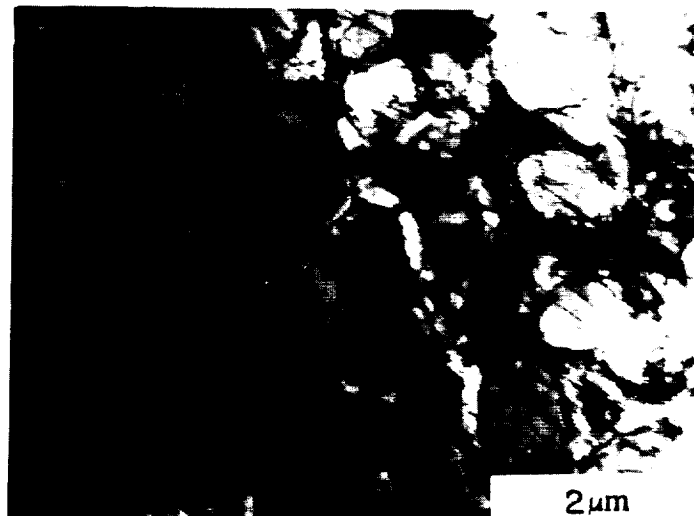


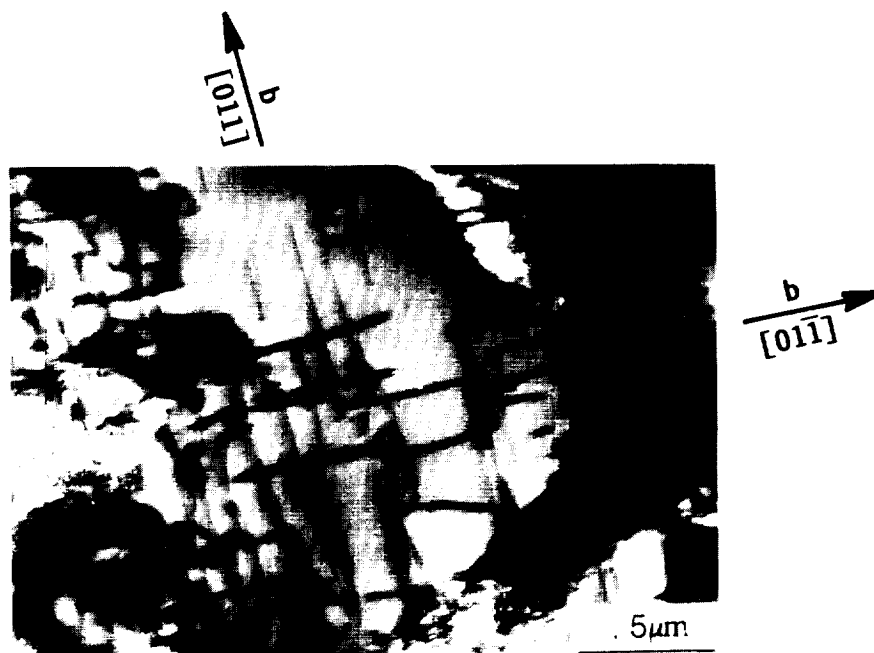
FIGURE 3.49 TEM MICROGRAPH OF SPECIMEN 1E SHOWING HIGH DISLOCATION AT γ/γ' INTERFACE, LOW DISLOCATION DENSITY IN SOME γ , AND RELATIVELY LOW DENSITY OF CURVED DISLOCATIONS IN γ'

TABLE 3.5
A SUMMARY OF DISLOCATION STRUCTURES IN B1900-Hf SPECIMENS TESTED
UNDER NONISOTHERMAL OR TMF CONDITIONS

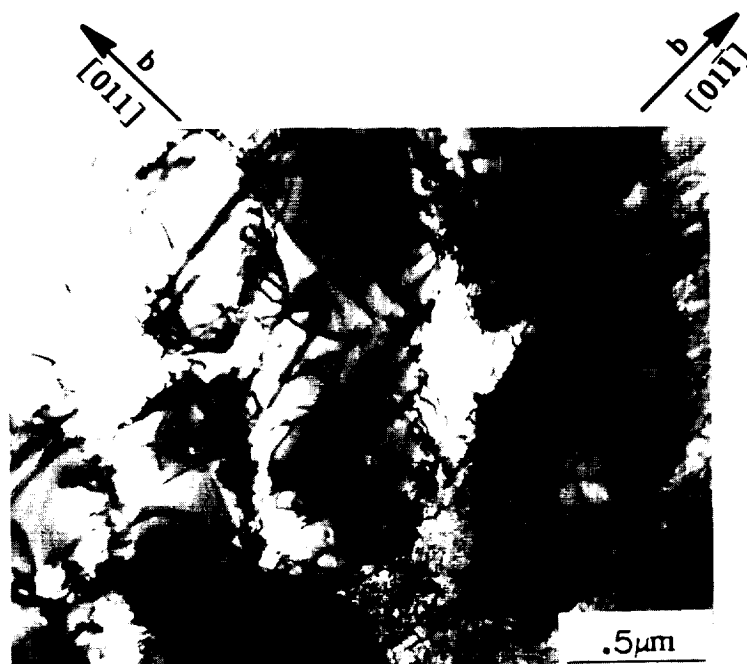
Specimen	Dislocation Structure			Comments
	γ	γ'	γ	
J3-1	Extremely high dislocation density	Intermediate to low density of straight and wavy dislocations		Straight dislocations have $\langle 101 \rangle$ Burgers Vector
K2	Relatively low dislocation density in γ ; high dislocation density at γ/γ'	Low dislocation density; dislocations are mostly curved (wavy)		dislocation density in γ is reduced by thermal recovery (at 982°C)
K3	Extremely high dislocation density in γ and at γ/γ' interface	Intermediate density of straight and wavy dislocations; cuboidal γ' , spaghetti γ' , and spherical γ' are all sheared by dislocation		γ' morphology does not affect the dislocation structure
K9	Extremely high dislocation density in γ and at γ/γ' interface	Intermediate to low dislocation density; combination of straight and curved dislocations		Dislocation structure is similar to Specimen K3
1D	Extremely high dislocation density; presence of planar slip bands	High dislocation density; dislocations are straight, presence of planar slip bands		Two types of slip in γ' ; probably (111) slip and cross slip on (010) planes
1E	Extremely high dislocation density in some areas while low in others; high density at γ/γ' interface; planar slip bands	Intermediate density; mostly curly dislocations		Thermal recovery (at 982°C) reduce the dislocation density in γ

(the diffraction vector) for which the dislocations became extinct were located, and the Burgers vector \vec{b} of the dislocations was obtained from the cross product of the two diffraction vectors based on the principle that $\vec{g} \cdot \vec{b} = 0$. Figure 3.50(a) shows that the Burgers vector for the straight dislocations in Specimen 1D is of the $\langle 101 \rangle$ type. These are screw dislocations, i.e., the dislocation lines are aligned parallel to the Burgers vector. On the other hand, the curved dislocations exhibited in Specimen 1E, shown in Figure 3.50(b), were found to be of mixed character having both edge and screw components since the dislocation lines are neither normal nor parallel to the Burgers vector.

An extensive review of dislocation structures in Ni_3Al in either single crystal form or in γ/γ' alloys has been presented by Pope and Ezz [16]. Comparing the present results with those summarized by Pope and Ezz [16], it appears that the straight dislocations observed in Specimen 1D are probably sessile $\langle 101 \rangle$ (010) dislocations which are formed as the result of cross slip from the (111) to the (010) planes. Since these dislocations are immobile, they are barriers to subsequent dislocations either on the (111) planes or on the (010) planes. In principle, this hardening mechanism can be operative in tension, compression or cyclic loading of specimens at the intermediate temperature regime (538-760°C), but appears to be somewhat more pronounced under thermomechanical loading as reflected by the greater amount of straight dislocations observed in Specimen 1D. The anomalous hardening observed in TMF cycling in the 538-760°C shown in Figures 3.31 and 3.33 for Specimens 1B and 1D is probably the result of the interactions of mobile dislocations with the sessile (010) dislocations.



(a)



(b)

FIGURE 3.50 DISLOCATIONS IN THE γ' OF TMF SPECIMEN TESTED AT: (a) 538-760°C (Specimen 1D), and (b) 538-982°C (Specimen 1E). The straight dislocations in Specimen 1D exhibit screw character, while those in Specimen 1E show mixed character.

ORIGINAL PAGE IS
OF POOR QUALITY

The above hypothesis is supported by experimental observations made on Specimen 1E. In particular, it was observed that removal of the sessile, straight screw dislocations in γ' by increasing the hot end of the TMF cycle to 982°C results in the elimination of the anomalous hardening. It is well-known that the rapid decrease in strength (critical resolved shear stress) of Ni_3Al and of γ/γ' alloys at temperatures above 871-982°C has generally been attributed to the activation of (010) slip [25]. At these elevated temperatures, the critical resolved shear stress for the (010) plane is lower and thermal recovery is more prominent than in the intermediate temperature regime (538-760°C). The higher test temperature in Specimen 1E is believed to lower the critical resolved shear stress for (010) slip so that the dislocations on that plane are mobile and more favored than those on the (111) plane. Any sessile $\langle 101 \rangle$ (010) dislocations that are produced at the cold end of the TMF cycle could become mobile at the hot end (982°C) of the TMF cycle thereby reducing the amount of straight screw dislocations that are observed. Without these sessile dislocations in γ' , there would be no additional barrier to dislocation motion and therefore no anomalous hardening.

Intense shear bands were also observed in Specimens 1D and 1E. As shown in Figure 3.51(a) and 3.51(b), these shear bands consist of narrow bands of material containing an extremely high density of dislocations which extend across both the γ and γ' phases. The slip bands were oriented on the [110] directions and were composed primarily of $\frac{a}{2}$ [110] edge dislocations. Occasionally, slip bands were observed that contained dislocations of mixed or primarily screw character, as shown in Figure 3.51(c). Observed only in the TMF specimens which have been cycled at $\pm 6\%$ for several cycles, these shear bands were probably formed as the result of the breakdown of the dislocation

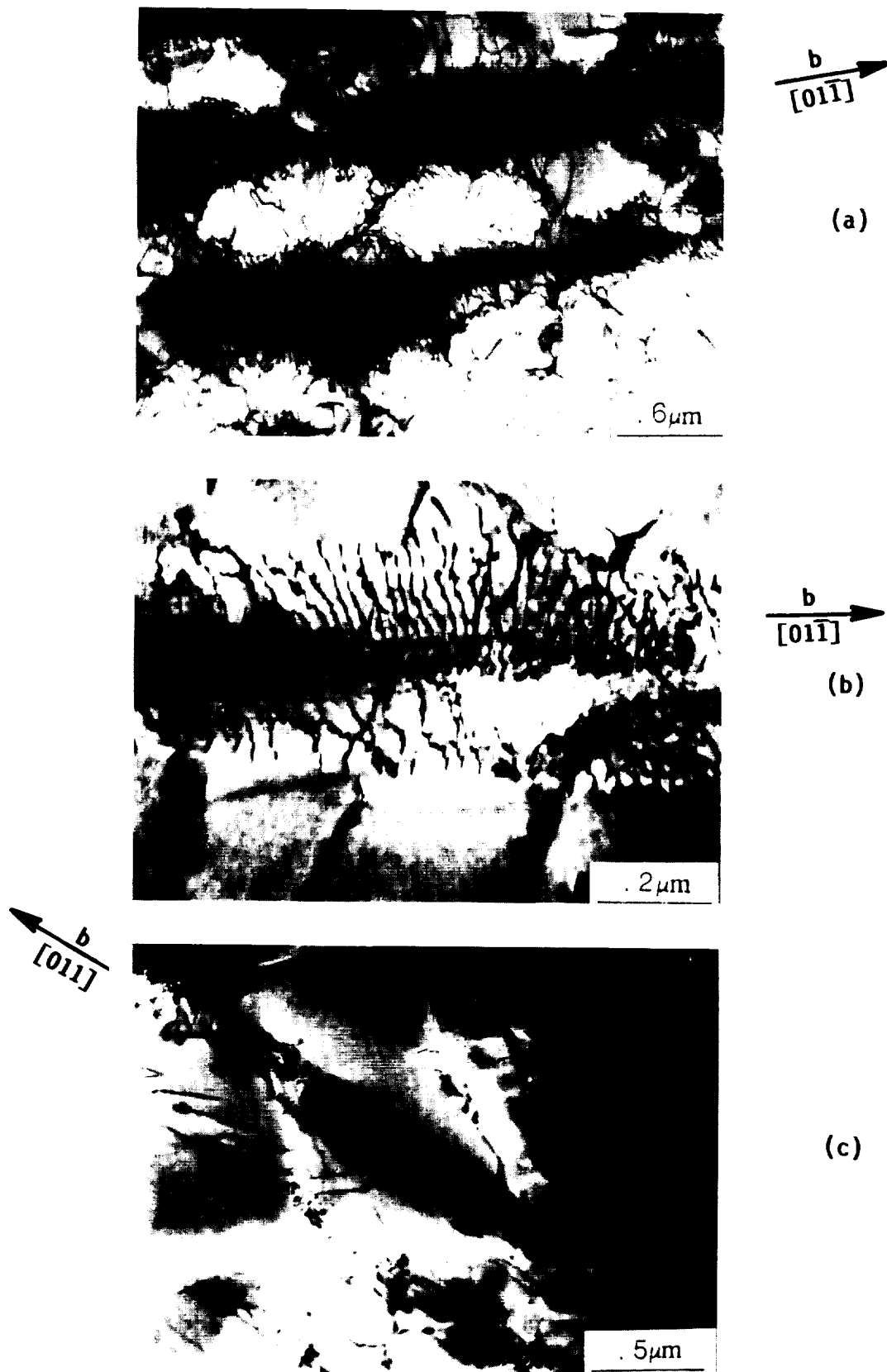


FIGURE 3.51 INTENSE SHEAR BANDS OBSERVED IN SPECIMEN 1E ARE COMPRISED PRIMARILY OF EDGE DISLOCATIONS (a and b), AND A SHEAR BAND IN SPECIMEN 1D, WHICH IS COMPRISED OF MIXED DISLOCATIONS (c)

ORIGINAL PAGE IS
OF POOR QUALITY

cellular structure due to strain cycling. They are likely to lead to fatigue crack formation, since they tend to concentrate the plastic strain.

3.5.3 Relation of Microstructural Examinations and Unified Constitutive Theories

One of the important observations of the dislocation arrangements in isothermally, as well as in nonisothermally deformed B1900+Hf specimens, is the formation of cellular dislocation networks around the γ' precipitates. That fewer dislocations are observed within the γ' can be rationalized on the basis that the phase ordered structure of γ' requires dislocations within it to occur as pairs separated by an anti-phase boundary of relatively high energy [16]. To minimize the total energy associated with the dislocation, dislocations which shear the γ' are stored and rearranged in the γ and at the γ/γ' interface into a cellular network. Such dislocation cell structures appear to form at relatively low strain levels (a few percent) and appear to be the stable configuration for specimens tested under different loading paths including isothermal tensile, isothermal creep, nonisothermal tensile, and TMF loading. The theoretical implication is that the saturation stress concept postulated in many unified constitutive models can be considered to be the flow stress associated with the saturated dislocation configuration, i.e., the stress required to move dislocations to and from the walls of the dislocation cellular network. Since the saturated dislocation structure is independent of the thermomechanical loading path, the saturation stress and the limiting values of the internal hardening variables should therefore be independent of the thermomechanical loading path. The values of the saturation stress should, however, depend on temperature and strain rate indicating the dependence of the critical resolved shear stress on these quantities.

The dislocation structure in specimens which have not reached the saturated state condition depends on their previous deformation history, and can be quite different in appearance from that of the saturated configuration. For example, the dislocation structures associated with strain cycling at low strain levels in Figures 3.42 and 3.43 consist mainly of dislocation segments in γ' without a very distinctive cellular dislocation network in γ and at the γ/γ' interface. It appears that the dislocation structure evolves with plastic deformation from a low density state to a saturated state with increasing inelastic strain or plastic work. The evolution equations for the hardening variable that are used in the unified approach are continuum representations of the evolution of dislocation structures in the deformed metals. The rate of hardening corresponds on the rate of dislocation interaction and rearrangement into cellular structures. For B1900+Hf and Mar-M247, the saturated configurations can be attained at a few percent strain.

The rearrangement of dislocations into cellular structures implicitly suggests a dynamic recovery process since it is a means to reduce the interaction energy between dislocations. The observation that the cellular structure can be attained at low temperature without the benefit of thermal recovery clearly indicates the presence of a deformation-induced recovery process. The use of dynamic recovery terms in the evolution equations for the hardening variables, leading to saturation conditions, is thereby justified.

The experimental evidence also shows that thermal recovery reduces the dislocation density in the cellular structure. The static thermal recovery terms in the hardening equations are the continuum representations of this process. At elevated temperature, steady-state is controlled by the balance of the hardening and static thermal recovery terms. Consequently, the

high temperature steady-state structure can be different from the saturated structure. In B1900+Hf, this difference is manifested as a reduction in the dislocation density in the cellular structure. In the unified models, it is represented by the fact that the steady-state values of the hardening variables (isotropic and directional hardening) are generally lower than their respective limiting values due to the presence of the static thermal recovery terms.

The cell size of the dislocation configuration tends to decrease with stress in many metals. For B1900+Hf and possibly other strengthened alloys, the dislocation network is formed as the result of storing dislocations in γ and at the γ/γ' interface. The size of the dislocation cell structure appears to be controlled by the γ' size and is relatively independent of the stress level. This effect can be seen by comparing the dislocation cell size associated with the cuboidal γ' with those of the spaghetti γ' , with the latter being larger because of the larger spaghetti γ' size.

Thermal history effects in inelastic deformation are generally considered to be induced by strain aging or other microstructural influences [8,9,18]. For the B1900+Hf and Mar-M247 materials studied in the present program, there are no indications that strain aging plays an important role in the constitutive response of these alloys under thermomechanical loading. There are, however, some indications that interactions of dislocations in the ordered γ' phase might be somewhat dependent on the thermomechanical loading path. This may be due to the forming of sessile (010) screw dislocation in γ' which can occur only at the immediate temperature regime and is most pronounced under thermomechanical loading. Even under those conditions, this additional "anomalous" hardening effect is relatively minor compared to

conventional hardening due to γ' and dislocation cell walls. Ignoring the effects of the sessile (010) dislocations in the Bodner-Partom model has not been found to introduce any significant errors in the predicted TMF calculations.

Based on these micromechanical considerations, it is fair to conclude that the basic framework of the unified approach appears to be adequate for the class of materials studied in this program. In particular, the use of one kinetic equation for describing all aspects of inelastic flow, including plastic deformation, creep, and stress relaxation is fundamentally valid and supported by the dislocation structures observed on the deformed specimens. The general form of evolution equations for the hardening variables is also consistent with the various features of the dislocation configurations. For materials with stable microstructures, it does not appear that the hardening mechanisms under isothermal loading conditions are significantly different from those under nonisothermal loading conditions. It is therefore not necessary to introduce additional hardening terms into the evolution equations to account for thermal history effects other than those representing the variation of material constants with temperature.

3.6 Discussion of Thermal History Effects

The conclusion obtained here that nonisothermal behavior can be predicted on the basis of isothermal data is different from those of other investigations [8-10,26]. It is therefore of interest to compare and discuss the present findings with those of Pelloux and Marchand [26] and of Robinson and associates [8-10]. In a recent report [26], Pelloux and co-workers examined the thermomechanical cyclic stress-strain response of B1900+Hf in the

temperature range from 400 to 925°C. By comparing the values of the stress range as a function of the strain amplitude for the TMF cycles with the isothermal strain cycles, they observed differences in the hardening behavior and concluded that it was difficult to predict the cyclic stress-strain behavior under TMF conditions from isothermal data. Their conclusion was directed mainly to the observation that the stress-strain responses of B1900+Hf under TMF cycling were different from those under isothermal conditions. Those differences arose because they compared the cyclic response characteristic of B1900+Hf subjected to very different thermomechanical loading histories. Since inelastic deformation is history dependent, it is therefore not surprising that a different response was observed for the different deformation paths; such differences of cyclic response were also observed in the present result. Our contention is that it is possible to obtain material constants in a unified model using only isothermal data and to apply the model for thermomechanical loading conditions. Without such a model, comparison of stress-strain responses of different thermomechanical histories is not meaningful.

In a series of papers [8-10], Robinson and associates expressed the view that inelastic deformation under nonisothermal loading conditions cannot be predicted based only on isothermal data. In particular, they reported experimental data of step temperature cyclic tests of Hastelloy-X, which showed that the stress response associated with strain cycling at 424°C after initial cycling at 649°C was different from the isothermal response at 424°C. On the other hand, the stress response associated with step temperature cycling from 427°C to 649°C was in good agreement with the isothermal data. The latter behavior was observed in the step temperature cyclic tests of the B1900+Hf

material in this program. The lack of agreement between the isothermal and nonisothermal data of Hastelloy-X subjected to strain cycling with temperature changes from 649°C to 424°C was attributed to dynamic strain aging [8-10], which was recently confirmed by Miner, et al [27]. Since dynamic strain aging is not a factor in the B1900+Hf and MAR-M247 materials, the conclusions reached in the present program do not contradict those of Robinson. More recent work by Bartolotta and Ellis [28] on the Hastelloy X under isothermal and thermomechanical cycling suggests some correlation is possible between isothermal and nonisothermal cyclic response. Based on our experience and that of Robinson and co-workers, it is fair to conclude that isothermal data are sufficient for evaluating all the model constants in the unified models for materials which do not exhibit strong dynamic strain aging, plasticity-induced precipitation, or large microstructural changes in the temperature range of interest. The question of whether isothermal data is sufficient for evaluating all the model constants in a unified model for materials which exhibit concurrent plasticity-induced precipitation (e.g., 316 stainless steels and the Hastelloy-X alloy) remains open. Further work is required in this area.

4.0 APPLICATION OF CONSTITUTIVE MODEL TO AN ALTERNATE MATERIAL (TASK L)

The application of the Bodner-Partom model to the alternate material, Mar-M247, was conducted in three phases. In Task L1, the minimum number of monotonic tensile, creep, and isothermal cyclic constitutive tests (both uniaxial and biaxial) was conducted to generate a data base for determining the model constants. Task L1 was completed last year, while Tasks L2 and L3 were completed this year. In Task L2, three cyclic thermomechanical tests were performed using the same test parameters that were employed in Task K for the base material. The applicability of the Bodner-Partom model was demonstrated for Mar-M247 in Task L3 by performing computations for the thermomechanical test cycles.

For these tasks, a total of twenty (20) Mar-M247 specimens were fabricated. Fourteen (14) specimens were used for isothermal tension, creep, and cyclic strain tests; three (3) specimens were used for isothermal biaxial tests and three (3) specimens for the TMF tests.

4.1 Experiments

4.1.1 Isothermal Tensile, Creep, and Cyclic Testing

Tensile tests with strain rate jumps were conducted for Mar-M247 using the procedures described in [6]. The tensile tests involved extending the specimen at an initial strain rate, $\dot{\epsilon}_i$, to a prescribed 2% strain level (corresponding to the saturation stress level). After reaching the prescribed strain, four changes of strain rate were imposed. The tensile test matrix for Mar-M247 is shown in Table 4.1. In addition, isothermal cyclic and creep tests were performed for Mar-M247. As indicated in the test matrix, the

TABLE 4.1

ISOTHERMAL TENSILE, CYCLIC AND CREEP TEST
MATRICES FOR Mar-M247

	23	648	Temperatures, °C		982	1093
			760	871		
Mar-M247	X	X	X	X	X	X

$$\dot{\epsilon}_1 = 1 \times 10^{-4} \text{ sec}^{-1}, \dot{\epsilon}_2 = 1 \times 10^{-6} \text{ sec}^{-1}, \dot{\epsilon}_3 = 1 \times 10^{-5} \text{ sec}^{-1},$$

$$\dot{\epsilon}_4 = 1 \times 10^{-4} \text{ sec}^{-1}, \dot{\epsilon}_5 = 1 \times 10^{-3} \text{ sec}^{-1}$$

CYCLIC TEST MATRIX FOR Mar-M247

Temperature, °C	$\dot{\epsilon}_1 \text{ sec}^{-1}$	$\Delta\epsilon_1 = \pm .25\%$	$\Delta\epsilon_2 = \pm .4\%$	$\Delta\epsilon_3 = \pm .6\%$
23	5×10^{-4}	X	X	X
648	5×10^{-4}	X	X	X
871	5×10^{-4}	X	X	X
982	5×10^{-5}	X	X	X
1093	5×10^{-5}	X	X	X

CREEP TEST MATRIX FOR Mar-M247

Temperature, °C	σ
871	600 MPa
982	300 MPa
1093	150 MPa

cyclic tests were conducted at three strain range levels (0.25%, 0.4% and 0.6%) and at five temperatures (23, 648, 871, 982, and 1093°C). Only three creep tests were performed under conditions listed in Table 4.1.

The biaxial deformation behavior of Mar-M247 was examined using three nonproportional strain cycles. The first strain cycle was conducted at 648°C and contained the strain history sequence: (1) 90° out-of-phase combined tension-torsion, (2) in-phase combined tension-torsion, (3) fully reversed torsion, and (4) fully reversed tension. The strain sequence was conducted under strain-controlled condition and was repeated on the same specimen at two effective strain ranges ($\pm 0.4\%$ and $\pm 0.6\%$). The second nonproportional strain cycle was identical to the first one, but was performed at 982°C. The third strain cycle was a combined tension-torsion cycle conducted under 90° out-of-phase condition with strain hold at each of the strain peaks. The test temperature was 982°C, and the imposed effective strain range was $\pm 0.4\%$.

4.1.2 Nonisothermal Tensile and TMF Testing

Two nonisothermal (step temperature) tensile tests were performed on the Mar-M247 specimens. In one case, the specimen was pulled at 760°C at $\dot{\epsilon} = 1 \times 10^{-4} \text{ sec}^{-1}$ until a strain of $\approx 1.0\%$ was reached. The test temperature was then changed to 649°C. Straining at 649°C was continued until a strain of $\approx 2\%$ was reached. The test temperature was then changed back to 760°C. All the temperature change was done while straining at $\dot{\epsilon} = 1 \times 10^{-4} \text{ sec}^{-1}$. The other nonisothermal tensile test was performed in a similar manner, but the applied temperature sequence was 649°C and 760°C. An out-of-phase thermo-mechanical cycle identical to that of Specimen 1E (see Table 3.3) was also

performed for Mar-M247. The temperature range for the TMF cycle was 538-982°C, and the imposed mechanical strain ranges were $\pm 0.4\%$ and $\pm 0.6\%$ at a rate of $\pm 1 \times 10^{-4} \text{ sec}^{-1}$.

4.2 Correlation of Model and Experiment

Comparisons of calculations based on the Bodner-Partom model and experimental results were presented for isothermal tensile, creep, and cyclic tests of Mar-M247 in the annual report [6] of last year (1986). For completeness, some of these comparisons are summarized here together with the nonisothermal test results obtained recently. The same set of material constants, which were determined from isothermal tensile and creep data shown in Table 4.2, was used for all the isothermal and nonisothermal calculations. The temperature dependence of material constants with temperature are shown in Table 4.3. The procedures for obtaining the material constants were described in Ref. [6]. Determination of the essential constants at the lower temperatures (23-648°C) was not possible since strain aging effects obscured the normal strain rate dependence of the flow stress. As a consequence, the value of Z_1 obtained at the higher temperatures was assumed to be constant, and the associated value of n at the lower temperatures was obtained from the saturated flow stress.

Correlation of model and experimental tensile stress-strain curves for six test temperatures at $\dot{\epsilon} = 1 \times 10^{-4} \text{ sec}^{-1}$ is shown in Figure 4.1. The unusual temperature behavior at the lower temperature appears to be due to strain aging effects which were directly incorporated in the hardening constants. This procedure can be done for a single strain rate but does not demonstrate the influence of strain aging on the applicable strain rate

TABLE 4.2

BODNER-PARTOM MODEL CONSTANTS FOR Mar-M247

Temperature - Independent Constants

$$m_1 = .1 \text{ MPa}^{-1}$$

$$\alpha_1 = 0.0$$

$$Z_1 = 1.64 \times 10^4 \text{ MPa}$$

$$r_1 = r_2 = 3$$

$$D_0 = 1 \times 10^4 \text{ sec}^{-1}$$

Temperature - Dependent Constants

Constants	Temperature, °C					
	<u>23</u>	<u>648</u>	<u>760</u>	<u>871</u>	<u>982</u>	<u>1093</u>
n	.556	.556	.556	.522	.467	.415
$m_2 \text{ (MPa}^{-1}\text{)}$	1.35	.47	.47	1.35	1.35	1.35
$Z_0 \text{ (MPa)}$	1.6×10^4	1.6×10^4	1.6×10^4	1.3×10^4	1.2×10^4	1.05×10^4
$Z_2 \text{ (MPa)}$	1.6×10^4	1.6×10^4	1.6×10^4	1.3×10^4	1.2×10^4	1.05×10^4
$Z_3 \text{ (MPa)}$	5×10^3	5×10^3	8.63×10^3	8.63×10^3	8.63×10^3	8.63×10^3
$A_1 = A_2 \text{ (sec}^{-1}\text{)}$	0	0	0	2×10^{-2}	.25	2
E (MPa)	1.9×10^5	1.61×10^5	1.71×10^5	1.49×10^5	1.29×10^5	9.7×10^4

TABLE 4.3
TEMPERATURE DEPENDENCE OF THE BODNER-PARTOM MODEL CONSTANTS
FOR Mar-M247

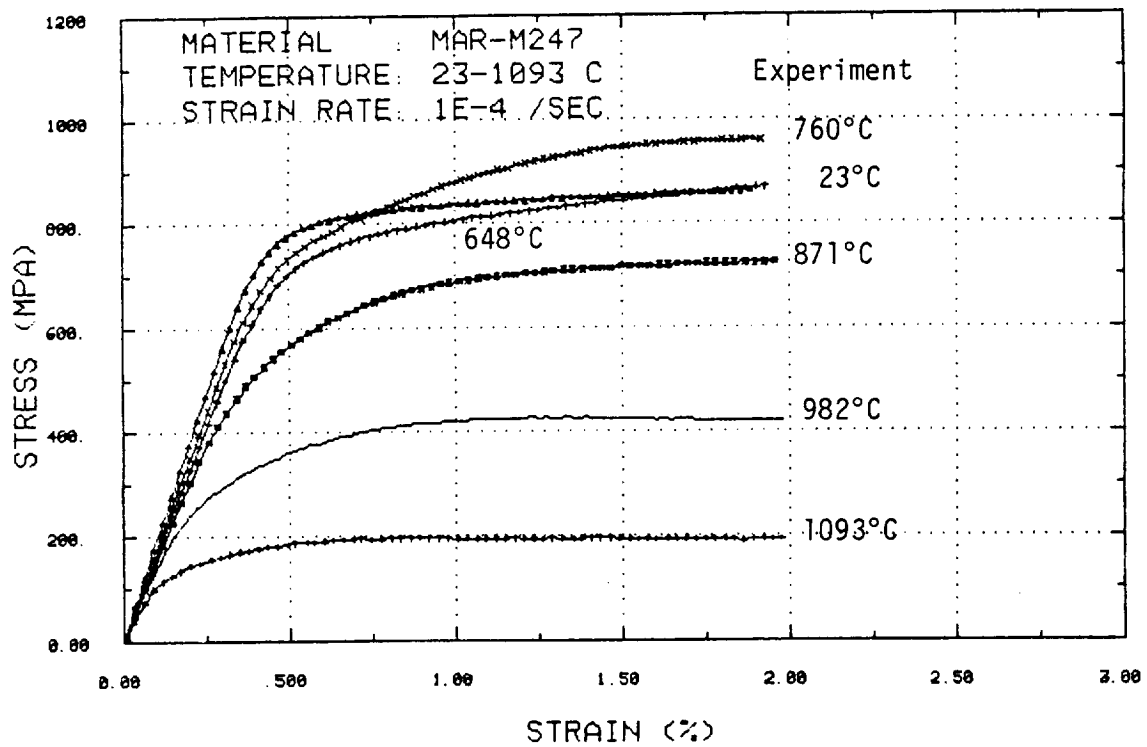
$$n = .556 \quad T \leq 823^{\circ}\text{C}$$

$$n = -.1575 + \frac{781.95}{T+273} \quad 823^{\circ}\text{C} \leq T \leq 1093^{\circ}\text{C}$$

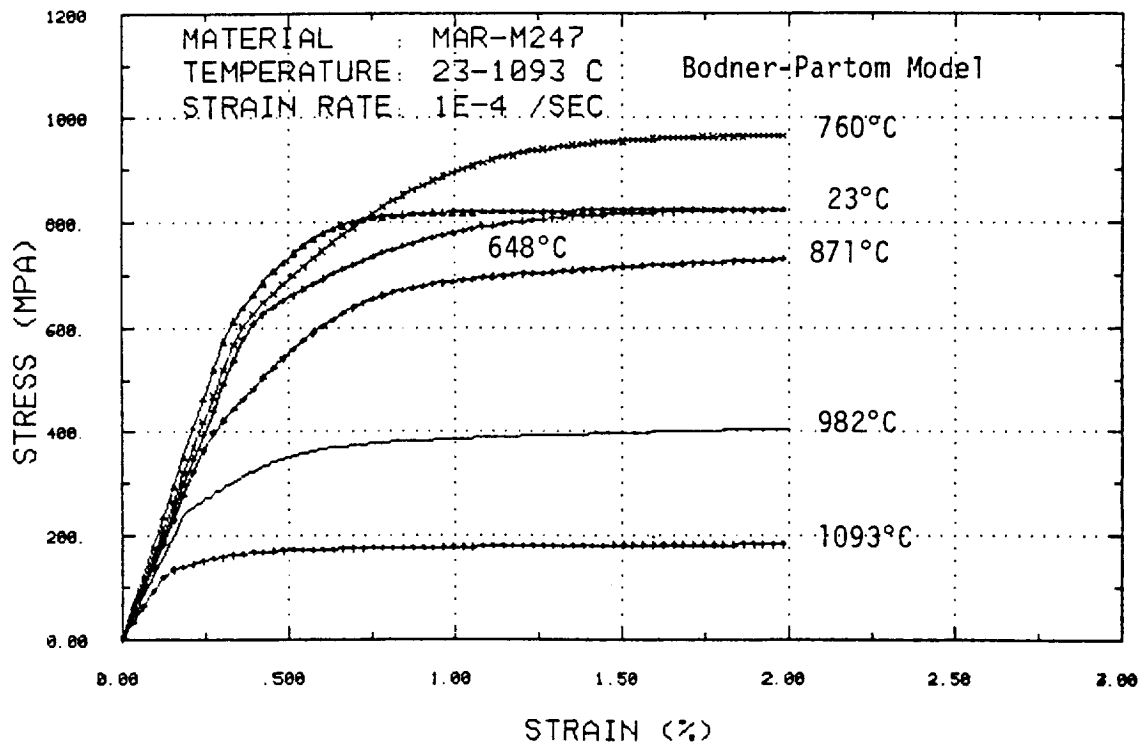
$$Z_0 = Z_2 = 1.6 \times 10^4 \text{ MPa} \quad T \leq 760^{\circ}\text{C}$$

$$Z_0 = Z_2 = -6.5617 \times 10^3 + \frac{2.3305 \times 10^7}{T+273} \text{ MPa} \quad 760^{\circ}\text{C} \leq T \leq 1093^{\circ}\text{C}$$

$$A_1 = A_2 = 3.3064 \times 10^{10} \exp \left[- \frac{3.214 \times 10^4}{T+273} \right] \text{ sec}^{-1} \quad T \leq 1093^{\circ}\text{C}$$



(a)



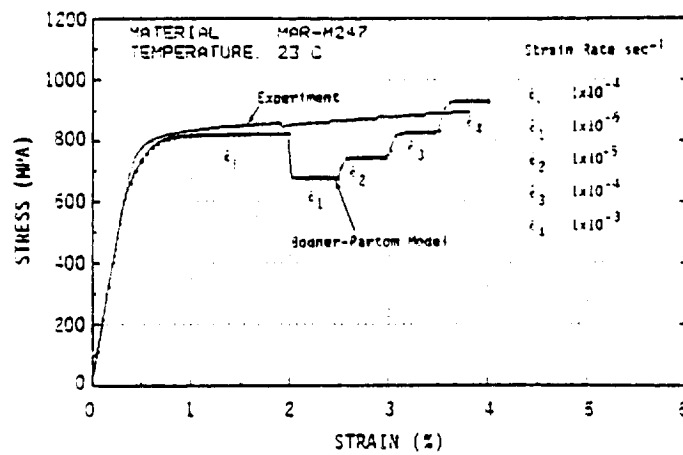
(b)

FIGURE 4.1 CORRELATION OF THE BODNER-PARTOM MODEL WITH EXPERIMENTAL TENSILE CURVES AT SIX TEMPERATURES: (a) EXPERIMENT, AND (b) MODEL CALCULATIONS.

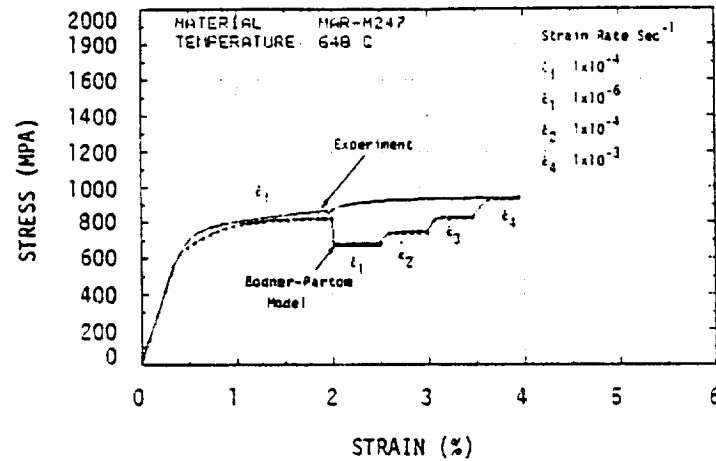
sensitivity. As a consequence, the proper strain rate sensitivity in the presence of strain aging would not be indicated. Figures 4.2(a), (b), (c), (d), (e), and (f) show comparisons of model calculations and experimental results for the stress-strain response under variable strain rate conditions at 23, 648, 760, 871, 982, and 1093°C, respectively. The poor correlations of the predicted strain rate dependence of the flow stress with the test results at 23 and 648°C are due to strain aging effects which are currently not included in the model. Comparison of model and experimental creep curves under an applied stress of 60 MPa at 871°C is presented in Figure 4.3. For cyclic loading, the Bodner-Partom model predicts the stress range at a given imposed strain range reasonably well, but the calculated hysteresis loops are slightly overly squared, as demonstrated in Figure 4.4.

Correlations of model and experiment for biaxial loading under nonproportional 90° out-of-phase tension-torsion strain cycling at 648°C are shown in Figure 4.5. The imposed effective strain range is $\pm 0.4\%$. As shown in Figure 4.5, the $\sigma-\sqrt{3}\tau$ loci at 648°C are predicted by the model, but individual hysteresis loops are larger than those experimentally observed. A comparison of model prediction and experimental data for 90° out-of-phase tension-torsion strain cycling with strain hold at the strain peaks is shown in Figure 4.6. In this case, the model also slightly overpredicts the tension/compression stress range and the width of the associated hysteresis loop.

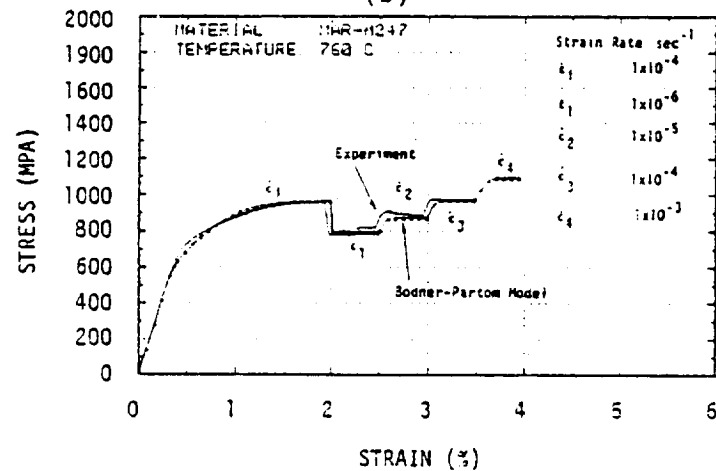
Figure 4.7 shows the nonisothermal tensile test result for the case in which the specimen was pulled initially at 760°C. The test temperature was then reduced to 649°C at a cooling rate of 4.4 °C/sec after the mechanical strain reached $\approx .75\%$. The test temperature reached 649°C at a mechanical



(a)



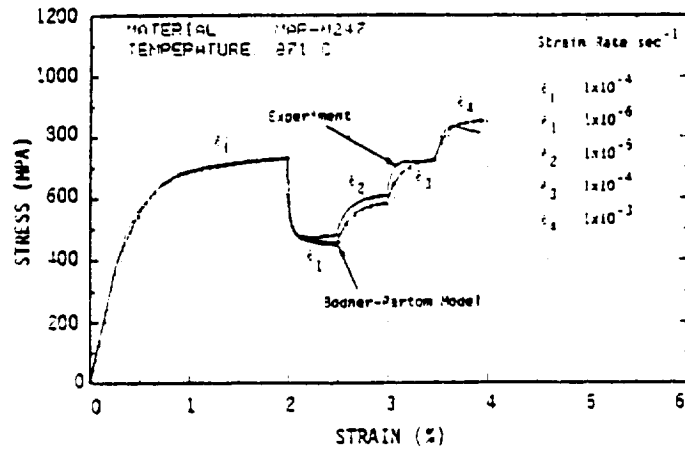
(b)



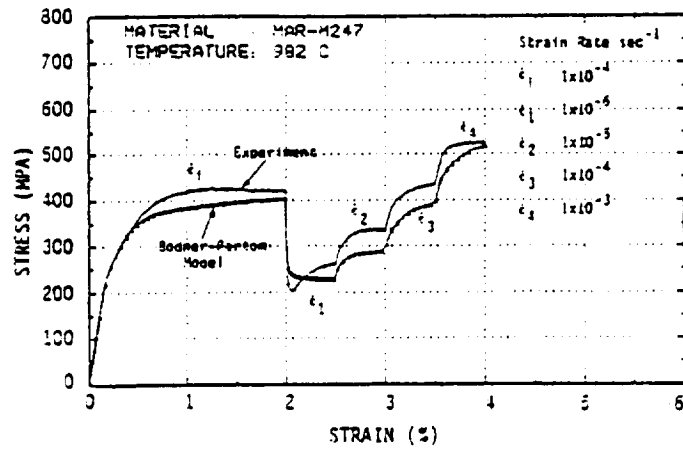
(c)

FIGURE 4.2 COMPARISONS OF MODEL CALCULATION AND EXPERIMENT FOR TENSILE TEST WITH STRAIN RATE CHANGES: (a) 23°C, (b) 648°C, and (c) 760°C.

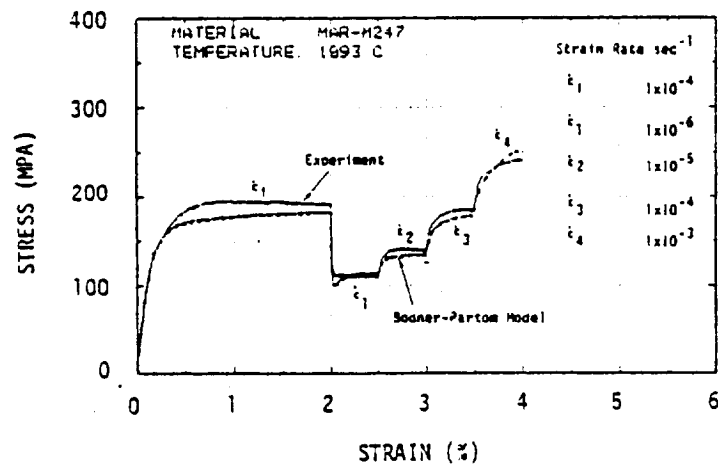
ORIGINAL PAGE IS
OF POOR QUALITY



(d)



(e)



(f)

FIGURE 4.2 (Continued) COMPARISONS OF MODEL CALCULATION AND EXPERIMENT FOR TENSILE TEST WITH STRAIN RATE CHANGES: (d) 871°C, (e) 982°C, and (f) 1093°C.

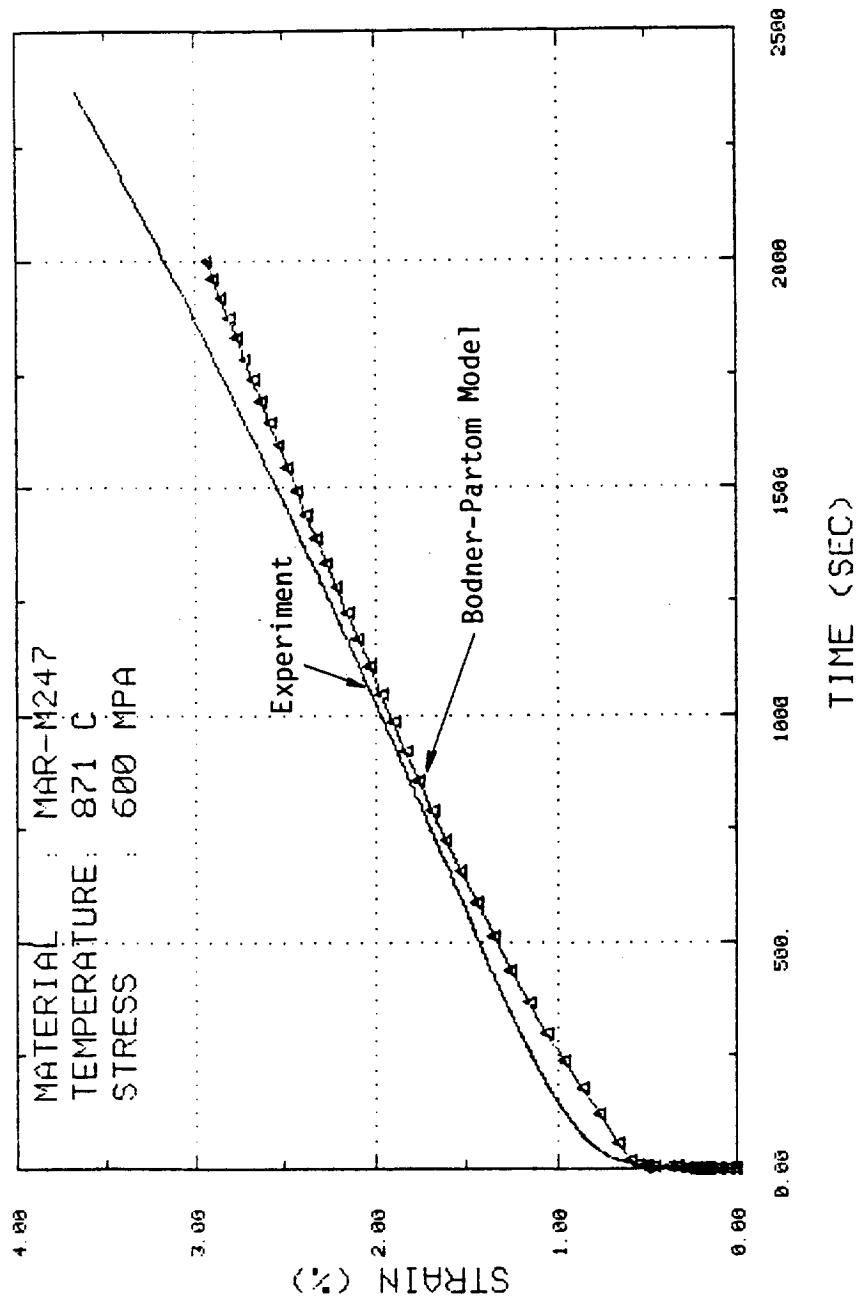
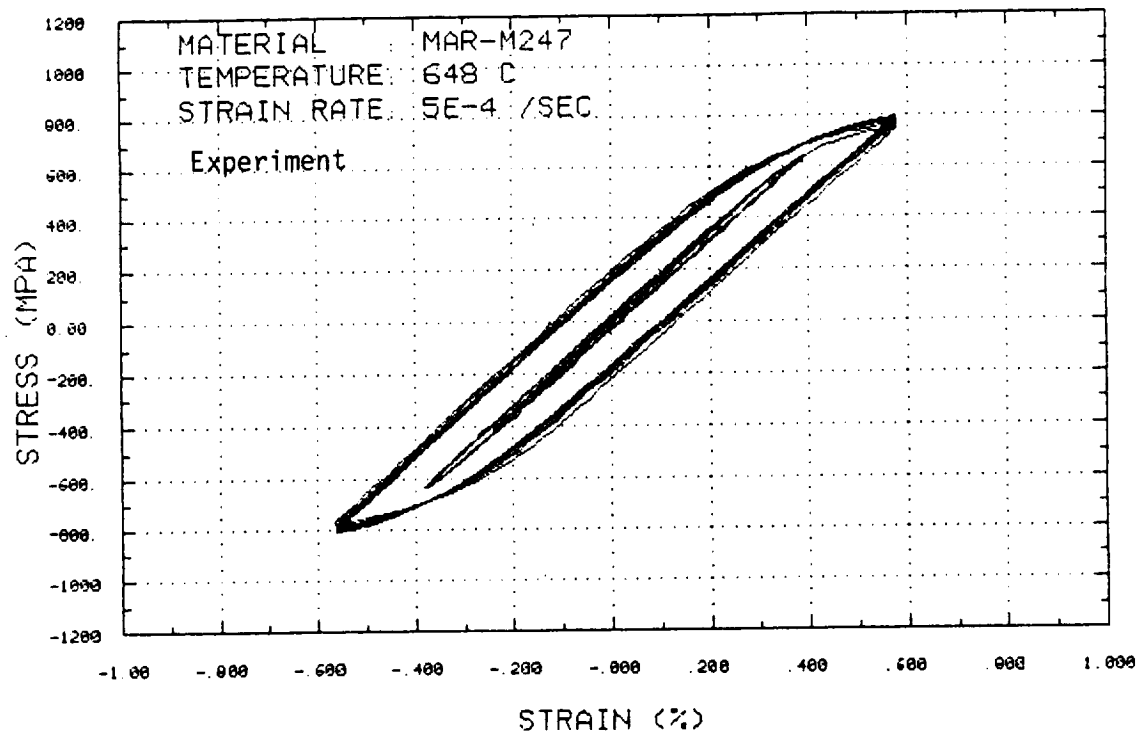
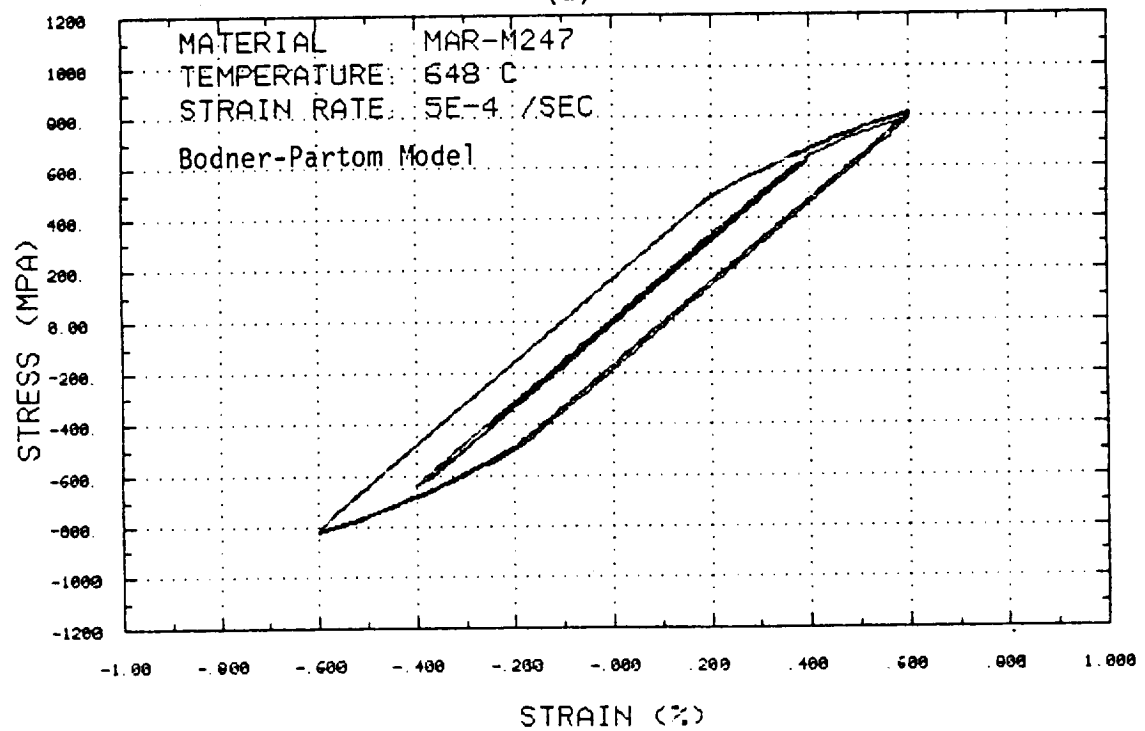


FIGURE 4.3 CREEP CURVE OF Mar-M247 AT 871°C UNDER AN APPLIED STRESS OF 600 MPa.



(a)



(b)

FIGURE 4.4 COMPARISON OF MODEL CALCULATION AND EXPERIMENTAL CYCLIC DATA AT 648°C. The cyclic test was conducted under fully reversed condition at strain ranges of $\pm 0.25\%$, $\pm 0.4\%$, and $\pm 0.6\%$: (a) experiment, and (b) Bodner-Partom Model.

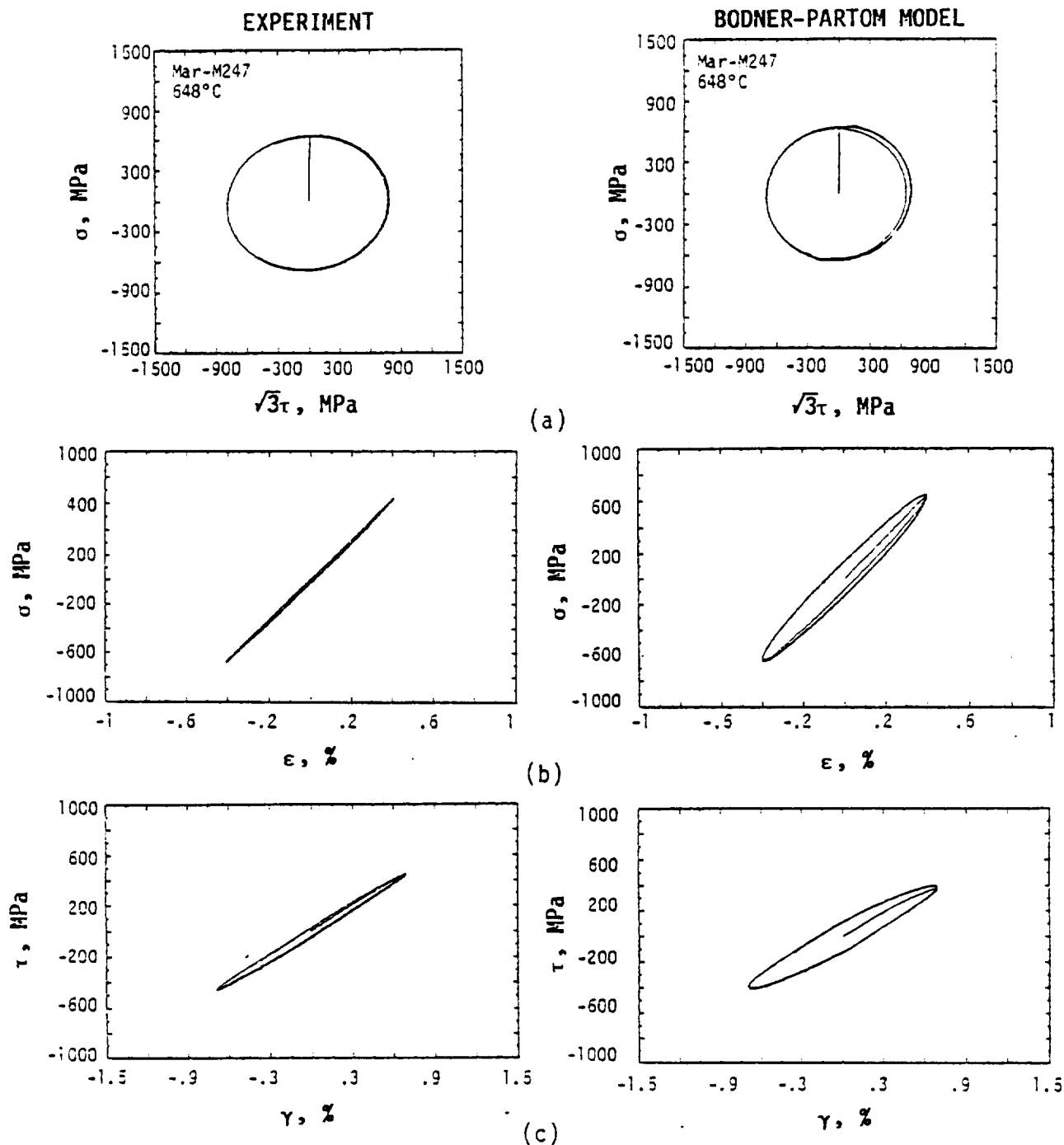


FIGURE 4.5 COMPARISON OF MODEL CALCULATION AND EXPERIMENT FOR Mar-M247 UNDER 90° OUT-OF-PHASE STRAIN CYCLING AT 648°C. The effective strain and strain rate are +.4% and $4 \times 10^{-4} \text{ sec}^{-1}$: (a) σ - τ plot, (b) σ - ϵ plot, and (c) τ - γ plot.

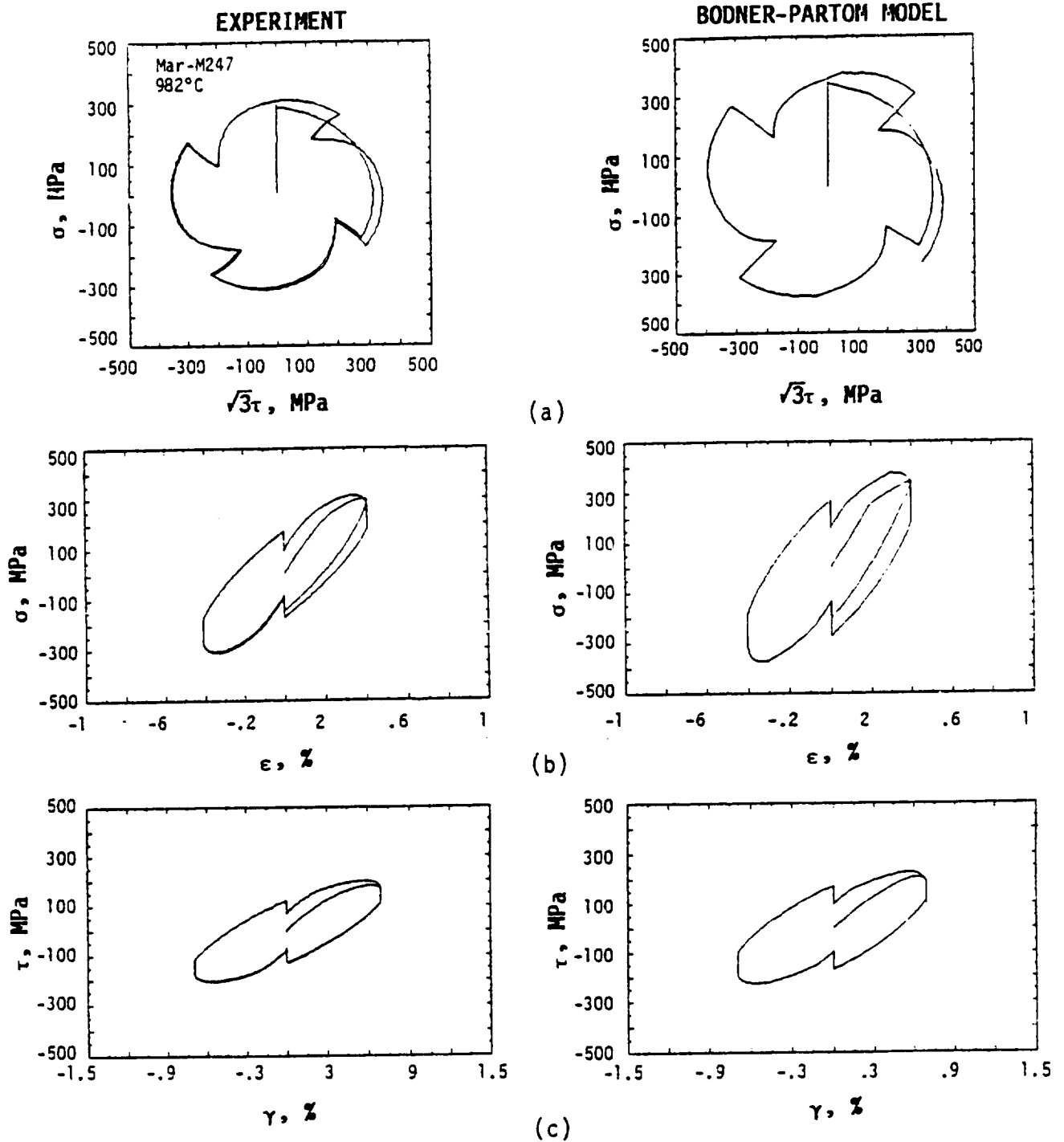


FIGURE 4.6 COMPARISON OF MODEL CALCULATION AND EXPERIMENT FOR Mar-M247 UNDER 90° OUT-OF-PHASE STRAIN CYCLING AT 982°C WITH STRAIN HOLD AT EACH OF THE STRAIN PEAKS. The effective strain and strain rate are $\pm 4 \times 10^{-4} \text{ sec}^{-1}$: (a) σ - τ plot (b) σ - ϵ plot and (c) τ - γ plot.

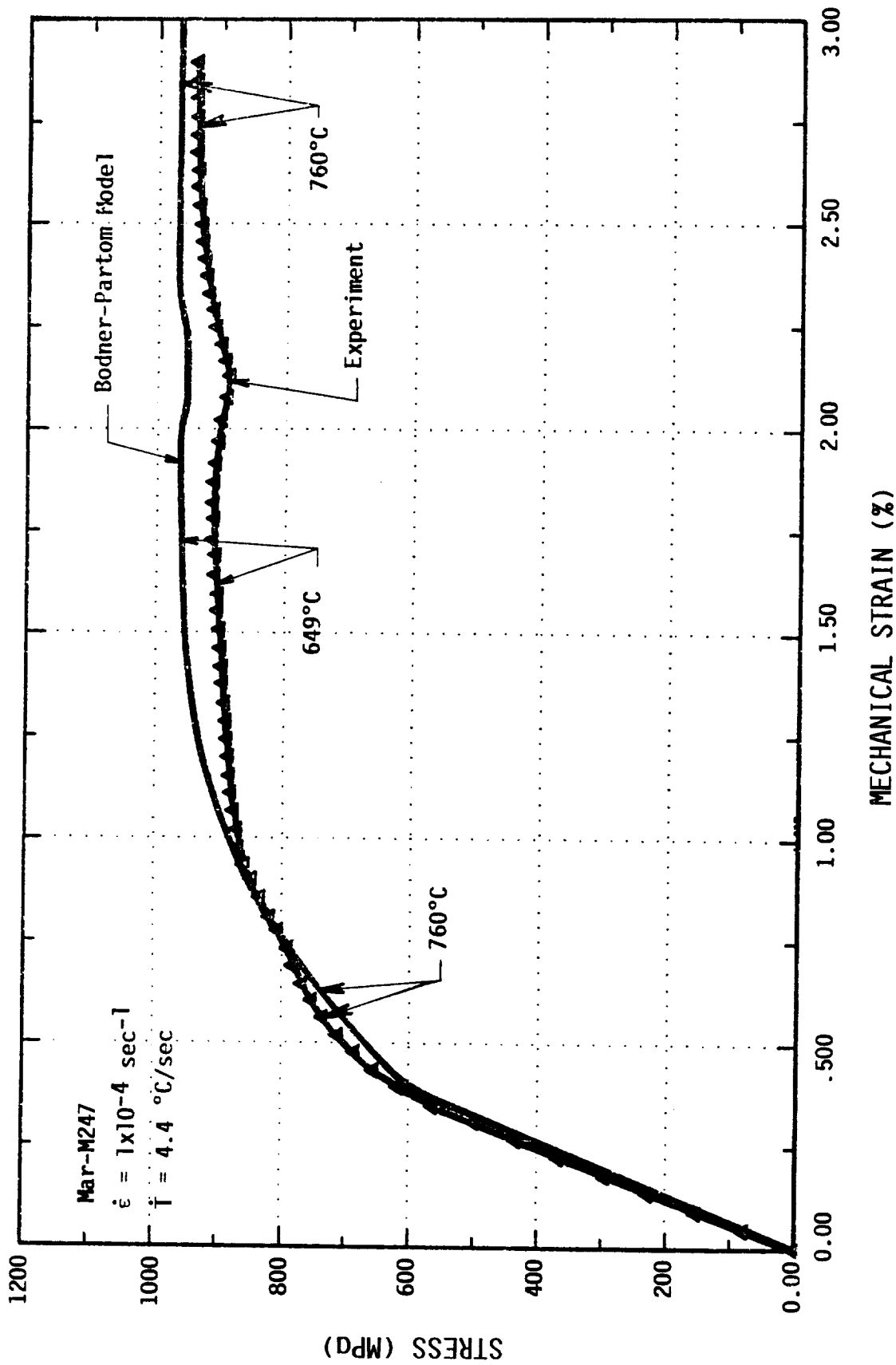


FIGURE 4.7 COMPARISON OF THE BODNER-PARTOM MODEL CALCULATED CURVE WITH THE EXPERIMENTAL RESULTS OF A NONISOTHERMAL TENSILE TEST FOR Mar-M247 WITH TEMPERATURE CHANGES FROM 760°C TO 649°C AND THEN REVERTING TO 760°C

strain of $\approx 1.0\%$, and straining continued until $\epsilon \approx 1.85\%$. The test temperature was then increased to and maintained at 760°C until the mechanical strain reached 3% . The imposed mechanical strain rate was $1 \times 10^{-4} \text{ sec}^{-1}$ throughout the test. Figure 4.7 also shows the Bodner-Partom model calculation obtained on the basis of material constants determined from isothermal data. Good agreement is observed between theory and experiment. In Figure 4.8, the test conditions were similar to the one in Figure 4.7, with the exception that the temperature sequence was 649°C and then 760°C . Good agreement between theory and experiment is also obtained in this case. Figures 4.9(a) and 4.10(a) show the experimental results for the out-of-phase TMF cycle for the mechanical strain ranges of $\pm 0.4\%$ and $\pm 0.6\%$, respectively. The temperature range for the TMF cycle was $538\text{--}982^\circ\text{C}$, and the mechanical strain rate was $1 \times 10^{-4} \text{ sec}^{-1}$. The corresponding Bodner-Partom model calculations are shown in Figures 4.9(b) and 4.10(b). The good agreement between theory and experiment indicates that the thermomechanical deformation behavior of Mar-M247 can be predicted on the basis of isothermal data only.

4.3 Discussion

The objective of Task L was to demonstrate the general applicability of the Bodner-Partom model and the associated procedures for determining material constant, which were developed for the material B1900+Hf, to the alternate material, Mar-M247. In order to evaluate critically the proposed methodology, only a limited amount of test data (mainly isothermal tensile and creep data) were used for obtaining the material constants. The Bodner-Partom model used in this exercise did not include a strain aging term, and all the model calculations including those of nonisothermal and TMF loading were based

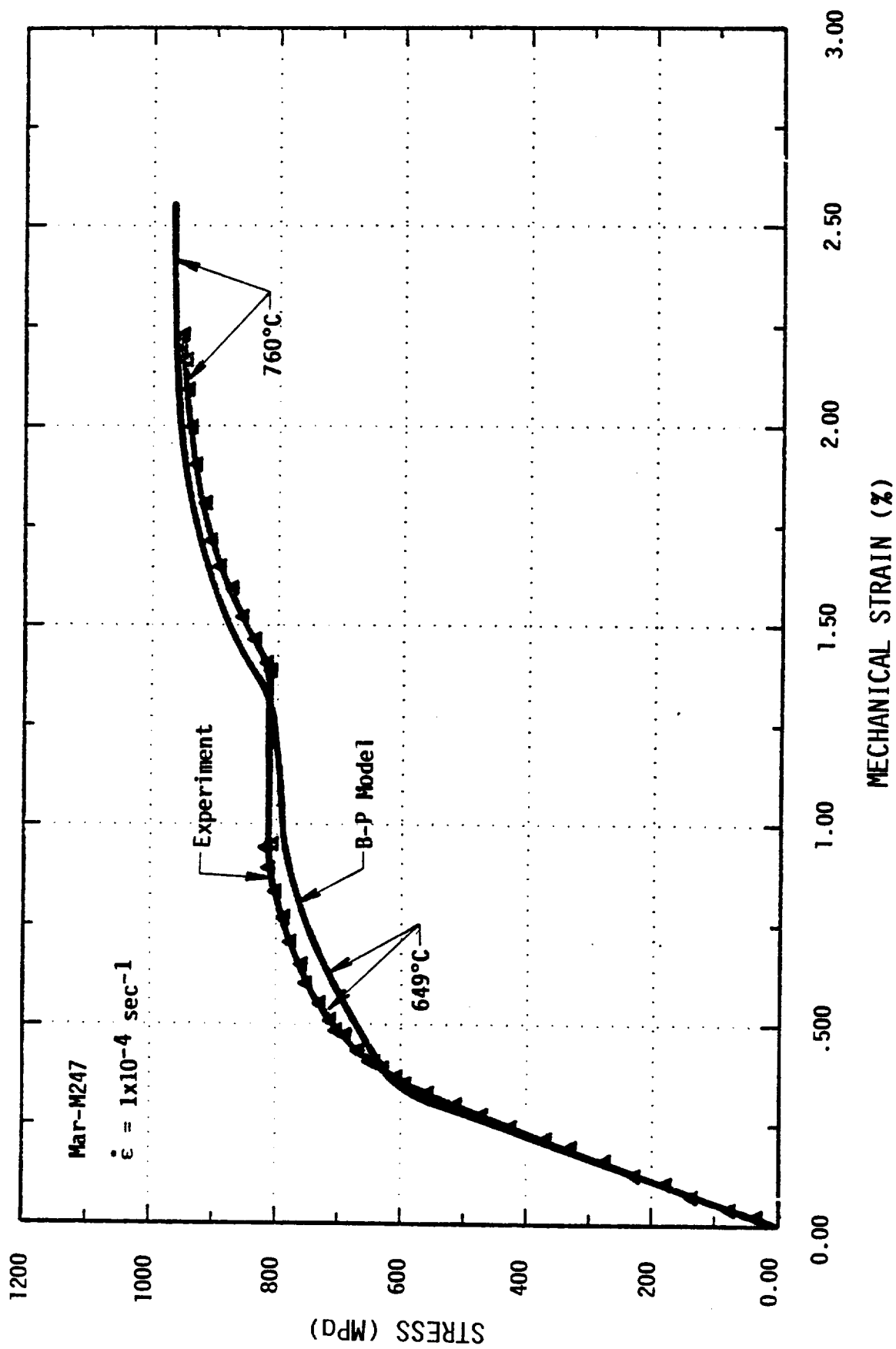
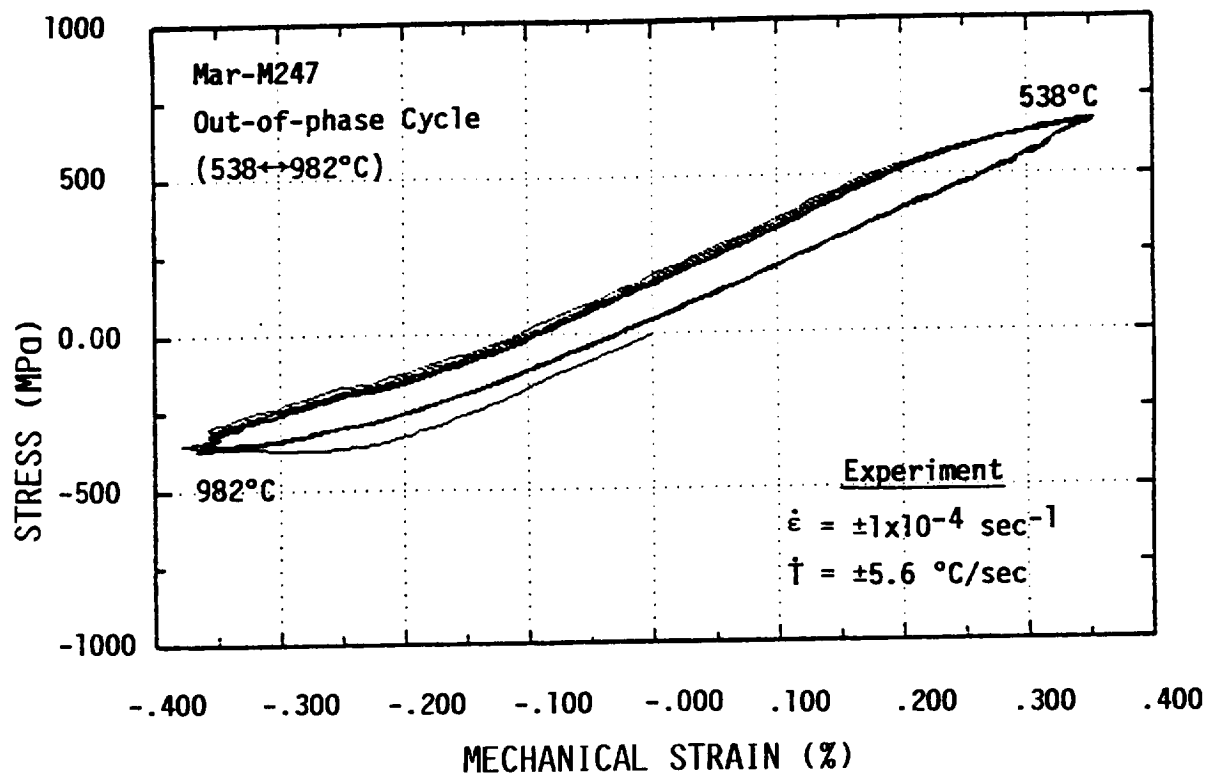
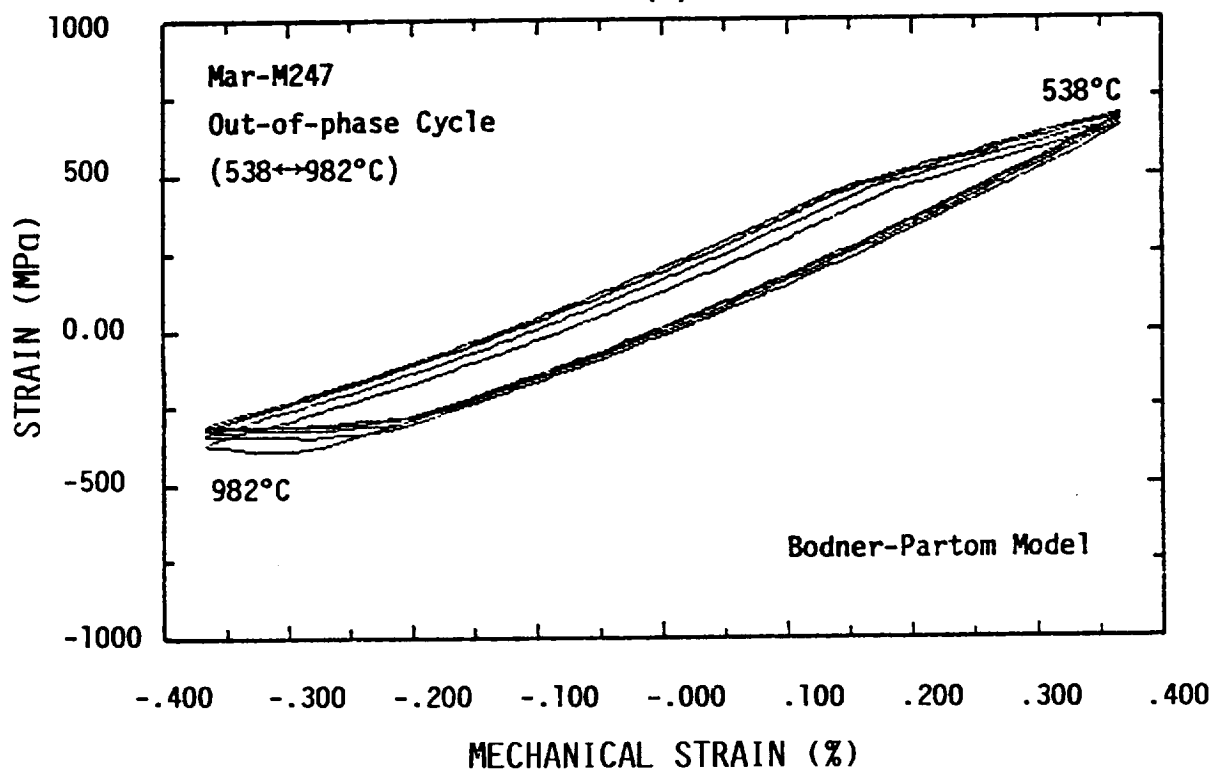


FIGURE 4.8 COMPARISON OF THE BODNER-PARTOM MODEL PREDICTION WITH THE EXPERIMENTAL RESULTS OF A NONISOTHERMAL TENSILE TEST FOR Mar-M247 WITH TEMPERATURE CHANGE FROM 649°C TO 760°C



(a)



(b)

FIGURE 4.9 COMPARISON OF EXPERIMENTAL RESULT WITH BODNER-PARTOM MODEL CALCULATION FOR Mar-M247 SUBJECTED TO AN OUT-OF-PHASE TMF CYCLE OF $\Delta\epsilon = \pm 0.4\%$: (a) experiment, and (b) Bodner-Partom model calculation

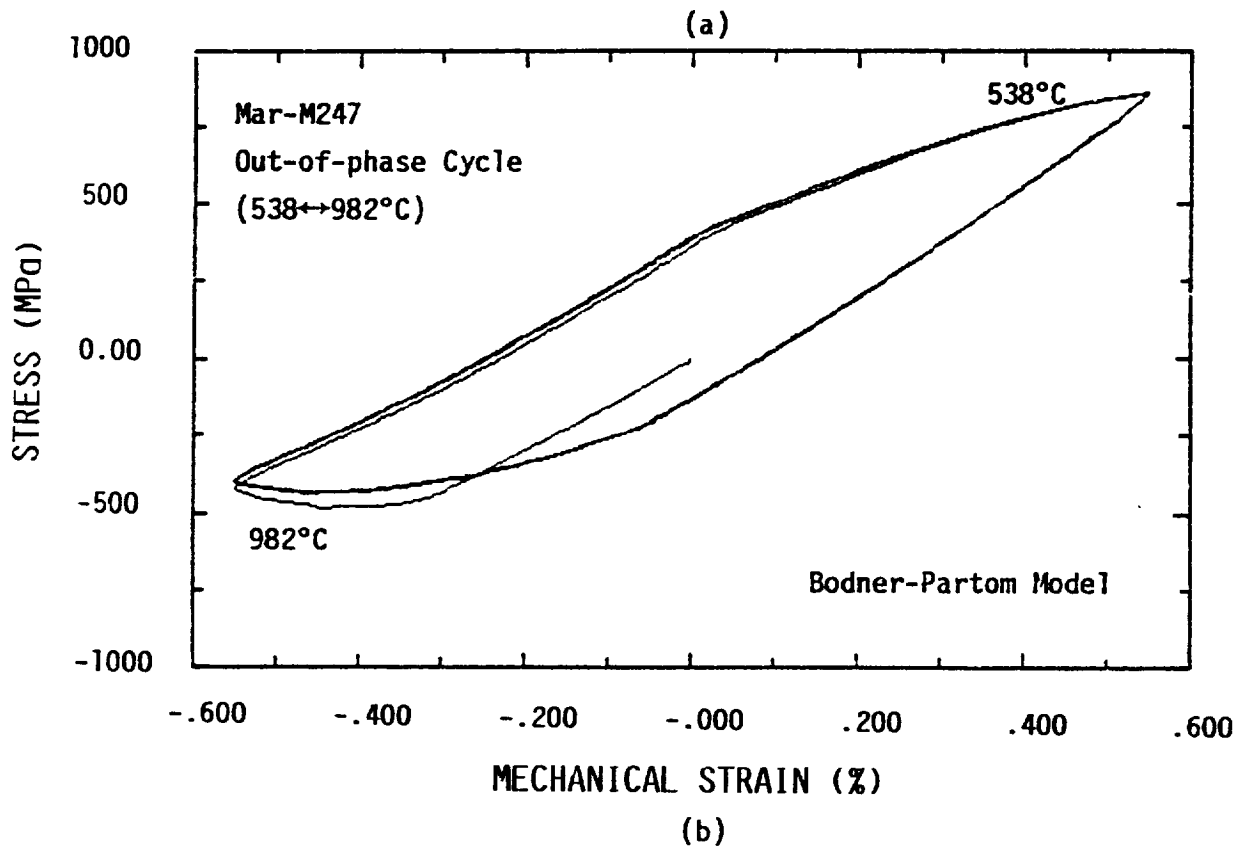
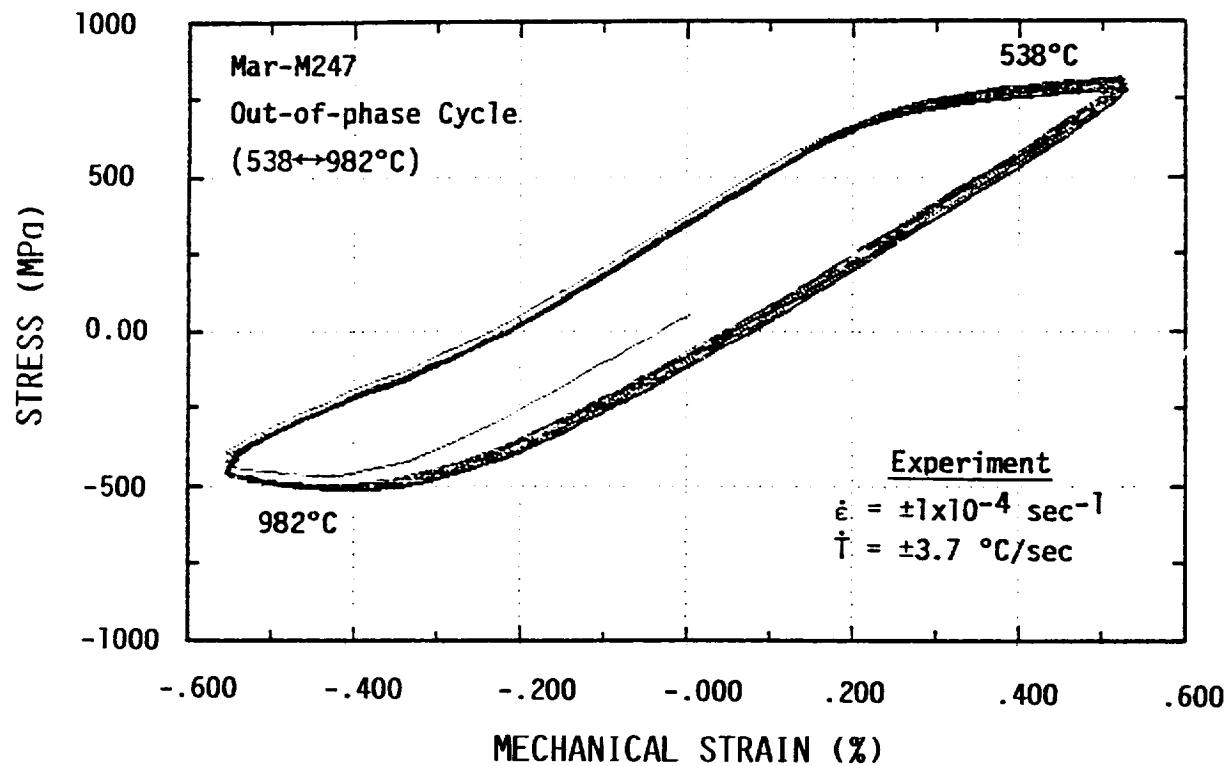


FIGURE 4.10 COMPARISON OF EXPERIMENTAL RESULT WITH BODNER-PARTOM MODEL CALCULATION FOR Mar-M247 SUBJECTED TO AN OUT-OF-PHASE TMF CYCLE $\Delta\epsilon = \pm 0.6\%$: (a) experiment, and (b) Bodner-Partom model calculation.

on isothermal material constants. The good overall agreement between model and experiment for uniaxial and multiaxial strain cycling, and nonisothermal tensile and thermomechanical loading confirms the conclusion previously obtained for B1900+Hf: (1) material constants for the Bodner-Partom model can be determined based only on isothermal tensile and creep data; (2) no additional terms are required in the evolution equations of the hardening variables for representing thermal-history effects. The possible influence of thermal history on inelastic flow can be adequately obtained by integrating the constitutive equations for the imposed thermal and loading histories.

5.0 SUMMARY

The concept of unified constitutive equations for elastic-viscoplastic material behavior has been in existence for twenty years, and the subject has undergone extensive development and application during the past ten years. This program has shown it to be a valid and reliable working tool for some of the more sophisticated engineering applications of materials where strain rate and temperature-dependent inelastic deformations are experienced. This conclusion is based upon: (1) the demonstrated capability of two available unified constitutive models to correlate a wide ranging set of both uniaxial and multiaxial test data on nickel-base alloys at high temperature and (2) the efficient implementation and use of these constitutive equations in a general purpose finite element structural code.

To summarize, the main accomplishments of this NASA-sponsored research program are:

1. The unified approach for elastic-viscoplastic constitutive equations has been shown to be a valid and workable method for representing and predicting material response characteristics in the ranges where strain rate and temperature-dependent inelastic deformations are experienced.
2. A sophisticated test program on two high temperature alloys has been conducted over a wide temperature range for a variety of uniaxial and in- and out-of-phase multiaxial loading conditions, including thermomechanical cycling. The results of the test program provide a data base for evaluation of the representational and predictive capability of constitutive equations.
3. The program has motivated further development of the two sets of constitutive equations under examination.

Walker Equations: modification of the governing kinetic equation; some modifications to the hardening evolution equations; demonstration of temperature dependence of material constants.

Bodner-Partom Equations: development of procedure for determining material constants from monotonic loading test data; development of method for including additional hardening due to nonproportional multi-axial loading; demonstration of temperature dependence of material constants.

4. Explicit procedures were developed for determining all material constants from isothermal test data.
5. The two unified constitutive equations under examination have been incorporated into the MARC finite element code. A number of numerical exercises have been run including thermomechanical cycling histories on components of the hot section of gas turbine engines.
6. Particular material effects have been examined in the test program with regard to their possible inclusion, if required, in the constitutive equations. These consist of:
 - a. additional hardening due to nonproportional multiaxial loading;
 - b. thermal history effects;
 - c. strain aging effects; and
 - d. effects of thin coatings and grain size on mechanical response.
7. Comparisons have been made of features of the two sets of constitutive equations with regard to alternative methods of describing directional hardening and measures of hardening. However, no decisive preferences can be stated.

6.0 REFERENCES

1. U. S. Lindholm, K. S. Chan, S. R. Bodner, R. M. Weber, K. P. Walker, and B. N. Cassenti, NASA CR-174718, May 1984.
2. U. S. Lindholm, K. S. Chan, S. R. Bodner, R. M. Weber, K. P. Walker, and B. N. Cassenti, NASA CR-174980, July 1985.
3. S. R. Bodner and Y. Partom, ASME J. of Applied Mechanics, Vol. 42, 1975, p. 385.
4. S. R. Bodner, "Evolution Equations for Anisotropic Hardening and Damage of Elastic-Viscoplastic Materials," Proc. Conference on Plasticity Today, Udine, Italy, 1983.
5. K. P. Walker, NASA Contract Report NASA CR 165533, 1981.
6. K. S. Chan, U. S. Lindholm, S. R. Bodner, J. T. Hill, R. M. Weber, and T. G. Meyer, NASA CR 179522, August 1986.
7. K. S. Chan, S. R. Bodner, and U. S. Lindholm, "Phenomenological Modeling of Hardening and Thermal Recovery in Metals," Trans. ASME, J. of Eng. Mat. and Tech., 1987 (in press).
8. D. N. Robinson, "Thermomechanical Deformation in the Presence of Metallurgical Changes," Proc. Second Symposium on Nonlinear Constitutive Relations for High Temperature Applications, NASA Lewis Research Center, Cleveland, OH, NASA Conf. Pub. 2369, October 1984.
9. P. A. Bartolotta, "Thermomechanical Cyclic Hardening Behavior of Hastelloy-X," NASA Contractor Report 174999, 1985.
10. D. N. Robinson and P. A. Bartolotta, "Viscoplastic Constitutive Relationships with Dependence on Thermomechanical History," NASA Contractor Report 174836, 1985.
11. J. D. Baird, "Dynamic Strain Aging," The Inhomogeneity of Plastic Deformation, ASM, Metals Park, OH, 1973, pp. 191-222.
12. C. G. Schmidt and A. K. Miller, "The Effects of Solutes on the Strength and Strain Hardening Behavior of Alloys," Acta Metallurgica, Vol. 30, 1982, pp. 615-625.
13. A. Rosen and S. R. Bodner, "The Influence of Strain Rate and Strain Aging on the Flow Stress of Commercially Pure Aluminum," J. of the Mech. and Phys. of Solids, Vol. 15, 1967, pp. 47-62.
14. C. G. Schmidt and A. K. Miller, "A Unified Phenomenological Model for Non-Elastic Deformation of Type 316 Stainless Steel-Part I and Part II," Res. Mechanica, 1981, pp. 109-129, pp. 175-193.

15. A. K. Miller, ASME J. of Eng. Mat. & Tech., Vol. 96, 1976, p. 97.
16. D. P. Pope and S. S. Ezz, "Mechanical Properties of Ni₃Al and Nickel-Base Alloys with High Volume Fraction of γ' ," Int. Metals Reviews, Vol. 29, 1984, pp. 136-167.
17. MARC General Purpose Finite Element Program, MARC Corporation, Palo Alto, CA.
18. G. Cailletaud and J. L. Chaboche, "Macroscopic Description of the Microstructural Changes Induced by Varying Temperature," ICM3, Vol. 2, 1979.
19. A. Philips, "Combined Stress Experiments in Plasticity and Viscoplasticity: the Effects of Temperature and Time," in Plasticity of Metals at Finite Strain: Theory, Experiment and Computation, E. H. Lee and R. L. Mallett Ed., Stanford University, 1981, p. 230.
20. K. S. Chan, U. S. Lindholm, S. R. Bodner, and K. P. Walker, "A Survey of Unified Constitutive Theories," Proc. Second Symposium on Nonlinear Constitutive Relations for High Temperature Applications, NASA Lewis Research Center, Cleveland, OH, NASA Conf. Pub. 2369, October 1984.
21. V. Moreno and E. H. Jordon, "Prediction of Material Thermomechanical Response with a Unified Viscoplastic Constitutive Model," Int. J. of Plasticity, Vol. 2, 1986, pp. 223-245.
22. T. G. Tanaka, "A Unified Numerical Method for Integrating Stiff Time-Dependent Constitutive Equations for Elastic/Viscoplastic Deformation of Metals and Alloys," Dissertation, Stanford University, Department of Materials Science and Engineering, 1983.
23. C. H. Wells and C. P. Sullivan, "The Effect of Temperature on the Low-Cycle Fatigue Behavior of Udimet 700," Trans. ASM, Vol. 60, 1967, pp. 217-222.
24. V. Moreno, D. M. Nissley, and L. S. Lin, NASA CR-174844, 1985.
25. S. M. Copley and B. H. Kear: Trans. AIME, Vol. 239, 1967, p. 977.
26. R. M. Pelloux and N. Marchand, NASA CR-175048, 1986.
27. R. V. Miner, G. P. Allen, P. A. Bartolotta, S. W. Mladsi, and J. R. Ellis, "Investigation of Cyclic Hardening Mechanisms in Hastelloy," Fourth TMF Workshop, NASA Lewis Research Center, Cleveland, OH, September 29-30, 1987.
28. P. A. Bartolotta and J. R. Ellis, "Use of Inelastic Strain as a Basis for Analyzing Thermomechanical Test Data," Turbine Engine Hot Section Technology, NASA Conf. Pub. 2493, 1987, p. 303.

